DEVELOPMENT OF PIEZORESISTIVE SILICON NANOWIRES (SiNWS) AND THE APPLICATIONS IN NEMS TECHNOLOGY

BY

Zhang Songsong

(*B. TECH. (Hons.), NUS*)

A THESIS SUBMITTED

FOR THE DEGREE OF DOCTOR OF PHILOSOPHY

DEPARTMENT OF ELECTRICAL AND COMPUTER ENGINEERING

NATIONAL UNIVERSITY OF SINGAPORE

2014

DECLARATION

I hereby declare that this thesis is my original work and it has been written by me in its entirety. I have duly acknowledged all the sources of information which have been used in the thesis.

This thesis has also not been submitted for any degree in any university previously.

_____

Zhang Songsong

31 Jul 2014

Acknowledgements

Last but not the least, I would like to express my genuine appreciation to my family. Without the encouragement from my parents, I would not able to make such adventure. I would also like to express my deepest gratitude to my beloved wife, Mrs. Yingying Zhu, who has always been supporting me with her unselfish love and undeniably scarification through the past eight years. In addition, I want to gratefully thank my parent-in-law for their unwavering helps and taking good care of my lovely daughter.

Table of Contents

Summary

As one of most sophisticated sensing mechanisms, piezoresistive effect has been widely implemented into various applications diversifying from automotive industry to clinic trial. To further fulfill the market demands (e.g. miniaturization, large sensing range, high sensitivity, good linearity, low cost and high yield, etc.); the research interest is now focusing on nano-scaled materials.

Silicon nanowire (SiNW) is one of the most promising nano-scaled materials and has been well reported for its superior piezoresistive coefficient (or larger gauge factor) compared with the traditional piezoresistive sensing elements (e.g. metal gauge, conductive elastomer, polysilicon/buckle silicon wire and etc.). However, up to date, most literatures are focusing on SiNW fabricated using bottom-up technology. Additionally, a majority of reported data is related to fundamental study and theoretical model. It is thus essential to practically implement the SiNWs into the real device application for the verification of these reported theories and transformation of the frontier research effort into the industry technology.

In this thesis, various fabrication techniques of silicon nanowires with top-down technology on 8 inch wafer are explored and processed. With optimized process flows, the detailed performance of SiNWs based Nano-Electro-Mechanical-Systems (NEMS) prototypes for each specific application (e.g. cantilever shaped flow sensor, diaphragm pressure sensor and neural device with built-in strain gauges) is characterized and discussed. Taking advantages of the nano-scale sensing element, such demonstration of capability for proof-of-concept NEMS sensor facilitates the purpose for the transformation of nanotechnology into the real-world manufacturing.

List of Tables

List of Figures

List of Acronyms

MEMS	Micro-electro-mechanical systems
SiNWs	Silicon Nanowires
NEMS	Nano-electro-mechanical systems
AFM	Atomic force microscopy
TEM	Transmission electron microscopy
SEM	Scanning electron microscopy
SOI	Silicon on insulator
PZR	Piezoresistance
PZT	Lead zirconate titanate oxide (Piezoelectric materials)
RIE	Reactive ion etching
DOF	Degree of freedom
Pt	Platinum
CMOS	Complementary metal-oxide-semiconductor
3D	Three dimension
KOH	Potassium hydroxide
IOP	Intraocular pressure
ICP	Intracranial pressure
NL	Non-linearity
NPD	Neural prosthetic devices
CSC	charge storage capacity
TMAH	Tetramethylammonium hydroxide
BOX	Buried oxide
RTA	Rapid thermal annealing

BARC   Bottom Anti-Reflective Coatings

DRIE   Deep reactive ion etching

DHF   Dilute hydrochloric acid

PECVD   Plasma-enhanced chemical vapour deposition

SiO_2 Silicon dioxide

Si_3N_4 Silicon Nitride

PR   Photoresist

Al   Aluminium

FEM   Finite element method

XeF_2 Xeon difluoride

FIB   Focus ion beam

Structure B   Boss centred diaphragm structure

Structure B&R   Boss centred diaphragm with rib structure along edge

FSS   Full-scale span

MWCNTs   Multi-wall carbon nanotubes

CNTs   Carbon nanotubes

Gold   Au

Ir   Iridium

IrO_x Iridium oxide

ESA   Electrochemical surface area

GSA   Geometry surface area

EDX   Energy-dispersive X-ray

EIS   Electrochemical impedance spectroscopy

PBS   Phosphate buffered saline

Ag   Silver

AgCl   Silver chloride

CSC_c Cathodal charge storage capacity

PEDOT   Poly(3,4-ethylenedioxythiophene)

NI   National Instruments

DC   Direct current

CO_2 Carbon dioxide

PCB   Printed circuit board

CNS   Central Nerve System

s   Second

min   Minute

DVRT   Differential variable reluctance transducer

List of Symbols

R	Resistance of piezoresistor
ρ	Resistivity of piezoresistor
l	Length of particular element (e.g. piezoresistor, cantilever, etc.)
t	Thickness particular element (e.g. piezoresistor, cantilever, etc.)
Δ	The change of the particular parameter
υ	Poisson's ratio
ε	Strain applied on piezoresistor
μ	The mobility of electron
σ_{ij}	Stress tensor
ε_{ij}	Strain tensor
π_{44}	Shear piezoresistance coefficient
π_L	Longitudinal piezoresistance coefficient
π_T	Transverse piezoresistance coefficient
σ_L	Stress component along longitudinal direction
σ_T	Stress component along transverse direction
π_L	Longitudinal piezoresistance coefficient
f	Cantilever resonant frequency
π	Ratio of a circle's circumference to its diameter
k	Spring constant
m	Mass of the cantilever
w	Width of the cantilever
E	Young's modulus
R_e	Reynolds number

ς	Density of fluid
L	Characteristic linear dimension
V	Mean flow velocity
u	Dynamic viscosity
v	Kinematic viscosity
Q	Total flow rate
A	Cross-section area
d	Diameter
L_d	A given distance along the pipe
δ_{max}	Maximum cantilever tip deflection
I	The moment of inertia
Ω	Ohm
G	Gauge factor
h_r	The diaphragm thickness at rib area
h	The diaphragm thickness at hinge area
φ	Diaphragm centre deflection
w_g	Width of the groove
w_r	Width of rib
ξ	The non-dimensional coordinate of the gauge position (1 ~ -1)
a	radius of the diaphragm
E_d	The equivalent Young's modulus of the diaphragm
E_r	The equivalent Young's modulus of the rib
k_s	The support stiffness
σ_0	External stress applied on the substrate in a normal direction
$R(0)$	Resistance at initial conduction (pressure = 0)
$R(T)$	Resistance at a given pressure conduction (pressure = T)
NL_{p-R}	Total NL component between applied pressure and final resistance

$NL_{\varepsilon\text{-}R}$	NL component introduced between strain/stress and resistance
$NL_{\omega\text{-}\varepsilon}$	NL component introduced between deflection and strain changes
$NL_{p\text{-}\omega}$	NL component introduced between applied pressure and mechanical deflection
$\Pi(N,T)$	The piezoresistance coefficient with an impurity concentration N at a temperature T
$\Pi(300)$	The piezoresistance coefficient at temperature of 300 K
$P(N,T)$	The piezoresistance factor with an impurity concentration N at a temperature T
E_f	Fermi energy
η	Permittivity of the electrolyte
γ	The distance between tube internal surface and the maximum charge density of electrolyte ions.
C	Total capacitance: $C=\eta A/\gamma$
C_{dl}	Double-layer capacitance
R_f	Faradaic resistance
W	Warburg impedance
R_s	Series resistance of interfacial electrode
θ	Angular frequency
Z'	Real part of total interfacial impedance
Z''	Imaginary part of total interfacial impedance
Z	Total interfacial impedance
P	Buckling load/force

Chapter 1 Introduction of Piezoresistance Effect of Silicon Nanowires

Piezoresistive transduction is one of the most traditional sensing mechanisms implemented among the first Micorelectromechanical systems (MEMS) devices, which comprise a substantial market share of MEMS sensors in the Market today [1-2]. The piezoresistor made by silicon material has been widely integrated in different mechanical geometries (e.g. a block of substrate, a diaphragm or cantilever) for various applications (acceleration detection [3-4], pressure sensing [5-6], AFM [7-8], flow sensing [9-10], etc.). From the 1980s to the present, continuous improvements in device sensitivity, sensing resolution, detection range, and dimension miniaturization have been driven by extensively increasing market demands. To overcome the bottleneck of the design using traditional piezoresistive sensing elements (e.g. metallic wires, conductive polymer, polysilicon/buck silicon materals), the emerging alternative – single crystalline Silicon Nanowires (SiNWs) has been intensively explored for its superior piezoresistance effects [11-14]. With adequate theoretical studies and literatures on SiNWs, the P-type single crystalline SiNWs have been seems to be the promising candidate for sensor applications [14-16]. However, to date, there are only few reports on the development of SiNWs based sensor are available with the limited field of device applications [17-18]. Therefore, it is absolutely meaningful to validate aforementioned theoretical findings through the practical application of various SiNWs based sensors for diversified purposes. In this thesis, the following works are devoted to exploring the practical value of SiNWs and their integration with MEMS technology for different specific applications (e.g.

cantilever shaped air flow sensor, grooved diaphragm pressure sensor for a low pressure detection, built-in strain gauges for neural implantation and even the highly silicon electrodes for an establishment of electrode-neural interfaces). Before the discussion of detailed works, the introduction on piezoresistive effect of SiNWs will be briefed in this chapter. The following contents are then focused on the understanding of three aforementioned applications, which also explain the motivation of using the SiNWs based NEMS sensors as the replacement for each specific application demonstrated in the later chapters. The particular piezoresistive phenomena in nanoscale are reviewed and the issues involved are presented and commented. Sequentially, the general concept of piezoresistive sensors will be pinpointed. Finally, the state-of-the-art research on several aspects of SiNWs and recently reported SiNW based devices are addressed. In parallel with these efforts, our works further validate the possibility of applying piezoresistance effect of SiNWs in the practical field and push the technology migration from MEMS to NEMS in a new level.

1.1 Piezoresistance effect

The piezoresistance is one of the most important transduction mechanisms. During recent years, piezoresistive SiNWs are extensively explored for their interesting properties and integration potential with MEMS devices. The first part of this section elucidate the very fundamental of piezoresistance and the most commonly concerned properties including the basics, orientation, doping concentration and its related temperature effect, linearity. The second part reviews the new research finding on SiNWs piezoresistance including the so-called "giant piezoresistance effect" and the reasonable conclusion.

1.1.1 Definition of Piezoresistance

Piezoresistivity is the dependence of electrical resistivity on strain changes. The resistivity of a material depends on the internal atom positions and their motions. Strain changes this arrangement therefore, the resistivity [20]. The earliest report of piezoresistance was by William Thomson in 1856 with regard to iron and copper on their resistance change during elongation. Incurring an issue to telegraph companies by causing the signal propagation changes, this phenomenon was later emphasized by researchers and further motivated more effort into this area [21-23]. In 1950, Bardeen and Shockley predicted relatively large conductivity changes with deformation in single crystal semiconductors [24]. In 1954, C. S. Smith reported the first measurement result of the much larger piezoresistance effect in silicon and germanium than that of metallic materials [25]. The following research effort further verifies the Smith's finding [26-27].

1.1.1.1 General expression of piezoresistance

In general, the electrical resistance R of a homogeneous rectangular conductor can be expressed as [28]:

$$R = \rho \frac{l}{wt} \tag{1.1}$$

where R is the resistance, ρ is the resistivity of the material, l is the length, product of w (width), t (thickness) is the cross-section area of the structure. As seen, the resistance is a function of its dimensions and resistivity. When the resistor is stretched, the relative change in resistance is given by:

$$\frac{\Delta R}{R} = \frac{\Delta l}{l} - \frac{\Delta w}{w} - \frac{\Delta t}{t} + \frac{\Delta \rho}{\rho} \tag{1.2}$$

where Δ denotes the change of the each parameter due to the mechanical deformation.

After we introducing Poisson's ratio υ, the gauge factor G (figure of merit for the piezoresistance effect of a particular piezoresistive material) can be defined as:

$$G = \frac{\Delta\rho / \rho}{\varepsilon} + 1 + 2\upsilon \qquad (1.3)$$

where ε ($\Delta l/l$) is the applied strain caused by the elongation of the material. The last two terms in equation (1.3) represent the change in resistance due to geometric changes, which normally is the dominant for the resistance change of metallic gauges, Such contribution of last two terms is in the range of 1~1.5, while, the first term represents the change in resistivity. For silicon and germanium in particular crystalline directions, the contribution of $\Delta\rho / \rho$ is usually 50 times or even larger than the geometric factor. Thus, the gauge factor of semiconductor can also be simplified as:

$$G = \frac{\Delta R / R}{\varepsilon} \approx \frac{\Delta\rho / \rho}{\varepsilon} \qquad (1.4)$$

1.1.1.2 Resistivity changes of piezoresistive material

The discovery of such large resistivity changes demands a theory of the underlying physics. This section discusses the prevailing theories based on both theoretical model and empirical finding according to experimental results. The theories of semiconductor piezoresistance are explained in one-dimensional descriptions of electron and hole transport in crystalline structures under strain (potentially extended to three dimensions and to include crystal defects, electric potentials, and temperature effects).

With Smith's piezoresistance measurements, existing theories were based on shifts in bandgap energies. The band structure of diamond was first calculated by Kimball in 1935 [29], and that of silicon by Mullaney in 1944 [30]. In 1950, Bardeen and Shockley presented a model for mobility changes in semiconductors subjected to

deformation potentials and compared both predicted and measured conductivity changes in the bandgap with dilation [24]. It also served as the basis for later analyses [31-32]. In general, most models point out the direction dependence of bandgap and electron energies with respect to their wave functions in momentum space and the mobility changes. In addition, N- and P-type piezoresistors exhibit opposite trends in resistance changes and different direction-dependent under strain/stress (most analysis carried in small strain range, e.g. <0.1%).

For N-type silicon, many valley energy surfaces in momentum space are the well-recognized explanation for the large directional resistivity changes. Herring proposed that the band energy minima in three orthogonal directions (x, y, z) as locations of constant minimum energy show in Figure 1.1 for commonly used (100) plane silicon wafer [31-32]. The minimum energy of each valley lies along the centerline of the constant energy in ellipsoidal shape. Electrons have a higher mobility along the direction perpendicular to the long axis of the ellipsoid. In another words, the mobility (μ) is the lowest when parallel to the valley. For instance, an electron in the z direction has higher mobility in the x and y directions. The valley is defined by the bounded higher energy regions with ellipsoidal energy surface. Net electron conductivity is the sum of the conductivity components along three valleys. Net mobility along the direction of strain is the average mobility along all three valleys. When a uniaxial elongation (tensile strain/stress) is applied (Figure 1.1 (a)), the band energy of the valley parallel to the strain increases and the electron is transported to the perpendicular valleys. These transported electrons favor a higher mobility in adjacent valleys and result in the higher overall conductivity (or lower resistivity). With the same explanation, a compressive strain/stress will have the opposite piezoresistance effect. However the shear strain/stress (Figure 1.1 (b)) does not affect

the energy valley, hence, a very small piezoresistive behavior in <110> direction.
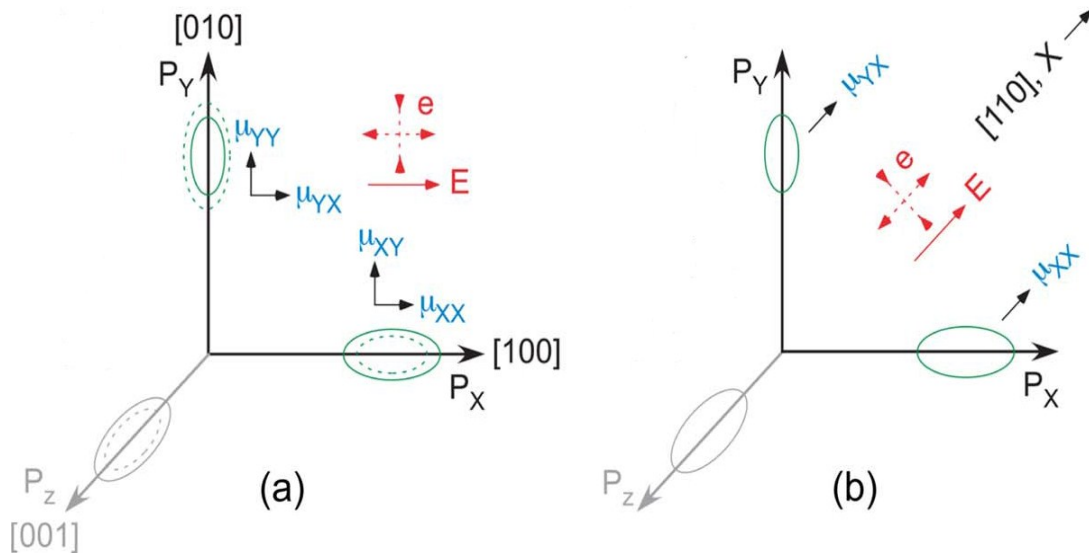
Figure 1. 1 Schematic illustration of the <100> valley in momentum space for N-type silicon under uniaxial strain. Dotted lines show the effect of strain/stress. (a) and (b) refer to the uniaxial and transverse strain/stress respectively [33].

On the other hand, the piezoresistance effect for P-type silicon is too complicated to be clearly explained. To match the experimental results in both low and high doping regimes, the exploration of a valid theoretical model is still undergoing up to now [34-38]. In general, the warped spherical energy surface is expected unlike the ellipsoid in N-type silicon [28, 35]. As depicted in in Figure 1.2, the common consensus of piezoresistance for P-type silicon is focusing on the strain induced degeneracy splitting between heaven and light hole energy bands. Such splitting leads to the holes transportation and the shift in effective mass, resulting in large resistivity changes. Please refer to Ref. [35-38] for more detailed explanations. Although the theoretical model has not been perfected, the research effort has pointed out the tendency of the piezoresistance effect related to several very important parameters, such as crystalline orientation, implantation profile and the related temperature effect.
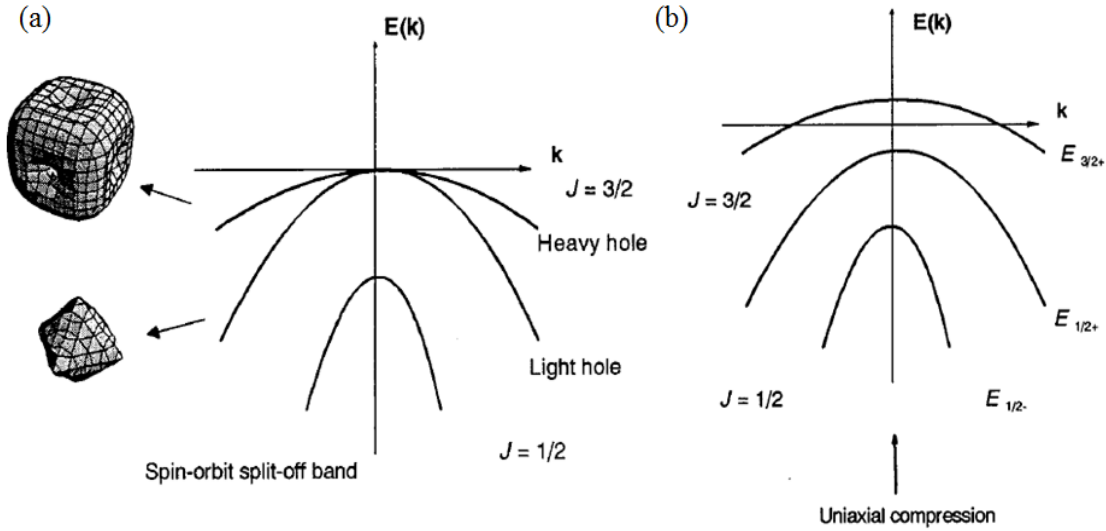
Figure 1. 2 Schematic of hole energy of silicon subjected to uniaxial stress [35].

1.1.1.3 Crystalline orientation

Crystalline silicon forms a covalently bonded diamond structure (lattice constant = 5.34Å), which is correlated to a regular face-centered-cubic structure in the reciprocal space. For a homogenous material (e.g. silicon), the stress and strain tensors can be correlated by Hooke's law. In static equilibrium state, both forces and moments sum to zero, thus, a stress tensor is always symmetric and so is the strain tensor, named as σ_{ij} and ε_{ij} respectively. The piezoresistance coefficient is related to stress and the electric component. Both parameters are second-rank tensors. The electric component relates to the potential and current. Stress component is referring to dual directions. Therefore, the original piezoresistance coefficient is described by a fourth tensor component. For the conciseness, the subscripts of each tensor are also simplified, e.g., $\pi_{1111} \rightarrow \pi_{11}$, $\pi_{1122} \rightarrow \pi_{12}$, $\pi_{2323} \rightarrow \pi_{44}$ (the shear coefficient) [20]. Based on these denotations, Smith determined the relationship of these piezoresistance coefficients for commonly used (100) plan silicon wafer as shown in Figure 1.3 [25].

$$\frac{1}{\sigma}\frac{\partial\rho}{\rho}=\pi_{11} \qquad \pi_{12} \qquad \frac{1}{2}\left(\pi_{11}+\pi_{12}+\pi_{44}\right) \qquad \frac{1}{2}\left(\pi_{11}+\pi_{12}-\pi_{44}\right)$$
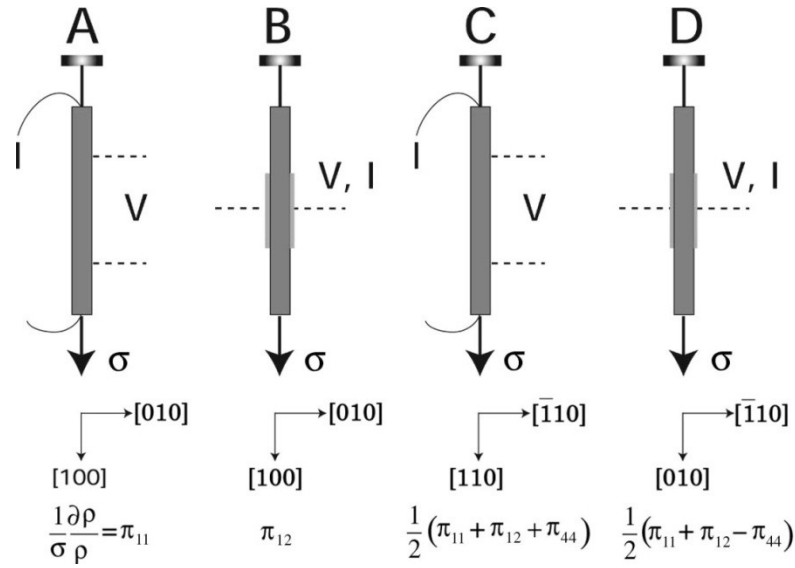
Figure 1. 3 Schematic showing the stress/strain system with explanations on crystalline orientations and electrode arrangement [25].

Specimens A and C indicate the longitudinal piezoresistiance coefficients (π_L) along <100> and <110> directions, whereas, B and D demonstrate the transverse piezoresistance coefficients (π_T) along each directions. The notation of "longitudinal" or "transverse" is defined based on the relationship between the directions of sample elongation and current flow. If two factors are aligned or placed in parallel, the specimen is said in a longitudinal manner. In case of the orthogonal relationship, it is said in a transverse manner. Additionally, it is worth noting that the longitudinal axis of the piezoresistor is arbitrary, not necessarily to coincide with the cubic axes. Furthermore, the structures are usually defined along [100] or [110] direction in real applications on a (100) wafer. This can be explained by two reasons. First of all, (100) wafers are most commonly used due to their relatively low cost. Secondly, the [100] n-type and [110] p-type silicon show the highest piezoresistive effect in comparison with otherwise configured piezoresistors on the (100) wafer. The details has been summarized in a graphic manner and shown in Figure 1.4 [34].
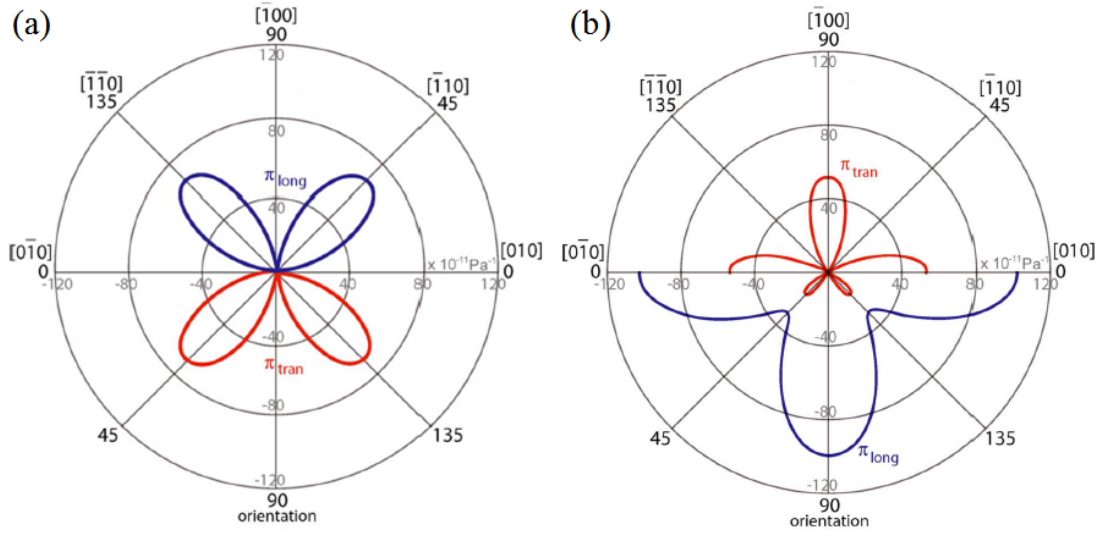
Figure 1. 4 The graphic explanation of piezoresistance coefficients on (100) silicon wafer for (a) P-type silicon and (b) N-type silicon [34].

For the p-type silicon, the highest piezoresistive coefficient lies along the [110] directions. More importantly, both longitudinal and transverse coefficients are in equivalent amount. Hence, the highly symmetrical design can be realized by using P-doped piezoresistors with proper electrical layout arrangements (e.g. Wheatstone bridge). For the n-type silicon, the highest longitudinal coefficient exists along [100] direction. However, the corresponding transverse component is few times smaller. Information obtained from the graph provides a good reference for the sensor design. Nowadays, P-type silicon in [110] direction is usually configured in Wheatstone bridge in the MEMS design for a better sensitivity resolution and immunity of temperature variations. However, the graph is obtained for the silicon under a rather low doping concentration based on Smith's data, it is necessary to consider the particular doping concentration for a specific design.

1.1.1.4 Impurity concentration and related temperature effects

It has been pinpointed that the piezoresistance reported by Smith was measured using lightly doped silicon samples with a fixed room temperature. However, the

substantial information on silicon with higher impurity concentration with respect to temperature variation was not completed. Such information would be vitally important for the sensor design. In 1957, F. J. Morin *et al.*, reported the silicon and germanium specimen with relatively higher doping [39]. With the setup of a three-wall cryostat (consists of a nitrogen-cooled radiation shield and an inner heat), temperatures over 5° to 350° K was achieved for germanium and 20° to 350° K was achieved for silicon. In 1962, O. N. Tufte *et al.* [40] further extended the doping concentration in the range from 10^{18} to 10^{21} cm^{-3}. In their experiment results (shown in Figure 1.5), the dominant piezoresistance coefficients (π_{11} for N-type and π_{44} for P-type silicon) generally decayed with the rising temperature. The phenomenon was even obvious for the lower doping specimens regardless of the type for the doping.
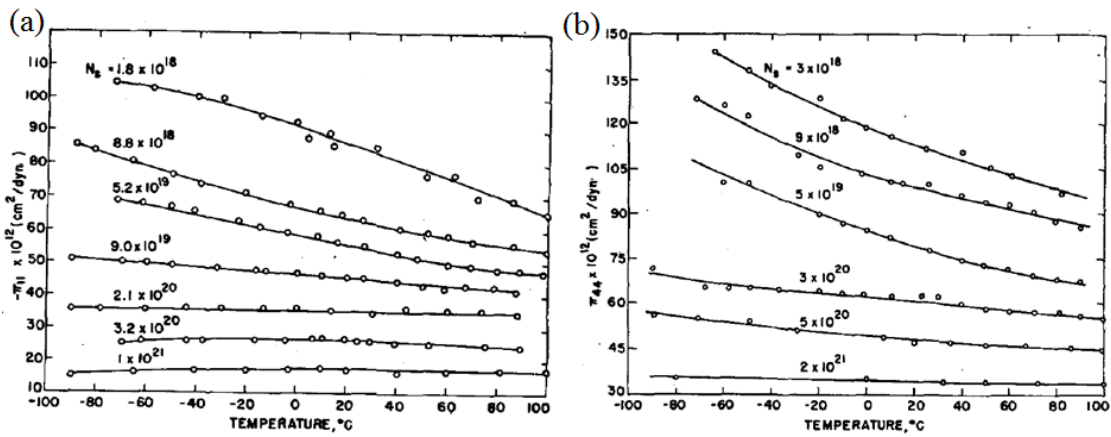
Figure 1. 5 Variations of piezoresistance coefficients with respect to temperature changes under different doping concentrations for (a) N-type silicon and (b) P-type silicon.

With the pioneer efforts, J. A. Harley and T. W. Kenny summarized the reported longitudinal piezoresistive coefficient as a function of boron concentration (shown in Figure 1.6) [41]. Kanda also presented theoretical calculations of piezoresistive changes versus doping concentrations. He suggested a simple power law dependence of the relaxation time with temperature and noted a discrepancy between his calculations and for high doping concentration. Up to today, it is still hard to

completely match the experimental data with the theoretical model in a wide doping range [38]. However, as far as the sensing application is concerned, the range of the doping profile should be $>10^{18}$ cm^{-3} (details of dosage optimizations will be demonstrated in Chapter 2.2). In addition, the empirical findings prove the optimized doping concentration at around 10^{18} cm^{-3} and 10^{20} cm^{-3} for a less temperature influence [28].
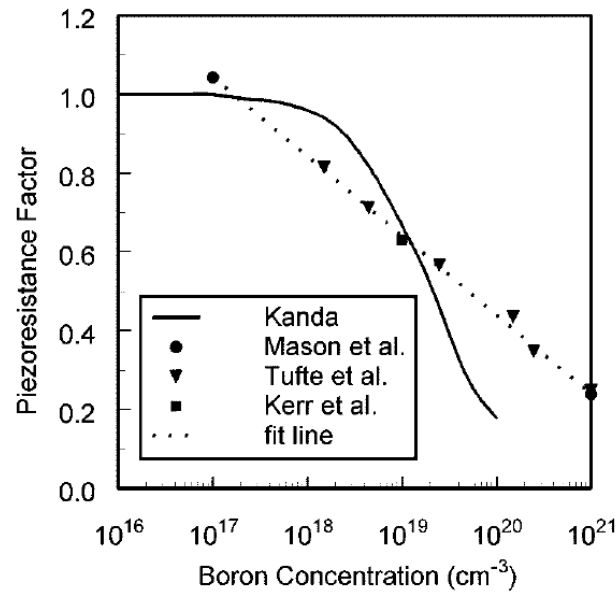
Figure 1. 6 Summary of longitudinal piezoresistive coefficients as a function of boron concentration [41].

1.1.2 Piezoresistance of Silicon Nanowires (SiNWs)

1.1.2.1 Giant piezoresistance effect

Most efforts on nanowires researches started after year 2000, the initial thought was to facilitate the device miniaturization. The interesting finding was spotted for the boost of piezoresistance effect with the decrease of the piezoresistor dimension [15-17, 42]. In 2006, He and Yang reported their observation of a very large piezoresistance effect (so called "giant piezoresistance effect") [11]. A significant enhancement of piezoresistance effect was discovered for the bottom-up fabricated SiNWs (growth on

the substrate from seeding layer) in <111> direction under a low P-doping condition. The bridge structure and the morphology of the SiNW are shown in Figure 1.7 (a) and the following TEM confirmed the crystalline orientation of the nanowire. As indicated in Figure 1.7 (b), the characterization was conducted using the standard four point set-up in both tensile and compressive region under strain around ±0.06%. Such structure ensured a longitudinal strain application and the electrical measurement was conducted when the strain applied. The resultant piezoresistive coefficient (up to 3550×10^{-11} Pa^{-1}) was 60 times higher than that of bulk silicon. With the variations of cross-section geometry, there four types of nanowire resistance changes (denoted in 4 different colors) versus strain were plotted in Figure 1.7 (c). In addition, the reported large piezoresistance effect appeared only in the compressive strain (not applied in the tensile strain). It is worth noting piezoresistive behavior in their finding, since the gauge factor was usually reported identical in both strain directions. However, the author did not specifically address the reason for such this non-symmetry.
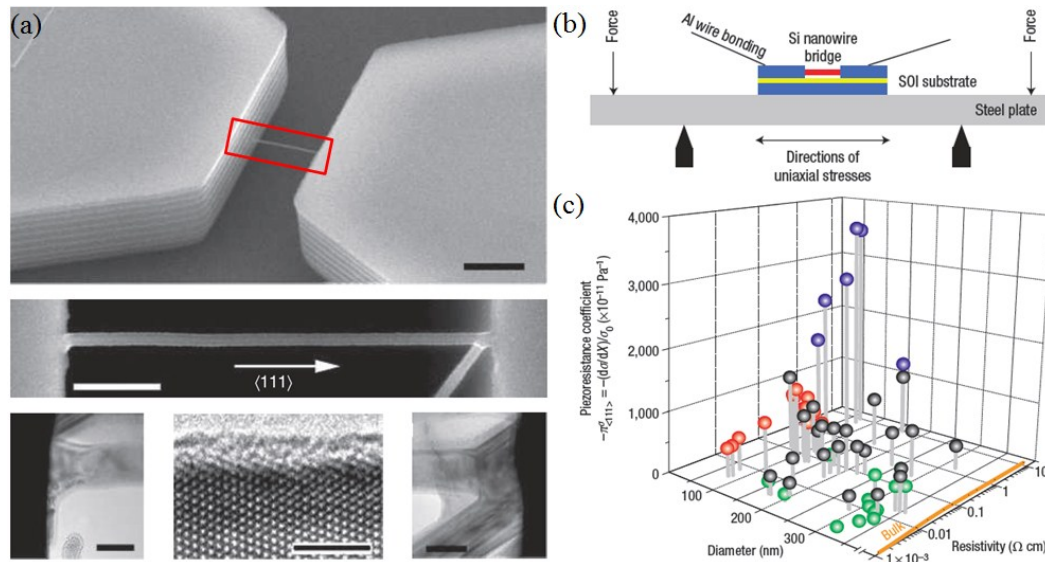
Figure 1. 7 (a) <111> oriented silicon nanowire (SiNW) bridges on SOI substrate. Insets show SEM of a single nanowire with the <111> growth direction and its cross-section with TEM. The scale bars are 2 μm, 500 nm, 100 nm and 3 nm, respectively. (b) Schematic diaphragm for the four-point bending setup used to apply uniaxial stresses on SiNWs. (c) First-order longitudinal piezoresistance coefficients of P-type SiNWs and their dependence on diameter and resistivity [11].

Encouraged by Yang's work, K. Reck *et al.* further extended the finding of "giant piezoresistance" on SiNW fabricated using top-down method (by electron beam writing and reactive ion etching processes) in order to comply with conventional fabrication techniques [43]. The test chip together with a reference resistor is integrated with contacts for electrical 4-point measurements as shown in Figure 1.8 (a). The reported increase in piezoresistance effect is up to 633% compared to that of bulk silicon. Both measurement result and comparison table were summarized (Shown in Figure 1.8 (b) & (c)). In addition, preliminary temperature measurements indicated a larger temperature dependence of silicon nanowires compared to bulk silicon. An increase of up to 34% compared to bulk polysilicon was observed in polysilicon nanowires with decreasing dimensions

Resistor	ρ [Ω·cm]	π_{44} [10^{-11} Pa]	$\pi_{44}/\pi_{44,ref}$
Reference	0.02	124	-
480x340 nm²	0.02	140	1.1
280x340 nm²	0.02	165	1.3
140x340 nm²	0.02	212	1.7
140x200 nm²	0.4	910	7.3
Smith [7]	7.8	138.1	1.1
Tufte et al. [8]	0.02	113	0.9
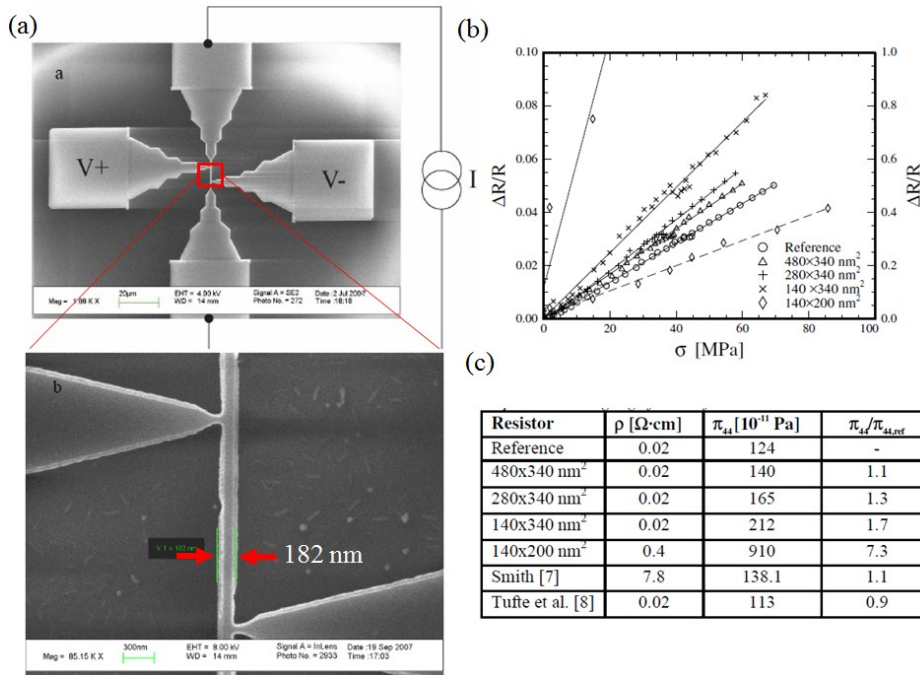
Figure 1. 8 (a) A silicon nanowire etched in the 340 nm device layer of an SOI wafer by RIE process. (b) The plot the resistance changes vs. the strain for different dimension of SiNWs. (c) The comparison table also includes reported works.

Through the similar top-down fabrication process, N. Pavel *et al.* demonstrated the giant piezoresistance effect by the modulation of an electric field-induced external

electrical bias [12]. In their report, the SiNWs were embedded at the anchor of a cantilever and the compressive strain was applied by using a PZT controlled needle to push the free end of the cantilever. Their testing setups were provided in Figure 1.9 (a) & (b). The carrier concentration of the SiNW was modulated via a backside biasing voltage. (c) Indicated holes concentration in SiNW as function of gate bias. Positive bias for a p-type device (negative for an n-type) partially depleted the SiNWs forming a pinch-off region, which resembled a funnel through which the electrical current squeezed. This region determined the total current flowing through the nanowires. It was plotted in Figure 1.9 (d), the SiNW showed a gauge factor as high as 5000 at the depletion mode when the carriers inside the channel are pushed out of the channel. This experiment used SiNW with dosage as low as 1×10^{12} cm^{-2} and was conducted in a strictly controlled dark, low noise environment.
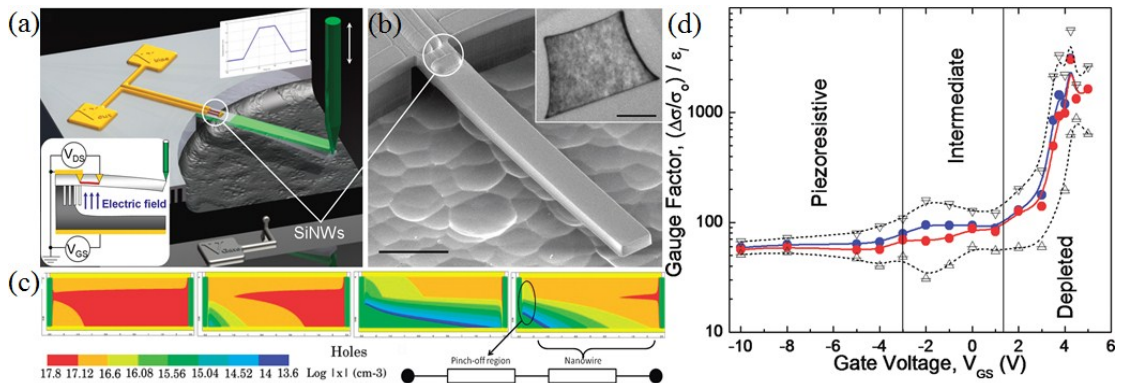
Figure 1. 9 (a) Schematic of the testing setup. (b) SEM image of the released cantilever. (c) Holes concentration in nanowire as function of gate bias (V_{gs}). (c) Extracted gauge factor as a function of V_{gs}. Increasing bias resulted in a gauge factor up to 5000 at 3.75V [12].

Even through the "giant" performance of SiNW was reported by several groups, the actual existence of "giant piezoresistance" was questionable. The correspondence letter was drafted from A. C. H. Rowe regarding to the "giant effect" reported by He and Yang [44]. By numerically solving the Poisson-Boltzmann equation using the finite element methods, he suggested that the so-called "giant piezoresistance effect"

should be considered "by no means a new phenomenon". Two years later, the same French group further explained such apparent giant piezoresistive effect and published their works in Physics Review Letters [13]. Their findings were briefly listed as the following:
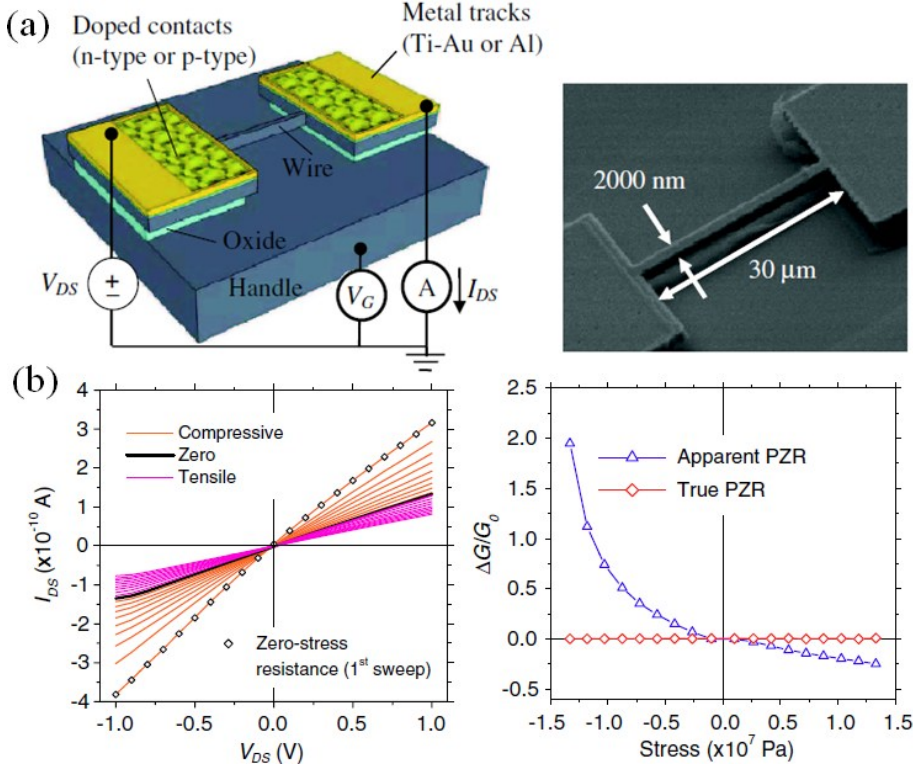
Figure 1. 10 (a) Typical testing setups of nanostructures and the SEM image of a released 2μm × 2μm × 30μm. (b) Plots of I_{ds}-V_{ds} measurements of a 50nm × 50nm ×1μm P-type nanowire before and after applying $V_{ds} = 0.5V$ with V_{gs} fixed at $0V$ [13].

With the testing setup shown in Figure 1.10 (a), they found that the resistance was varying strongly with time due to electron and hole trapping at the sample surfaces (between SiO_2 and Si interfaces) regardless of the applied stress. Under such circumstance, the time-varying resistance manifested itself as an apparent giant piezoresistance (apparent PZR) identical to that reported by He and Yang. By modulating the applied stress in time, the true piezoresistance of the specimen was found to be in the equivalent range with that reported by buck silicon counterpart. The measurement was also given in Figure 1.10 (b).

1.1.2.2 SiNWs for mechanical sensor design

Without further ado on the word "giant", another research group from University of Minnesota published their findings in 2010 [14]. As shown in Figure 1.11 (a), P-doped SiNWs on (100) plan SOI wafer along <110> and <100> direction were investigated under <100>-oriented strain. The nanowire thickness was varied from 23 to 45nm, the width was varied from 5 to 113nm. The length of SiNWs was fixed and no back-gate bias was applied for all their tests.
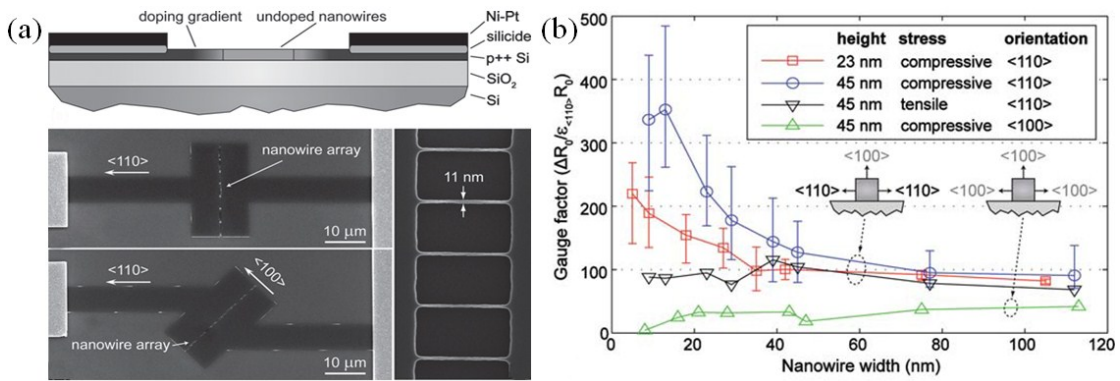
Figure 1. 11 (a) The schematic drawing of testing setup and SEM images of fabricated SiNWs along <110> and <100> directions, respectively. (b) Plot of extracted gauge factors with respect to variations of SiNW cross-section dimension.

The results plotted in Figure 1.11 (b) seemed different from these aforementioned findings. First of all, the SiNW in <100> under compressive gave the smallest value of gauge factor. In <110> direction, the shrinkage of the cross-section of SiNW did enlarge the gauge factor, but the repeatability of such results was not stable, especially for the smallest geometry (10×23 nm^2). In addition, it was also worth noting that the performance of P-doped SiNW along <110> direction under tensile stress was quite reliable with less influence on geometric variations after the width reduced below 120nm. Such result has also confirmed the suggestion on the piezoresistive mechanical sensor design early given by T. Toriyama *et al*.[35].

In their report, P-type SiNWs with minimum cross-section of 53×53 nm^2 were fabricated by the combination of thermal diffusion, electron beam lithography and

reactive ion etching (RIE) processes. Assume the stresses are uniform within the piezoresistor (SiNWs), the actual resistance change would be caused by biaxial stress, since SiNWs are normally embedded in the much bulky substrate layer. The induced the resistance change is thus given by [44]:

$$\frac{\Delta R}{R} = \pi_L \sigma_L + \pi_T \sigma_T \tag{1.5}$$

Where σ_L and σ_T are the induced stress components along longitudinal and transverse directions, respectively. In general, both surface in-plane having the same signs. However, π_L and π_T have opposite signs for main crystallographic orientation in silicon. As a consequence, the combination of both products always leads to a decrease in total resistance change in the conventional piezoresistive mechanical sensor. It was suggested by T. Toriyama *et al.* that the optimized geometry and doping concentrations of the SiNW will minimize the stress transmission in transverse direction, thus, a higher overall resistance changes along the stress applied direction than the output provided by bulk silicon piezoresistor. In addition, with the advantage of the reduced length and width, it is feasible to fabricated the SiNW at exact the high stress region without an average effect with adjacent lower stress region as the case of using bulk piezoresistive sensing elements. The detailed design consideration of SiNWs based NEMS sensor will be discussed in chapter 4 by using pressure sensor as an example, but it is reasonable to believe a larger piezoresistance effect of SiNWs over that of traditional bulk piezoresistive sensors even without considering the reality of so-called "giant piezoresistance effect".

1.2 Applications of Piezoresistance Effect in Conventional MEMS Physical Sensors

In this section, we will review the implementation of piezoresistance effect in MEMS sensor design based on three particular applications, namely as MEMS flow sensor, MEMS pressure sensor and silicon based neural probe. Literatures about the pioneer works and motivations will be briefly addressed as the followings.

1.2.1 MEMS Flow Sensor

Flow sensors have attracted numerous attentions due to their various applications such as weather predictions and automotive applications. As MEMS technology progresses in terms of lower manufacture cost and miniaturized dimension, the MEMS based flow senor not only fulfills the market demands for the traditional sensing purpose [46], it has also been successfully implemented into biomedical applications [47-49].

1.2.1.1 Thermal flow sensor
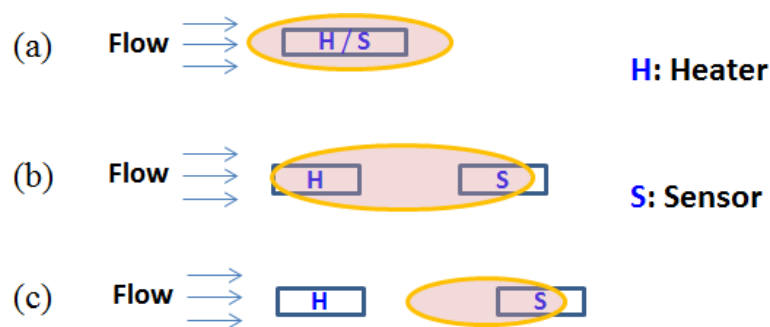
Figure 1. 12 Three principles used in thermal flow sensing: (a) thermal anemometry, (b) calorimetric flow sensing, and (c) time-of flight flow sensing [51].

In 1974, the first MEMS flow sensor was introduced based on thermal sensing mechanism [50]. As illustrated in Figure 1. 12 this mechanism can be categorized into three types: thermal anemometers, calorimetric flow sensors and time-of-flight flow

sensors depending on the different thermal sensing principles [51].

In general, no matter which thermal sensing principle is applied, an ideal thermal flow sensor is sensitive only to the thermal profile/effect of certain flows. Although the thermal sensing mechanism provides excellent sensitivity [52-56] and fast response time [54-58], for most thermal flow sensors, the extent of improvements for these parameters is always proportional to their increased input power. Therefore, one of the common problems for such thermal based flow sensor is their high power consumption and self-heating problems, which limits the application in many chemical and bio-medical environments. In additional, the extra heat dissipation is generated through the heat convection from the heating element to the device substrate or through the air. Thus the thermal insulation becomes an important aspect for thermal sensor design to prevent the extra heat loss.
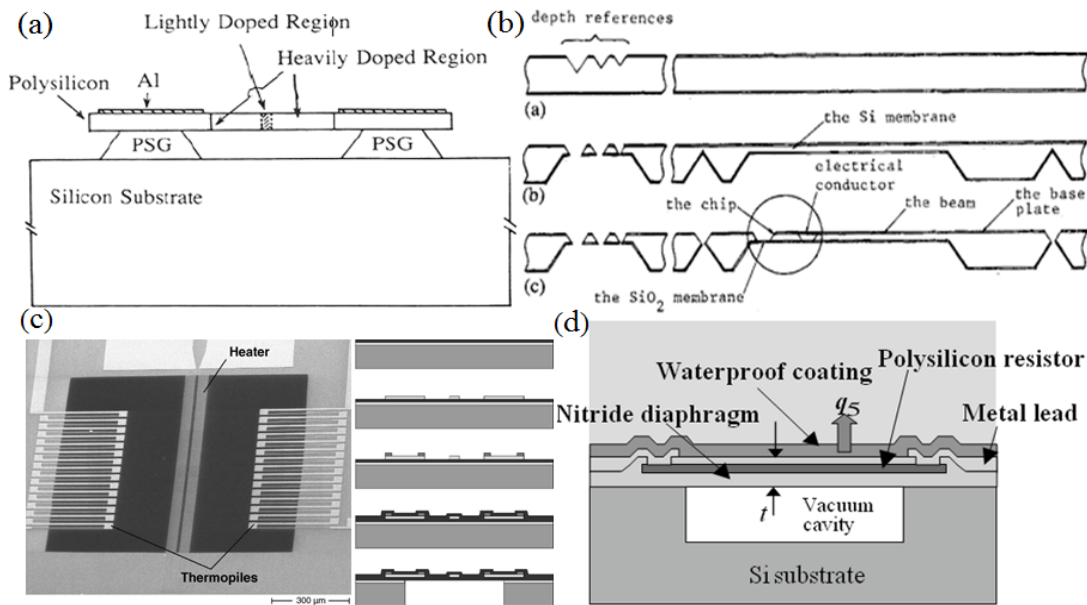
Figure 1. 13 Various methods for heating isolations: (a) with different doping concentration on polysilicon layer [59], (b) applying insolating barrier by the material with a low thermal-conductivity [61], (c) using suspending structure for thermal isolation [56], and (d) applying vacuum cavity beneath the heating structure [63].

Numerous methods have been tried out over the past decades to refine the design required to incorporate the thermal insulation. For instance, changing doping

profile [59] (Figure 1.13 (a)), implementing low thermal-conductivity layer [58, 60-61] (Figure 1.13 (b)), using freestanding structure [53, 56] (Figure 1.13 (c)) and applying vacuum cavity beneath the heating structure [62-64] (Figure 1.13 (d)) have been demonstrated as methods for improving thermal insulation by various research groups in their flow sensor designs. However, due the intrinsic power scavenging nature, the total power consumptions for most thermal air flow sensors are still above 1mW [54, 65-70]. For the liquid flow sensing, the power consumption can be even higher [68]. In addition, compromised by the high sensing resolution, the sensing range is always limited for many thermal flow sensor designs [55, 70]. To overcome the limitation of a narrow flow sensing range, Svedin *et al.* reported the flow sensor with the combination of two mechanisms [71]. The thermal sensing scheme was used for lower flow rate detection, while the piezoresistive sensing scheme was applied for the higher flow rate sensing.

1.2.1.2 Cantilever shaped piezoresistive flow sensor
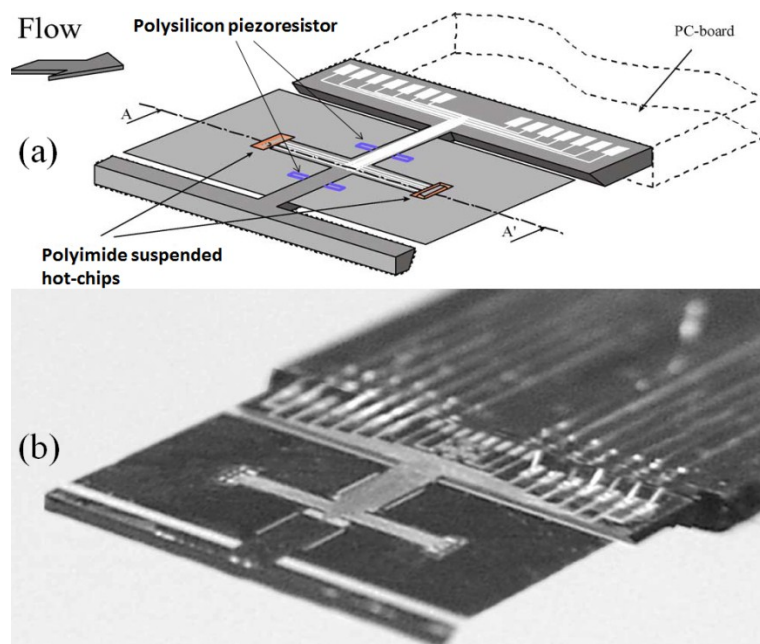
Figure 1. 14 The schematic drawing of the lift force flow sensor with integration of both thermal sensing (hot-chips) and piezoresistive sensing (polysilicon piezoresistor) mechanism, the optical image of the fabricated device is given at bottom [71].

The detailed device structure is illustrated in Figure 1.14. In the piezoresistive sensing scheme, the sensing structure will be deformed by flow induced mechanical force, i.e. lift force [71-72], shear force [73-74], drag force [75-76] and even the pressure difference [77-78]. As a result of the mechanical deformation, the strain change will be experienced by the piezoresistor. Consequently, the strain induced piezoresistance changes is recorded by the corresponding voltage change across the piezoresistor. In this sensing scheme, the piezoresistive element is designed to be located at the anchor point between the flexible structure and the fixed device substrate. This will allow the piezoresistor to experience the maximum stain and thereby the largest piezoresistance change. Benefiting by the design simplicity, the cantilever beam is one of the popular mechanical structures, which is commonly used in the MEMS sensor designs [79-85]. In the case of cantilever based piezoresistive flow sensor, the piezoresistive sensing element is embedded at the fixed end of the suspended cantilever clamped on the substrate. Thus, the flow induced cantilever deflection will be ultimately transferred to piezoresistance changes.
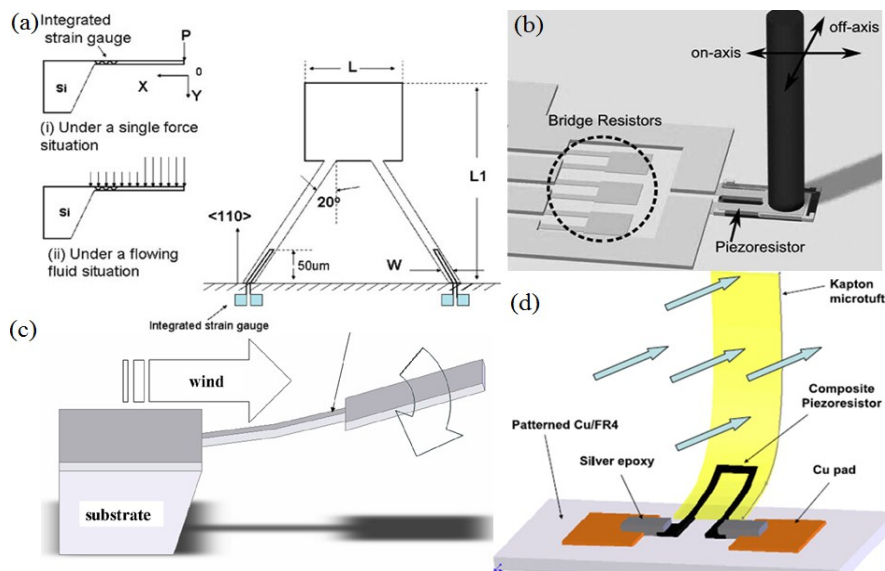
Figure 1. 15 Various research works on the cantilever shaped air flow sensor for (a) changing the cantilever size/effect sensing area [86], (b) biological hair cell design by transferring horizontal force to   vertical displacement [87], (c) pre-curved cantilever by manipulating the residual stress [89], and (d) an all polymer based cantilever shaped air flow sensor with conductive elastomer as piezoresistor [91].

The earliest design of such cantilever shaped flow sensor was reported in 1990s [76]. In 2000, by applying the concept of wind receptor of hairs, a 2-DOF (Degree of freedom) flow sensor with four piezoresistive sensing elements at the base was introduced [77]. Both flow direction detection and flow velocity sensing were successfully demonstrated. By increasing the cantilever length and narrowing down the supporting beam, Su *et al.* explored the relationship between the device sensitivity and its effective sensing area (Figure. 1.15 (a)) [86]. Inspired by the biological hair cell, Fan *et al.* and Chen *et al.* developed the cantilever based piezoresistive flow sensors with a vertical cilium, which was able to transfer the mechanical bending momentum from vertical to horizontal direction (Figure. 1.15 (b)) [87-88]. Through the manipulation of the residual stress, a pre-curved piezoresistive cantilever flow sensor was reported by Lee *et al.* with the highest sensitivity up to 0.0284 Ω/m/s (Figure. 1.15 (c)) [89]. After two years, the same group improved their design with maximum sensitivity to 0.0785Ω/m/s [90]. In 2009, an all polymer based air flow sensor with the sensitivity up to 66Ω/m/s was designed (Figure. 1.15 (d)) [91] and the similar work had recently been modified with an external amplification at a gain of 6 [92]. Till date, the cantilever based piezoresistive flow sensors have been well developed in terms of flow sensing performance and fabrication technology, but due to the limitation of materials used as piezoresistive sensing elements i.e. Pt stain gauge and elastomer, these recent works are not fabricated with CMOS-compatible process [89-92]. Consequently, the electrical circuit integration becomes a potential challenge at the wafer level. Li *et al.* recently reported a monolithic integrated piezoresistive cantilever flow sensor [93]. With a compatible fabrication by using doped bulk silicon wire as piezoresistor, an instrumental amplification circuit with a gain of 6.5 was successfully integrated with their MEMS flow sensor at the wafer

level. Except the advantage of the CMOS compatible process, nevertheless, this monolithic fabricated flow senor with bulk silicon piezoresistor did not show any remarkable performances in terms of device sensitivity and linearity. In addition, their device dimension was rather bulky and should consume relatively high power. Therefore, maintaining a CMOS compatible fabrication process, meanwhile improving the device flow sensing capability and scalability becomes a challenging topic in current research of piezoresistive flow sensor design.

1.2.2 MEMS Pressure Sensor

1.2.2.1 Introduction of piezoresistive pressure sensor
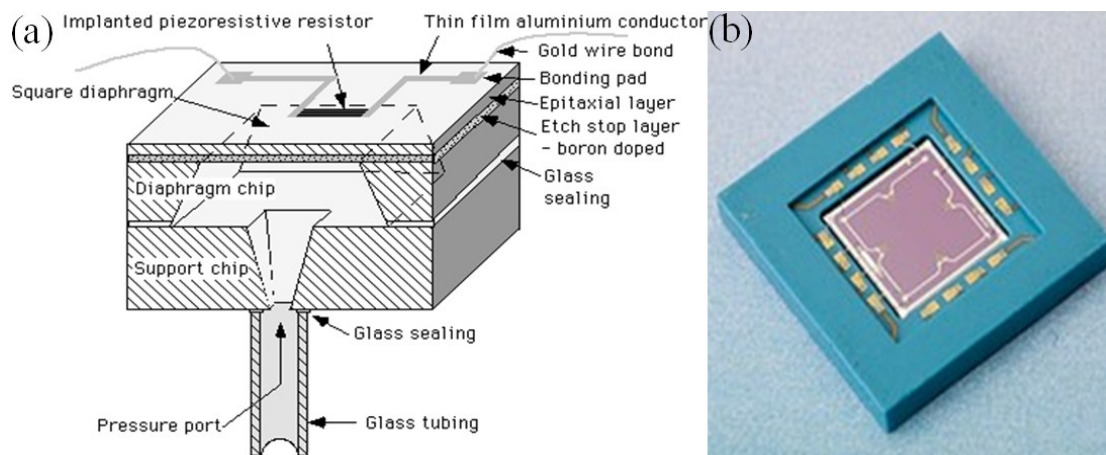
Figure 1. 16 (a) Illustration of a square diaphragm piezoresistive pressure sensor and (b) a photo of the commercial pressure sensing product.

Pressure sensor was reported and developed as one of the most traditional micromachined devices [94]. It dominated the market with 200 million units and 50% of revenues, spanning automotive, medical, consumer and even military applications as reported in 2005 [95]. The earliest piezoresistive pressure sensor was reported in late 1950s with the metallic diaphragm to sense the pressure change [96]. As illustrated in Figure 1. 16, the pressure sensor typically measure deformation/deflection of a thin rectangular/circular diaphragm under an applied

external pressure. Embedded piezoresistors (normally in pair) was fabricated at the edge of the diaphragm, where the maximum strain/stress occurred to achieve the best sensitivity of resistance change. With the significant progresses in semiconductor technology, the first silicon Piezoresistive pressure sensor was developed in early 1960s by O. N. Tufte *et al.* [5]. The pressure transducer consisting of a single crystal silicon diaphragm had stress sensitive piezoresistive regions formed by the localized diffusion of impurities. A good linearity of stress-pressure relationship was reported and in a good agreement with their theoretical predictions. In 1969, the piezoresistive pressure sensor with integrated circuit on diffused silicon was developed for air data application [97]. Following this, development of pressure sensor was extensively carried out. Various micro-fabrication technologies were explored. As shown in Figure 1. 17, Samaun *et al.* made the silicon diaphragm by using the anisotropic etching technique by KOH [98]. They claimed that such etching method was inexpensive, easy to handle and able to produce the flat sensing diaphragm. As a result, the great sensitivity improvement was achieved. Marshall at Honeywell patented the first silicon based pressure sensor through ion implantations [99].
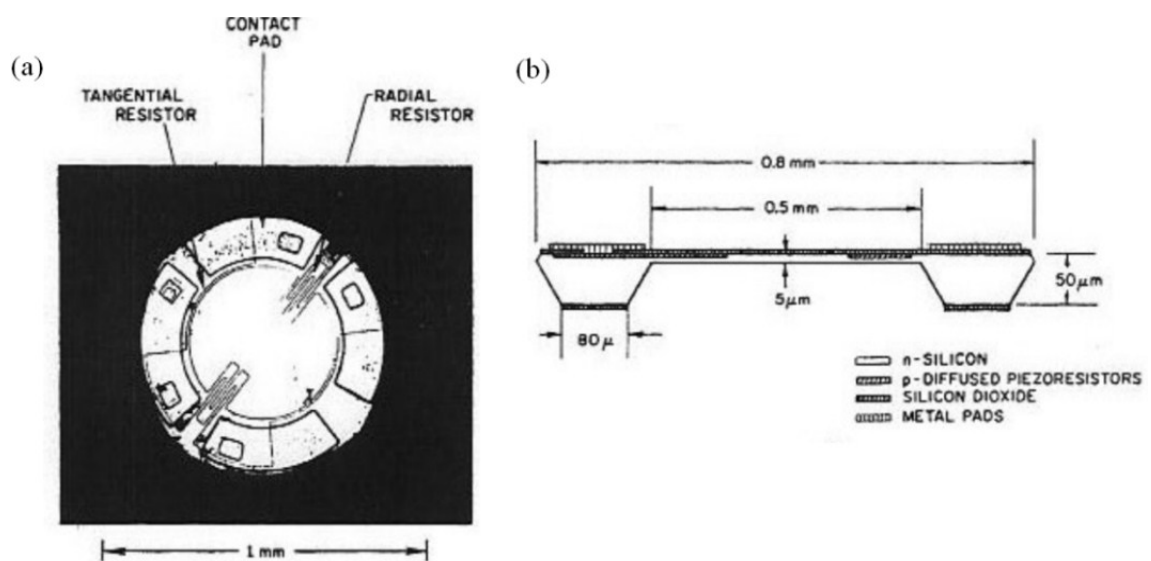
Figure 1. 17 Top view of the piezoresistive pressure sensor, (b) Cross-section of the device [98].
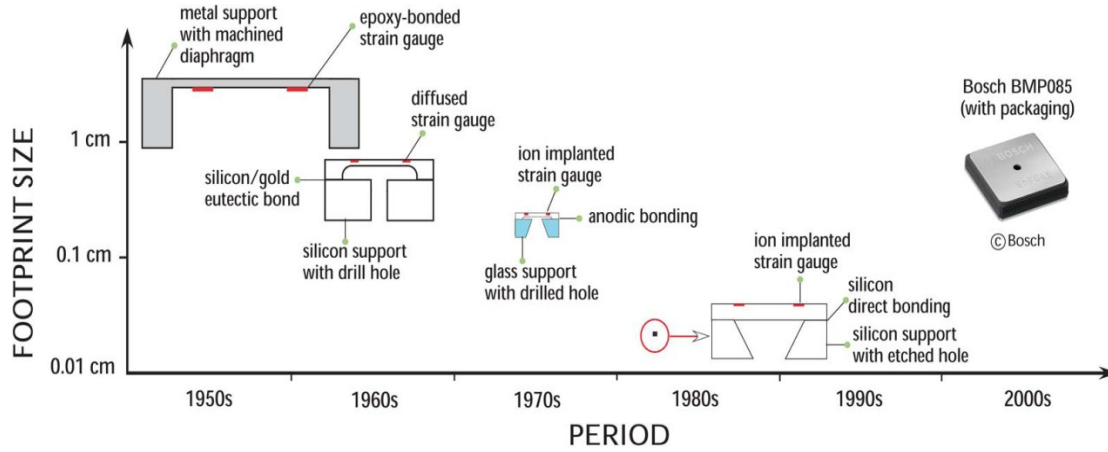
Figure 1. 18 The evolution of MEMS pressure sensors from 1950s to 2000s [33].

Motivated by the market demands, from the 1980s to now, continued improvement in fabrication technologies allowed further increase in sensitivity, higher yield, better performance with a reduced in device size. Barlian *et al*. summarized the trend of a dimension miniaturization for MEMS pressure sensor as shown in Figure 1.18 [33]. However, the conventional pressure sensor is generally fabricated through the chemical etching (e.g. KOH) through the device backside with piezoresistors patterned on the epitaxial layer (e.g. Polysilicon layer). As consequences, both diaphragm thickness and dimension of piezoresistor are relatively bulky (> 10μm), which seriously limits the sensitivity of the device and hinders its application, especially in low pressure sensing.

1.2.2.2 The boss diaphragm structure for low pressure sensing

The miniaturized pressure sensing diaphragm (e.g. diameter/length <1mm) was usually required for the special application (e.g. bio-medical related pressure sensing including intraocular pressure (IOP), intracranial pressure (ICP) and blood pressure measurement) [100-101]. In addition to the requirement of a stringent dimension, the pressure range was usually very low (e.g. pressure < 120 mmHg) under such situation. Conventional piezoresistive pressure sensor generally demonstrated a lower

non-linearity (NL) than that of the capacitive pressure sensing devices under a small diaphragm deflection range [102]. However, such conclusion did not stand in the case of low pressure sensing. For the conventional flat diaphragm based piezoresistive pressure sensor, when the thinner diaphragm with a large defection was required to sustain the minimum detectable output under a low pressure, the consequent well-known balloon effect would cause a severe degradation in device linearity [5,103].
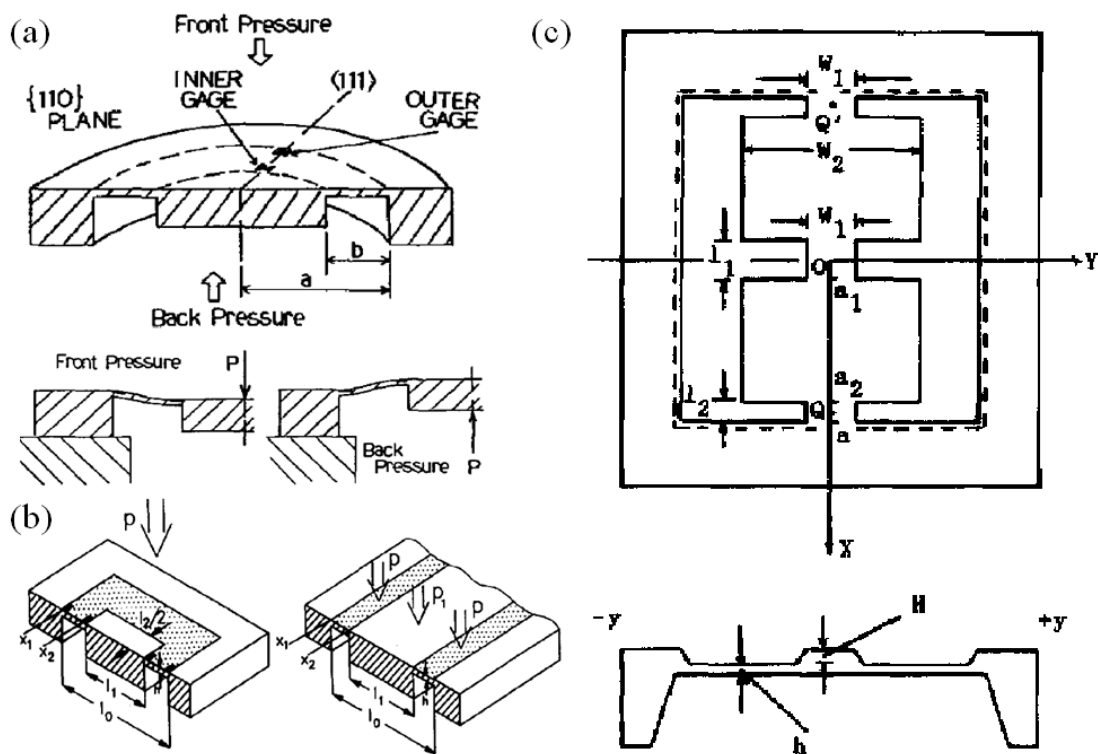
Figure 1. 19 Various design of bossed diaphragm pressure for low pressure application. (a) Bossed circular diaphragm pressure sensor [103], (b) bossed square diaphragm and an ideal plate stripe [104], (c) bossed diaphragm fabricated by front-side micromachining [105].

In order to solve the problem, a novel boss diaphragm structure, which was configured with a much thicker diaphragm in the center compared to the edge and fabricated based on bulk micromachining, was introduced to concentrate the stress distribution along the beam/rib structure without reducing overall diaphragm thickness and thus remaining a good linearity [103-104]. Taking the advantage of

surface micromachining, Bao *et al*. proposed a modified boss diaphragm by configuring those rib and groove structures on the front side of sensing diaphragm [105-106] with improved process accuracy. Further optimization efforts had been made to improve the boss device pressure sensing performance by optimizing geometry factors, such as dimensions, shapes and the ratio between length and width of such rib and groove structures [102, 107-108].

Besides, the theoretical study had also been carried out to optimize and predict the device sensitivity and linearity [6, 109-110]. Nevertheless the low pressure sensing performance of the boss diaphragm pressure sensor had been reaching its inherent limit with the diaphragm area in the range above mm^2 [102]. A further shrinkage in diaphragm diameter/length would significantly reduce the sensitivity due to a lower resultant resistivity change generated by the deflection induced stress/strain, which was proportional to the square factor of the diaphragm dimension [111]. Hence, other methods of performance improvement had to be considered for a further sensitivity enhancement.

1.2.3 Implementation of SiNWs in MEMS Physical Sensors

The aforementioned pioneer works on piezoresistive MEMS sensors verified the importance of the piezoresistance effect in the device level regarding to each special application, however, driven by market demands (e.g. device downsizing and better sensing resolution) or clinical requirements (e.g. integrated strain sensors for localized buckling mechanics), current developments of piezoresistive MEMS device in these application approaches their design bottom neck. Applying emerging nano-scale sensing element might to be the alternative solution for the continuous device performance improvement. In chapter 1.1.2, we had introduced the piezoresistance

effect of SiNWs and the feasibility of using SiNWs as the promising candidate for piezoresistive sensing. Before discussion on our detailed works, we would like to provide some works of SiNWs MEMS from other groups. These works explored several aspects relating to the practical usage of SiNWs and also helped us to identify the insufficiency and blanks reflected. In the meantime, these reported literatures also confirmed our previous SiNWs proposal for the further breakthrough over current bottom neck in current piezoresistive sensor design.

In 2009, J. H. Kim demonstrated the SiNWs embedded diaphragm pressure sensor [157]. With wet-etching technique (by using TMAH), SiNWs with cross section less than 300×300 nm^2 was fabricated from the front side (as shown in Figure 1. 20 (a)) and formed a suspending structure (shown in Figure 1. 20 (b)). In comparison to the sensitivity of pressure sensor using bulk silicon wires, the performance had been enhanced by 40 times (shown in Figure 1. 20 (c)).
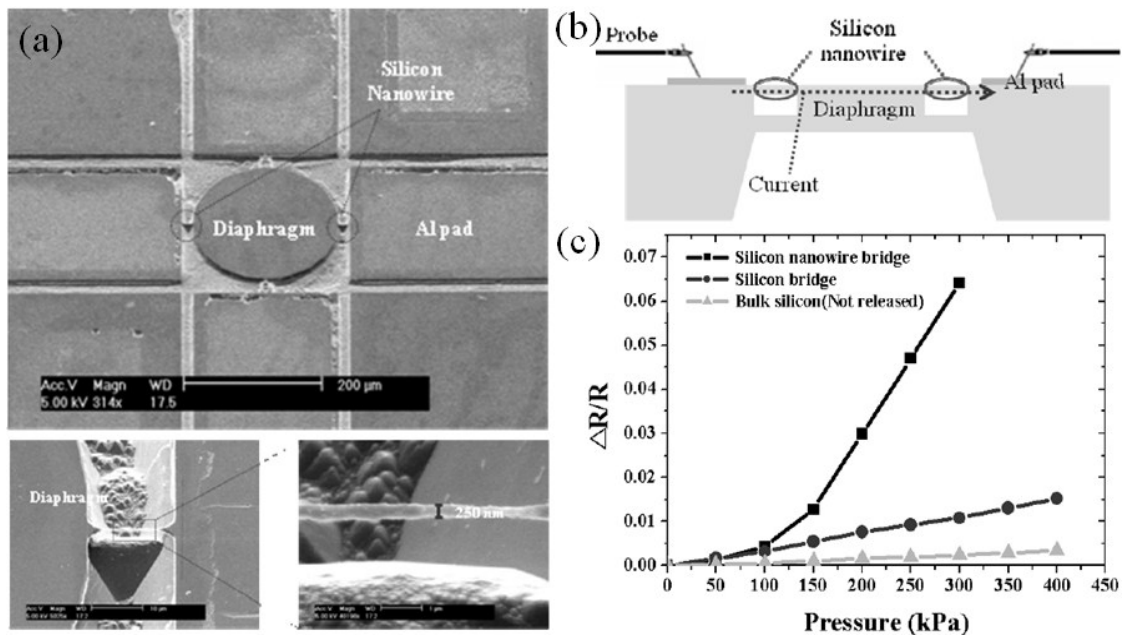
Figure 1. 20 (a) SEM images of the SiNWs embedded diaphragm pressure sensor and (b) the drawing of device cross-section. (c) A plot of device sensitivity in comparison to the pressure sensor with bulk silicon piezoresistors [157].
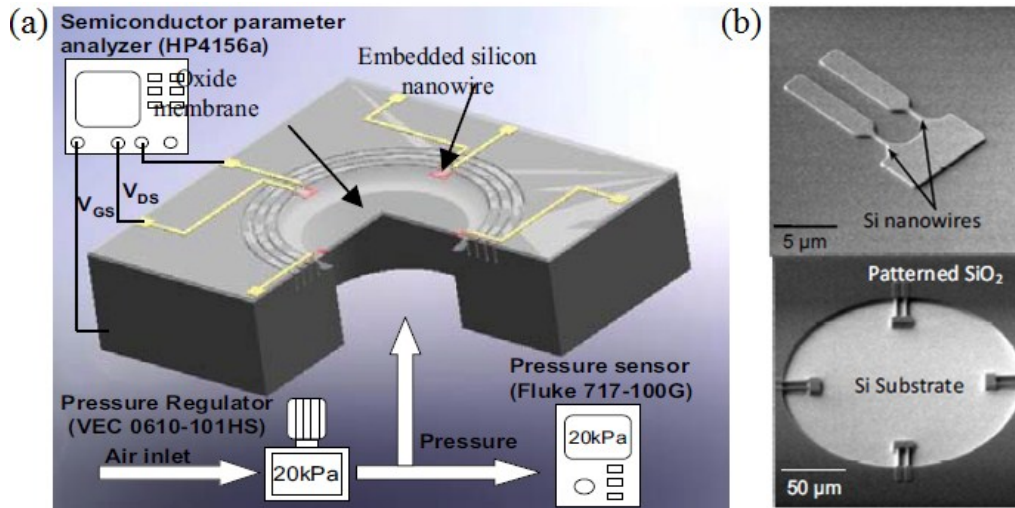
Figure 1. 21 (a) Schematics of 200μm diaphragm SiNWs pressure sensor (b) SEM image of the diaphragm and zoom-in of SiNW [158].

Soon *et al.* reported an ultrasensitive nanowire pressure with a square cross-section SiNW of 100 nm^2 [158]. As the reason concluded chapter 1.1.2, the P-type nanowire was formed along <110> for the optimized sensitivity. Except the boost of device sensitivity, the author also claimed the great scalability of SiNWs. As a result, the device with diaphragm diameter of only 200μm was fabricated and potentially capable for implantable bio-medical applications. Figure 1.21 demonstrated the (a) device drawing and (b) the SEM images of SiNWs.

In these above mentioned works, the device linearity and diaphragm structure have not been fully optimized, but their successful demonstration indicates the possibility of using SiNWs for a better sensing performance, which motivates the following works of using SiNWs for various applications.

1.2.4 Emerging Application of Piezoresistance Effect in Clinical Trials

Besides the implementation of piezoresistance effect with conventional physical sensors (e.g. flow or pressure sensor) in bio-medical applications [100-101], the application of piezoresistive sensing mechanism has become increasingly interested in clinical trials. Recently, B. Han *et al.* reported SiNWs based ring shaped tri-axial

force sensor to integrate with a surgical guide-wire for the clinical application [159].
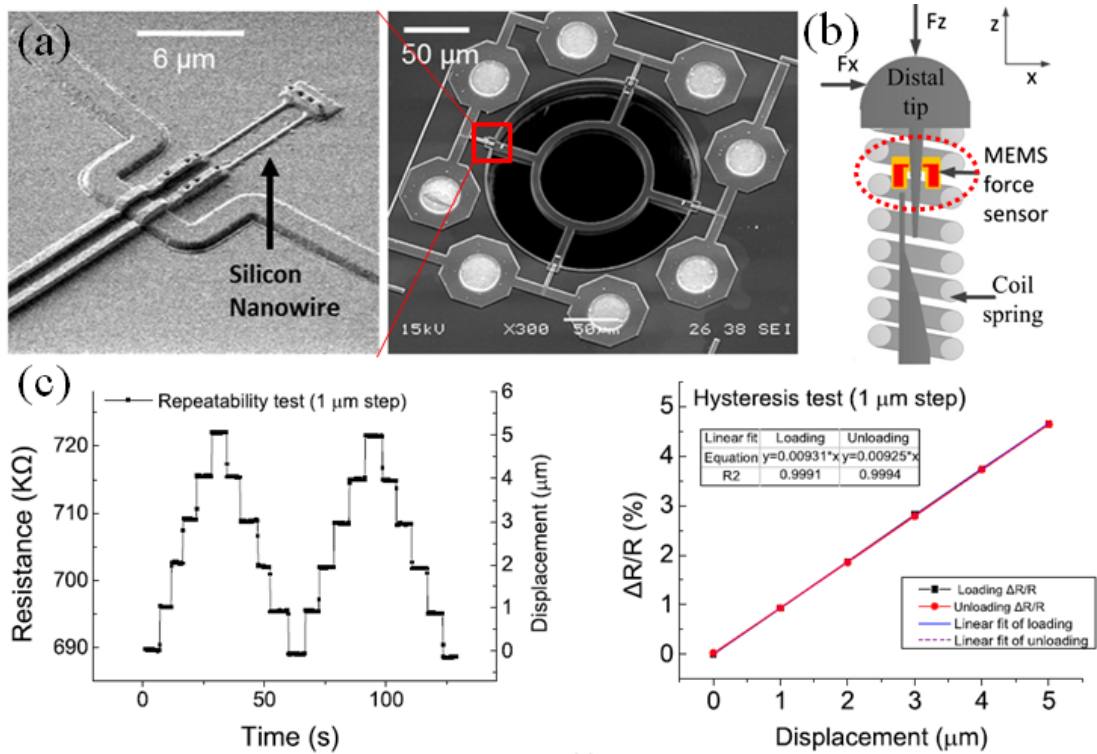
Figure 1. 22 SEM images of tri-axial force sensor with zoom-in view of 6 long SiNWs. (b) Illustrates the device working principle, the distal tip is used to sense the force. (c) Shows the device hysteresis and the extracted linearity [159].

As indicated in Figure 1. 22 (a), benefiting by the great scalability of SiNWs, the effective sensing area was controlled below 200μm × 200μm. Nevertheless, such great dimensional shrinkage did not compromise its sensing performance. As plotted in Figure 1.22 (c), both repeatability and linearity were explored for the SiNWs embedded NEMS force sensor. At the end, a detailed comparison table was summarized by the author and provided in Figure 1. 23. Compared with other reported piezoresistive MEMS force sensor, the SiNWs embedded NEMS device not only provided a better sensing resolution within a minimized sensing area, the device also performed with a reasonably good linearity.

Shear force transfer method	Application	Sensing element	Size (μm)	Sensitivity	Linearity	Force range	References
Guidewire or micro pillar	Guidewire navigation	Silicon nanowire	$380 \times 380 \times 10$	$S_{Dz} = 13.4 \times 10^{-3}\ \mu m^{-1}$ $S_{Fz} = 0.734\ N^{-1}$	0.999	20 mN	This work
Fabricated silicon rod	Minimally invasive surgery	Polysilicon piezoresistor	Diaphram: $420 \times 420 \times 7$ Post:H 470 um	$S_{Dz} = 6.0 \times 10^{-3}\ um^{-1}$ $S_{Dx} = 1.2 \times 10^{-3}\ \mu m^{-1}$ $S_{Fz} = 3.5\ N^{-1}\ S_{Fx} = 10.8\ N^{-1}$	n.a.	0–0.05 N	Hu et al 2010 [28]
Added epoxy mesa	Robotic control	Boron implanted p+ piezoresistor	$300 \times 300 \times 45$	4–6 mV/mN/V	n.a.	0–3 mN	Vasarhelyi et al 2006 [27]
Silicon mesa fabricated on the sensor	Amputees prosthesis	Boron implanted p+ piezoresistor	2.3 mm $\times$ 2.3 mm $\times$ 1.33 mm	$S_z = 0.032 \pm 0.001\ N^{-1}$ $S_x = S_y = 0.0323\ N^{-1}$	0.997	0–2 N	Beccai et al 2005 [25]
Planar structure	Grasping in robotic manipulator	Polysilicon piezoresistor	Array: 19.2 mm $\times$ 19.2 mm	$S_z = 1.59$ mV kPa^{-1} $S_x = S_y = 0.32$ mV kPa^{-1}	0.999	Normal: 0.35 mN^a Shear: 0.6 mN^a	Kane et al 2000 [22]
Attached SU8 square mesa	Hand grasping activity	Boron implanted p+ piezoresistor	Diaphragm: 1.9 mm $\times$ 1.9 mm $\times$ 50 Mesa: H 60	$S_z = 1.57\ N^{-1}$ S_x, S_y varies with loading conditions	0.98	0–3 N	Wang and Beebe 2000 [23]
Stylus attached by epoxy resin	Material characterization	Piezoresistor	5 mm $\times$ 5 mm $\times$ 0.36 mm	$S_z = 0.36\ N^{-1}$ $S_x = S_y = 13.2\ N^{-1}$	n.a.	n.a.	Bütefisch et al 2001 [24]

^{a} Unit converted from normal force range of 35 kPa and shear force range of 60 kPa to mili Newton in order to be identical to other designs.

Figure 1. 23 Summary of recently reported tri-axial force sensor designs [159].

Except of the above mentioned case, in fact, a successful demonstration of the implementation of piezoresistance effect in clinical trial was introduced as early as in 1990 [156] on the silicon neural probe. Although the neural recording function was sacrificed due to the bulky dimension of piezoresistor, Najafi *et al.* managed to include a single piezoresistor into the probe shank for real-time monitoring of the device buckling force. Before having a detailed view of their work, the progress of silicon neural probe is briefly given in the following content and it also serves as a preface for the further introduction of CMOS compatible silicon electrode probe, which will be discussed in chapter 5.

1.3 Silicon Neural Electrode Probe

Probe-shaped implantable neural prosthetic devices (NPDs) not only facilitate treatments for brain disorders, but also explore the function of neuron networks using electrical linkages through recording and stimulating respective neurons [112-113]. The metal wire based neural probes is the pioneering study in neural probe design. The electrodes typically consist of electrolytically sharpened wires that are commonly

less than 100μm in diameter and are completely insulated except for a small exposed area at the tip which forms the recording or stimulation site. The typical device images are given in Figure 1. 24 (a) and (b) [114-115].
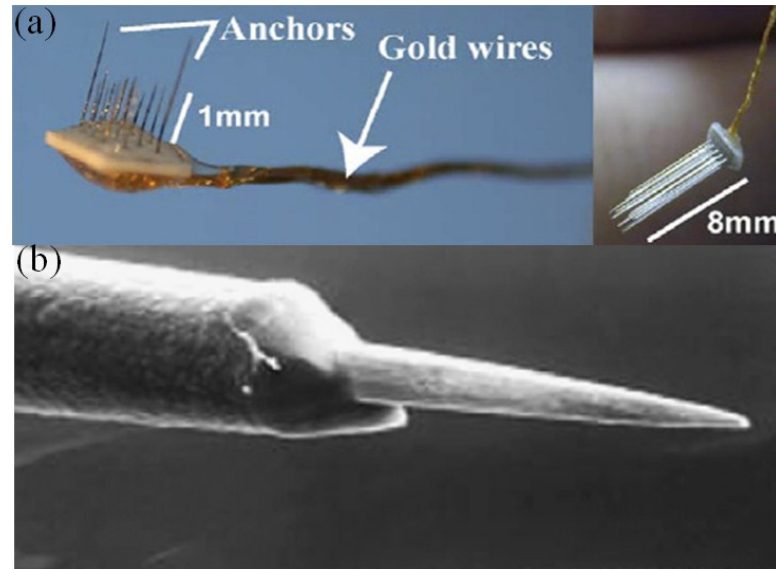
Figure 1. 24 Optical images of metallic neural probes [114] and the SEM of the probe tip (device is insulated with Parylene-C except the tip) [115].

Benefiting by the superior mechanical property [116] and progresses of semiconductor technology, the successful demonstration of silicon neural probe proved possibility of using silicon material to replace the traditional metal wires based NPDs [117-118]. Figure 1.25 shows the images of the well-known Michigan and Utah probes. Compared with pure metallic materials, silicon material standardizes fabrication processes with improved fabrication accuracy, the possibility of mass productions and extra capacities of more built-in functions (e.g. multi-functional electrodes and embedded fluidic channels, etc.) [119-124]. Tremendous researching endeavours have been devoted for both bio-compatibility and mechanical stability of the silicon neural electrode probe over chronic studies [124-127]. Meanwhile, the re-configuration of device structure and dimension has been proposed for less tissue damages [128-129]. In addition, the density of electrodes within single probe shank

demands to be largely increased for a higher resolution the neuron signal mapping [130-132]. Therefore, both aforementioned concerns require the necessary downsizing of the neural electrode, which may lead to the severe degradation for the quality of recorded neural information (e.g. neuron active potentials) against the background noise. As consequences, emerging materials (such as platinum gray [133], activated iridium oxide film [134], conductive polymers [135-136], various nano-scale materials [137-138] and even graphene [139]) are reported to be deposited on top of traditional metallic electrodes for a better charge storage capacity (CSC) [140]. Alternatively, integrated circuits including real-time processing and pre-amplifying functions are also widely deployed for a further processing of qualified neural recordings [141-143]. Furthermore, it has also become increasingly clear that the understanding of neuron networks/pathway at the system level requires the simultaneously recording and simulating behaviours from many sites in three-dimension (3D). Hence, great attentions have been focused on the fabrication of neural electrodes/probe arrays arranged in 3D structures [117-118, 144-147].
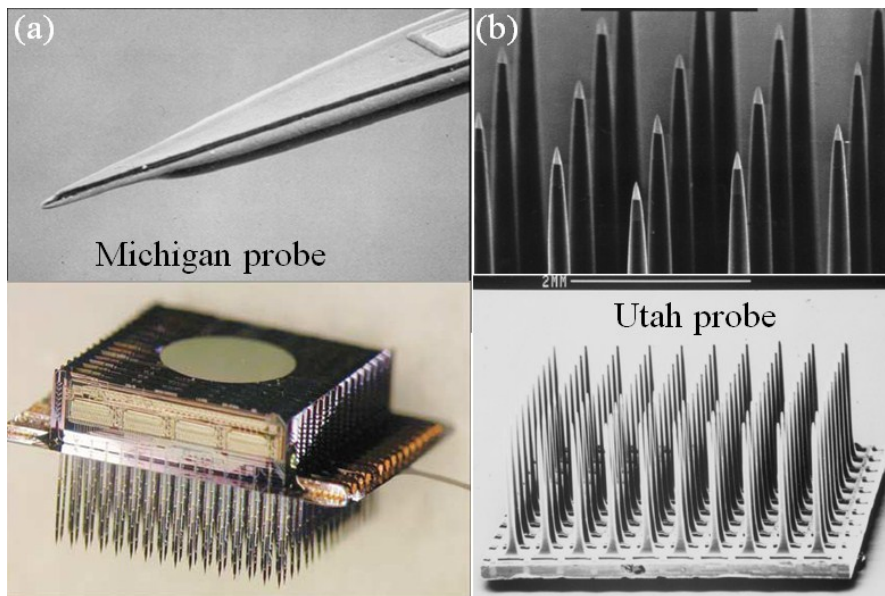
Figure 1. 25 Device images of well-known (a) Michigan probe array and (b) Utah probe array.

Enormous amount of raw recording data from high density probe arrays normally demands preliminarily processing and filtering before further analyses [117]. Thus, the integration of CMOS circuits onto the microelectromechanical system (MEMS) fabricated silicon neural electrode probe becomes vitally important. Reports of successful on-chip integrations have been widely introduced, but most reported devices reply on complicated post-fabrication process [130, 148]. In another word, the built-in integrated circuit is defined prior to the fabrication of recording/simulation electrodes due to the process incompatibility between the standard CMOS fabrication and the sequential MEMS process (e.g. Deposition and metallization of neural electrodes).

Except inherent properties between neural-electrode interfaces along the probe, the device insertion mechanics is always pertaining to final quality of recorded signals [149]. Optimization of tip, width and thickness of the implantable probe is crucial to reducing the tissue dimpling and the following tissue response after penetrations [150-151]. Additionally, the insertion speed during the process is also critical to the control of penetration forces and consequent initial damages [152-153]. Moreover, the correlation between the recorded neuron signal and the exact location/depth of the recording site is often necessary for the correct interpretation of functions of respective neural networks. Hence, the force gauge/load cell is usually applied to closely monitoring probe insertion behaviours. As a common practice, the external load cell is connected to the base of the implantable device and perpendicular to the brain tissue surface as demonstrated in Figure 1. 26 [153].
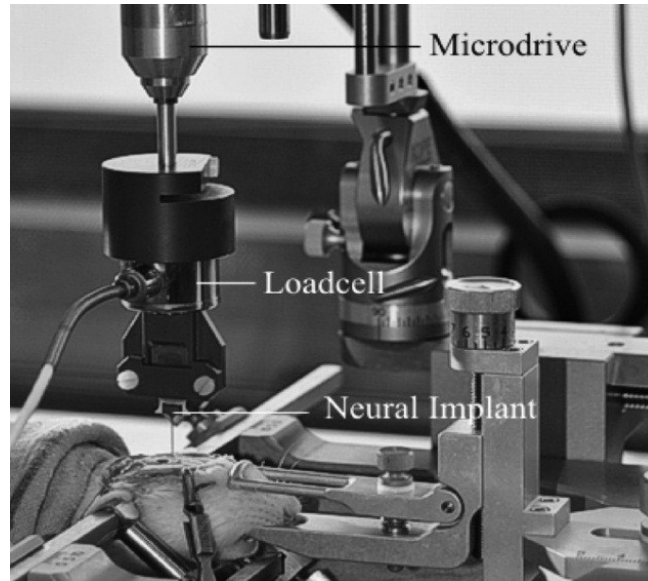
Figure 1. 26 The stereotactic probe implantation setups with an external load cell to measure the vertical compressive or tensile forces [153].

During the insertion, a normal bending force induced on the probe shank will be transferred to readings obtained from the load cell. After the load exceeding the critical buckling force, however, the actual probe deformation is hard to be measured by feedback readings from load cell since presences of both torsion and bending mechanics rather than purely bending case [154]. Nevertheless, a larger deformation is able to be continually monitored by strain changes till the complete fracture [155].
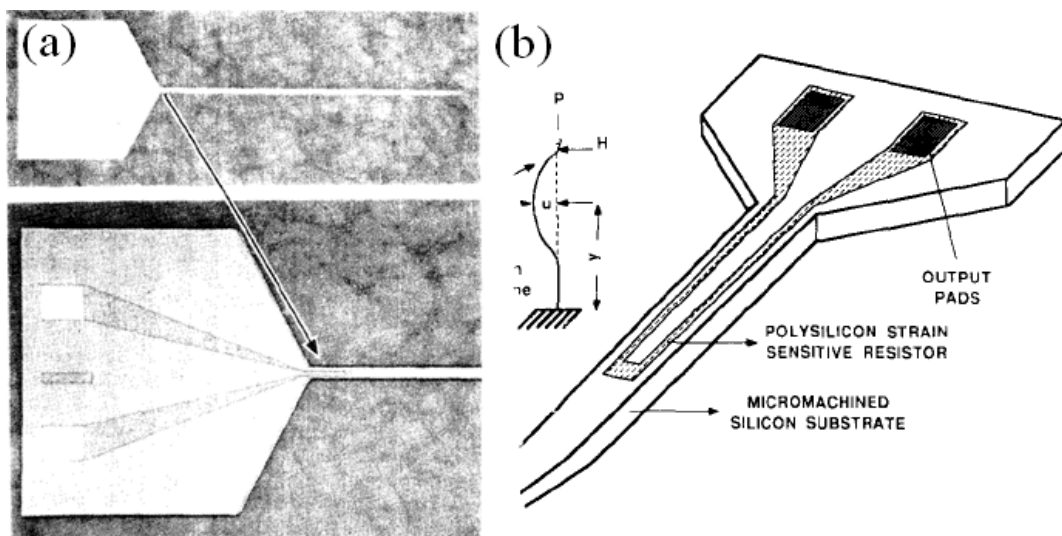
Figure 1. 27 (a) Optical images of the strain measurement probe, and (b) schematic design of the probe structure [156].

Taking advantage of the unique relationship between deformation and induced strain along probe shank, Najafi *et al.* [156] reports the silicon probe with an embedded piezoresistive strain gauge for the monitoring of probe insertion mechanics. As shown in Figure 1.27, the corresponding resistance change from the integrated polysilicon piezoresistor provides the information such as extent of tissue dimpling, the exact moment of penetration and the correlated surface stress. Such strain sensor design can be further extend into current 3D array designs with monitoring of localized mechanical information in each individual probe. However, limited by the bulky dimension of polysilicon sensing element in their prototype design, apart from the lack of recording electrodes at the probe tip, only single piezoresistor is available rather than the commonly applied bridge structure consisting of four counterparts. Thus, the emergence of new piezoresistive sensing element is indispensible for further design enhancements.

1.4 Motivation of SiNWs embedded NEMS Piezoresistive Device

In conclusion, the successful demonstration of piezoresistance effect is not only applied in conventional physical sensing device (e.g flow and pressure sensor), its functionality has also been extended into clinical field as an integrated sensing element on the implantable device (e.g. guide-wire, silicon neural probe). However, either the traditional epitaxial piezoresistors or bulk silicon piezoresistive elements have been revealed with distinct drawbacks against the current market trend of building low cost, low power consumption, miniaturized and high performance sensing device. Furthermore, the on-chip integration with other peripheral circuits would be substantially beneficial for establishing the systematical sensing network. In

order to realize such visualizations, the utilization of SiNWs would provide the possibility for the future technology migration. The reported SiNWs based NEMS sensor demonstrates a good sensing capability compared with their counterpart using the conventional piezoresistors. In addition, the miniaturized dimension of the SiNWs NEMS device implicates the potential of using SiNWs piezoresistive sensor in bio-medical or clinical application for an advantage of a less invasion. Therefore, it is worthwhile to devote further research efforts to explore the potential of SiNWs as the NEMS sensing element with specific application in this thesis.

As the fundamental factor related to the final performance, we will firstly discuss detailed optimization process of SiNWs and the fabrication techniques on NEMS device. By using the device layer (single crystal silicon layer with thickness of 110nm) on (100) plane SOI wafer, the dimension of both sensing element (e.g. piezoresistor) and sensing structures (e.g. cantilever or diaphragm structure) can be significantly reduced. In chapter 3 to chapter 4, the detailed design consideration of conventional physical sensor will be explained based on different applications and device configurations, for instant, cantilever shaped air flow senor and diaphragm based pressure with annular grooves for low pressure sensing. After further leveraging the process compatibility, both neural recording electrodes and built-in strain gauges are managed to be integrated along a single probe shank, which will be discussed in chapter 5. The following up work and suggestion of future improvement will be addressed in chapter 6.

Chapter 2   Fabrication and Optimization of SiNWs Embedded NEMS Device

Besides the layout/structure design, the fabrication process is always crucial to the performance of the final MEMS device. It has been previously mentioned that the significance of the piezoresistance effect of SiNWs highly depends on the doping profile (e.g. doping concentrations, doping uniformity). In addition, the optimization of piezoresistance changes along strain applied direction is substantially important for a better sensitivity of the design. Therefore, the transverse stress component has to be minimized (see equation (1.5)). Apart from the device structure design, such minimization will be affected by the nanowire cross section, which can be controlled through the photolithography and etching processes [15]. Moreover, the contact resistance between metal interconnects and the beneath doped silicon layer determines initial resistances and the performance of nanowires. Multi-layer of passivation (cladding layers) introduces the different stress issue, which may potentially jeopardize the whole purpose of the initial design. In the following section, fabrication details of SiNWs based NEMS sensor will be discussed. Various process considerations and optimization process will be introduced.

2.1 Top-down Processes for SiNWs Fabrication

2.1.1 General Fabrication Steps

In our case, all SiNWs based NEMS device are fabricated on (100) plane 8 inch SOI wafer through top-down processes. The device silicon layer is 117 nm and buried

oxide (BOX) layer is 145 nm (Manufacturer: SOITEC) as depicted in Figure 2.1 (a). The device layer is initially N-doped with the estimated doping level of 1.5×10^{15} cm^{-3} (deduced from the nominal resistivity, which is in the range from 8.5 $\Omega \cdot$cm to 11.5 $\Omega \cdot$cm). In order to maximize the piezoresistive effect in <110> direction [34], 1st P-type implantation using BF2+ is performed with a dosage of 1×10^{14} ion/cm^2 (twist 22°, tilt 7°, implantation energy ~ 50KeV) as depicted in Figure 2.3 (a). After implantation, the carrier is activated by the rapid thermal annealing (RTA at 1050°C for 30 sec). To increase the visibility during the inspection, 320 nm thick photoresist (Model: JSR M221Y) with BARC (Model: AR3-600) is coated on the wafer. Followed by the first photolithography carried out by Nikon Scanner (Model: 203B), the SiNW pattern is formed along <110> crystalline orientation with initial width of 160 nm. The photoresist is then trimmed for 60 sec by the plasma induced feeding gas (He/O$_2$ + N$_2$) and the critical dimension is approximately decreased to 110 nm. After deep reactive ion etching (DRIE) for SiNWs formation (as shown in Figure 2.3 (b)), the photoresist ashing (O$_2$ + N$_2$ at 250°C) is performed for 2 mins. Dilute hydrochloric acid (DHF~1:100) and Piranha cleaning are carried out to remove the etching residue and the organic residue respectively. Sequentially, thermal dry oxidation (875°C for 120 mins) is conducted to further shrink down the dimension of SiNWs. As a result, the SiNWs with average cross section of 90 nm × 90 nm and various lengths (1μm, 2μm, 5μm and 10μm) have been fabricated. Figure 2.1 (a) provides the SEM image of the 2μm SiNWs with the inset of the zoom-in feature. The trapezoidal shaped cross-section with an average area of 90 × 90 nm^2 is confirmed by the TEM image as shown in Fig. 2.1 (b).
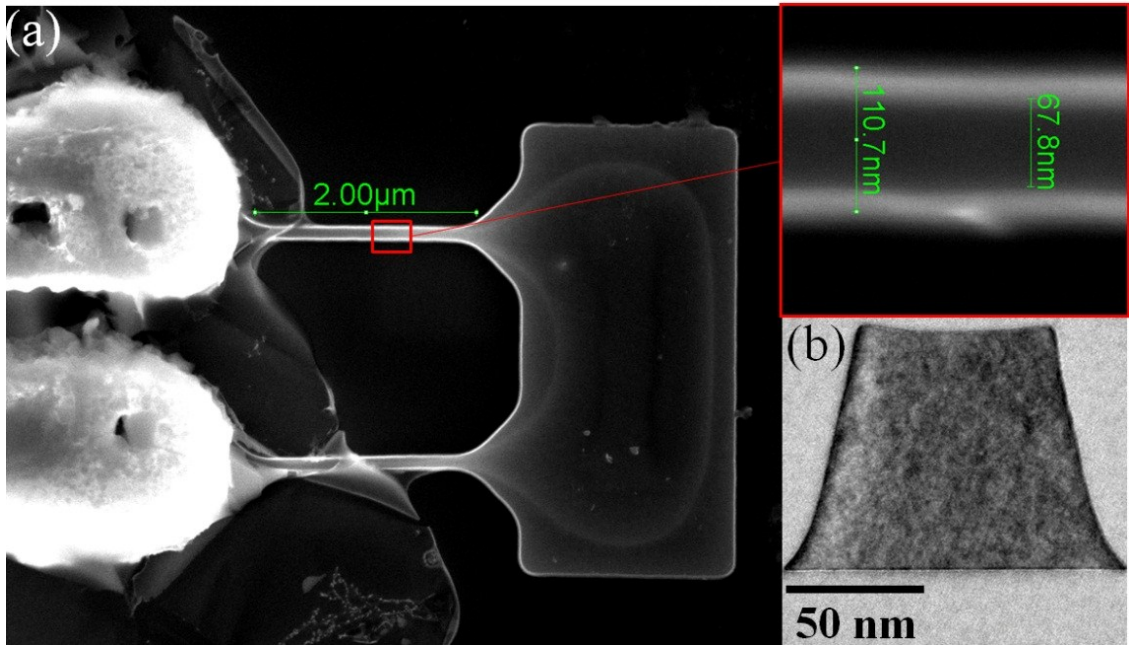
Figure 2. 1 SEM of 2μm SiNWs with a zoom-in of the top view. (b) TEM image of cross-section of nanowire.

By using 1 photoresist as hard mask, the 2nd P-type implantation is performed with a dosage of 4×10^{15} ion/cm^2 (implantation energy ~ 35KeV) at only contact paddle region on the silicon layer (Figure 2.3 (c)). After removal of photoresist, RTA (1050 °C, 30 s) is then conducted for the dopant activation. Based on the measurement from the test structure (a rectangular silicon block with dimension of 330 μm × 100 μm × 110 nm and resistance of 400 Ω), the estimated impurity carrier concentration is around 1×10^{20} cm^{-3}. A 400nm plasma-enhanced chemical vapor deposition (PECVD) SiO$_2$ is then coated as the first passivation layer. After via opening on the passivation, the last P-type implantation is performed with a dosage of 4×10^{15} ion/cm^2 at only via region (Fig. 2.3 (d)). 3rd RTA process is then carried followed by another DHF (1:100, 30 s) to remove the native oxide at via opening. With a time-link between previous step, 15s ion bombardments are performed prior to sputtering of 750nm aluminum. A metallization is completed though a BARC opening and the dry etching process as shown in Figure 2.3 (e). A good ohmic contact between

the metal and highly doped silicon layer is confirmed through the Kelvin structure as given in Figure 2.2. The typical contact resistance is around 30 Ohms. It is relatively negligible compared with the resistance of SiNWs. The 2nd passivation of low stress silicon nitride layer (tensile stress ~ 100 MPa) is coated by PECVD as shown in Fig. 2.3 (f). We will discuss the function of the nitride layer and the choice of layer thickness (range of 1 ~ 2.5 μm) in the following section (chapter 2.3). As indicated in Figure 2.3 (g), the passivation layers re-open is carried by front side RIE process. Due to the high material selectivity of the etchant, the bond-pad opening process is normally carried out in the high power RIE etching chamber with a 20-30% over-etching allowance. In case of etching passivation layers (thickness ~ 1.5μm) and stopping on silicon electrodes (thickness only ~ 100nm), the etching recipe should be verified before further processing.
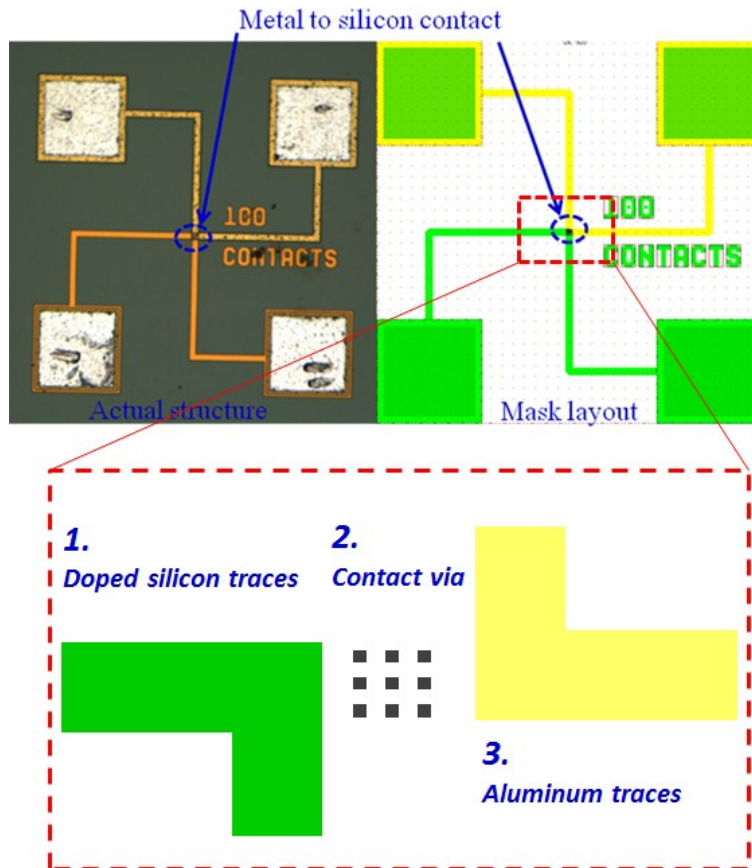
Figure 2. 2 An optical image and the layout drawing of Kelvin contact resistance measurement structure. Inset shows the overlapped three structures.

(a) 1st P-doping, dosage ~ 1×10^{14} ion/cm^{-2}

(b) Si nanowire   Si electrodes

(c) 2nd P-doping, dosage ~ 4×10^{15} ion/cm^{-2}

(d) 3rd P-doping, dosage ~ 4×10^{15} ion/cm^{-2}

(e)

(f)

(g)

Si (Device)   SiO$_2$ (BOX)   Si (Substrate)

PR   Al   SiO$_2$ (PECVD)   Si$_3$N$_4$
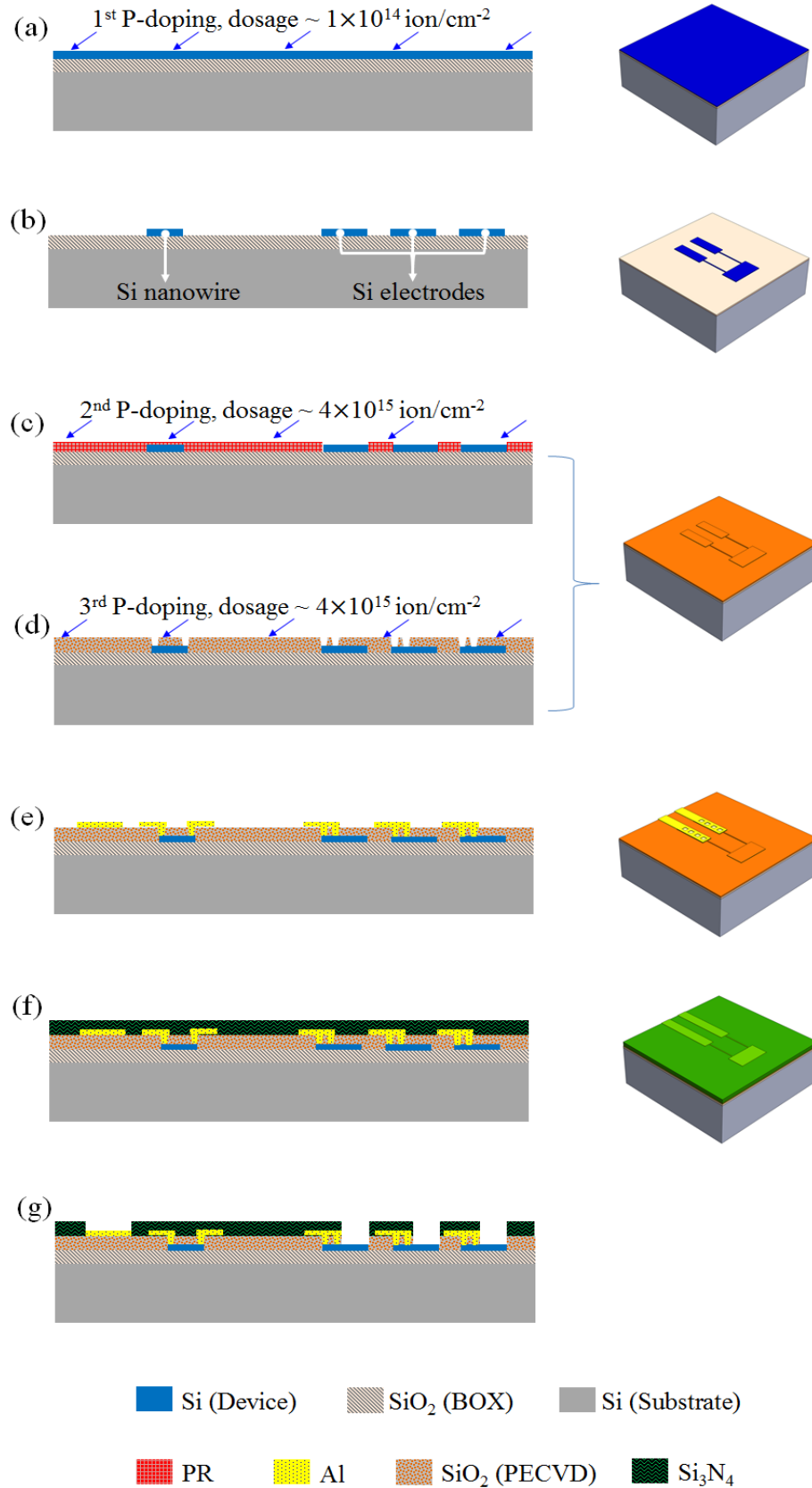
Figure 2. 3 General process flows of SiNWs embedded NEMS sensors. (a) 1st global implantation, (b) Feature patterning, (c) 2nd implantation (high dosage), (d) 1st passivation (SiO$_2$), via opening and 3rd implantation, (e) metallization, (f) 2nd passivation (Si$_3$N$_4$), (g) Bonding pad/electrodes opening

2.1.2 Fabrication Challenges

In the following section, some fabrication challenges will be addressed. Optimum solution will be introduced and it might be helpful for the fabrication of the SiNWs based sensors/designs in future.

2.1.2.1 Fabrication of silicon nanowires

It has been widely reported that both overall cross-section area affect the piezoresistive performance of nanowire [15]. Particularly, higher aspect ratio between thickness and width results in a much higher gauge factor for a given cross-section area (shown in Figure 2.4) [14]. Therefore, it is highly desirable to fabricate the nanowire with small overall cross-section and larger aspect ratio.
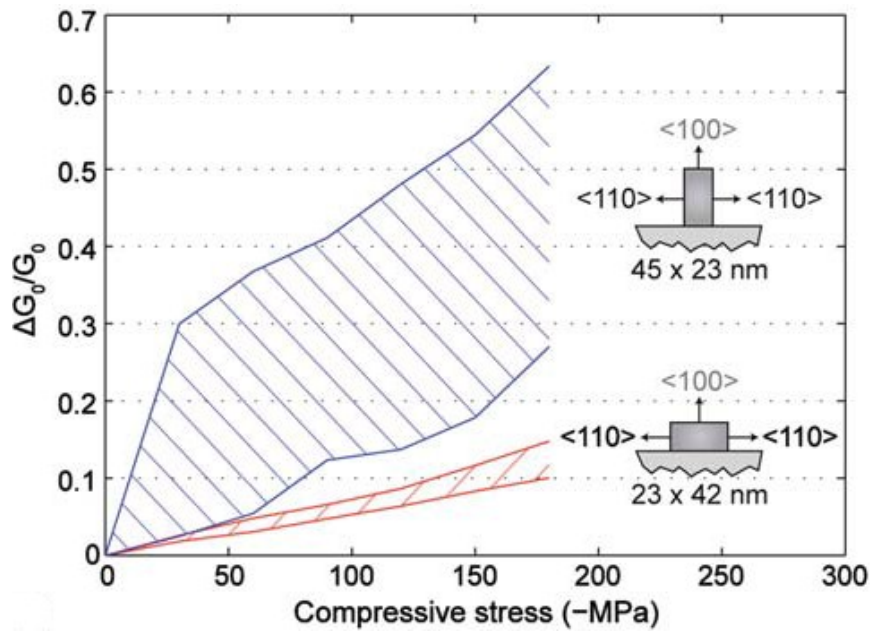
Figure 2. 4 Impact of nanowire aspect ratio on gauge factor [14].

In our fabrication steps, PR trimming technique is firstly applied to reduce the nanowire width from 160nm to 110nm. Final cross-section geometry is achieved through further dry oxidation (~ 20nm). We will briefly discuss both technique and address the reason for the combination of two in the following contents.

PR trimming is basically reducing the width of the photoresist to develop the smaller feature after the following RIE process. A straight side wall profile of the photoresist is substantial to avoid the pattern transfer issue. Longer trimming cycles will shrink the PR pattern, but it is difficult to maintain the profile, thus a severe pattern transferring effect will lead to the unwanted etching result. Figure 2.5 provides the SEM photos of etching result of a 1μm SINW with different PR trimming duration. After longer trimming steps, the SiNW pattern is no longer straight and the different of the nanowire width at top and bottom is huge.
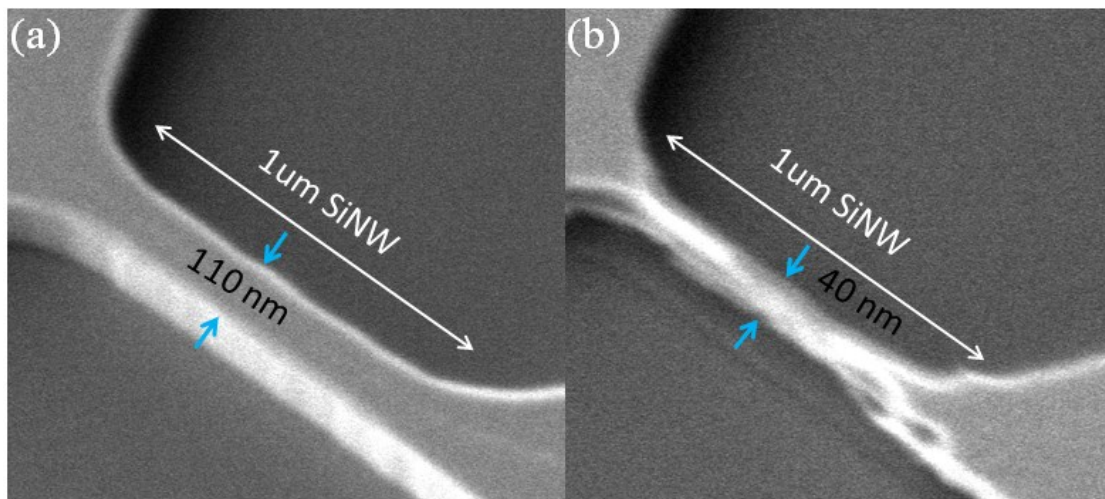
Figure 2. 5 SEM pictures for the etching result of 1 μm SiNW with (a) 60 s PR trimming and (b) 100 s PR trimming.
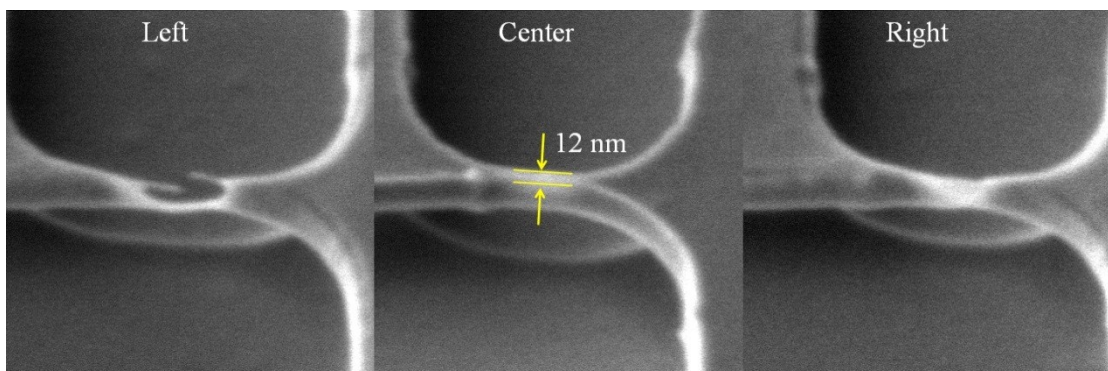
Figure 2. 6 SEM photos of 500 nm long SiNWs at left, center and right on the same 8 inch wafer.

On the other hand, dry oxidation process also can bring down the cross-section geometry of the nanowire. However, it is quite time consuming. In general, the oxidation of 10nm silicon requires more than 1 hour. Additional time consumed for chamber temperature ramping (both up and down) should also be included. Moreover, the uniformity control of the oxidation over 8 inch wafer can be even harder as the increase of the overall oxidation duration. Figure 2.6 indicates the deviation of nanowire geometry after 1 day oxidation on the same 8 inch wafer. SiNW at the left of the wafer has partially been broken. While at the center and the right, SiNWs are still continuous, although the geometry difference is obvious. Thus, it is reasonable to combine both shrinkage techniques to have better cross-section shape with less time and cost consumed.

2.1.2.2 Metallization and annealing

After the sputtering of the aluminum (Al) layer, the photolithography process is carried out for dry etching of Al layer. Due to the reflection issue, it is challenging to expose the photoresist with optimum recipe (focusing & dosage), hence it is important to use Bottom-Anti-Reflective Coatings (BARC) layer (normal thickness ~ 60nm) beneath the photoresist. For instance, for a metal block with designed dimension of 4μm × 8μm, SEM photos of the final etching results for both with or without BARC layer are demonstrated in Figure 2.7. Final Al patterns are highlighted in yellow. The difference in etching profile is quite obvious. The shrinkage of the pattern size is up to 21% without introducing BARC during the exposure (indicated in Figure 2.7 (a)). In the case of presence of beneath BACR layer (shown in Figure 2.7 (b)), the almost exact feature can be obtained (pattern shrinkage < 5%).
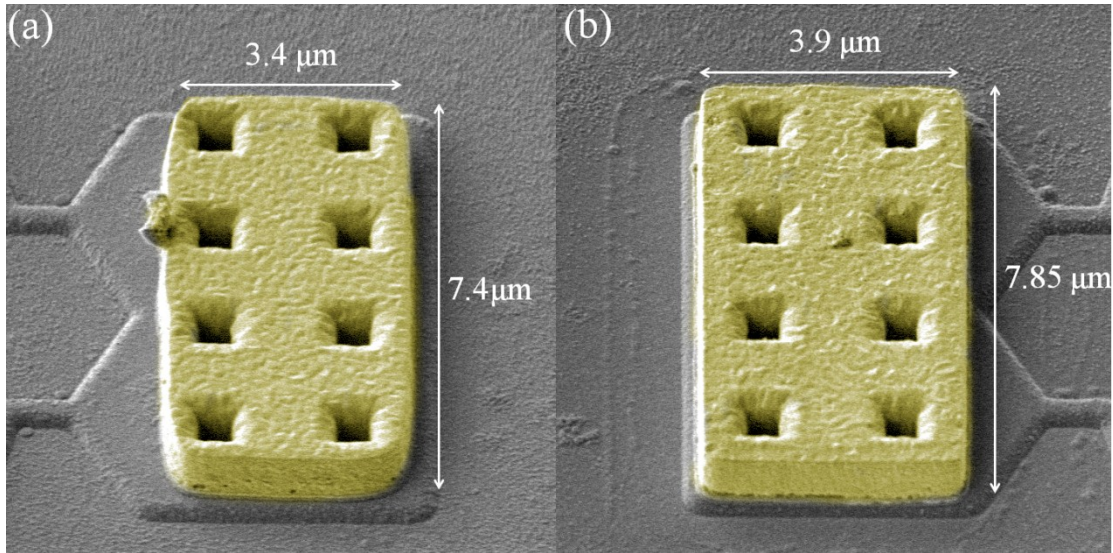
Figure 2. 7 SEM photos of Al patterns after etching (a) without BARC layer and (b) with BARC layer introduced.

After proper patterning of metal layer, the sintering (with N_2 gas purging) process is then performed to further reduce the contact resistance. For the sintering of materials, general four mechanisms exist depending on the temperature. They are the viscous flow, internal diffusion, surface diffusion and the vaporization.   In the case of lowering contact resistance, it is desirable to have the partial silicon (at the Si-Al interface) been consumed by Al. However, the processing temperature is important to prevent the "spiking" issue (fast over-consuming of silicon), which catastrophically short the adjacent pads/traces. Generally, the temperature should be around be higher than 350°C to ensure the effective heat treatment process [160]. Figure 2.8 shows the reported data of contact resistance changes with respect to sintering temperature [161]. In our case, the temperature of 420°C is chosen and the final contact resistance is ~ 30 Ohms.
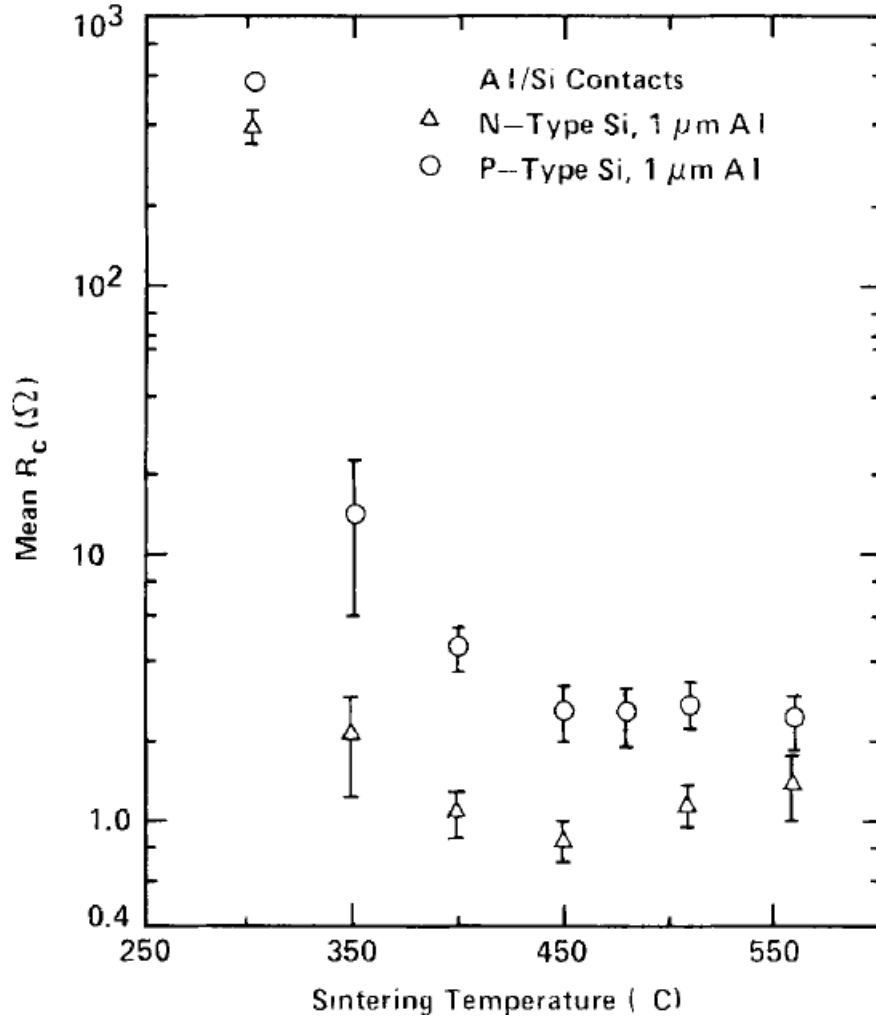
Figure 2. 8 Al/Si contact resistance as a function of sintering temperature. The sintering was carried out for 5 mins with N_2 gas flow [161].

2.2 Optimization of Doping Profiles for Various Applications

We have briefly discussed the effect of doping concentration on the piezoresistance effect and the linearity of the SiNW performance. Therefore, it is necessary to optimize the implantation dosage before starting fabrication of SiNWs based NEMS sensor. BF_2+ is firstly implanted into the silicon with different dosage level ranging from 1×10^{11} cm^{-2} to 1×10^{14} cm^{-2}.
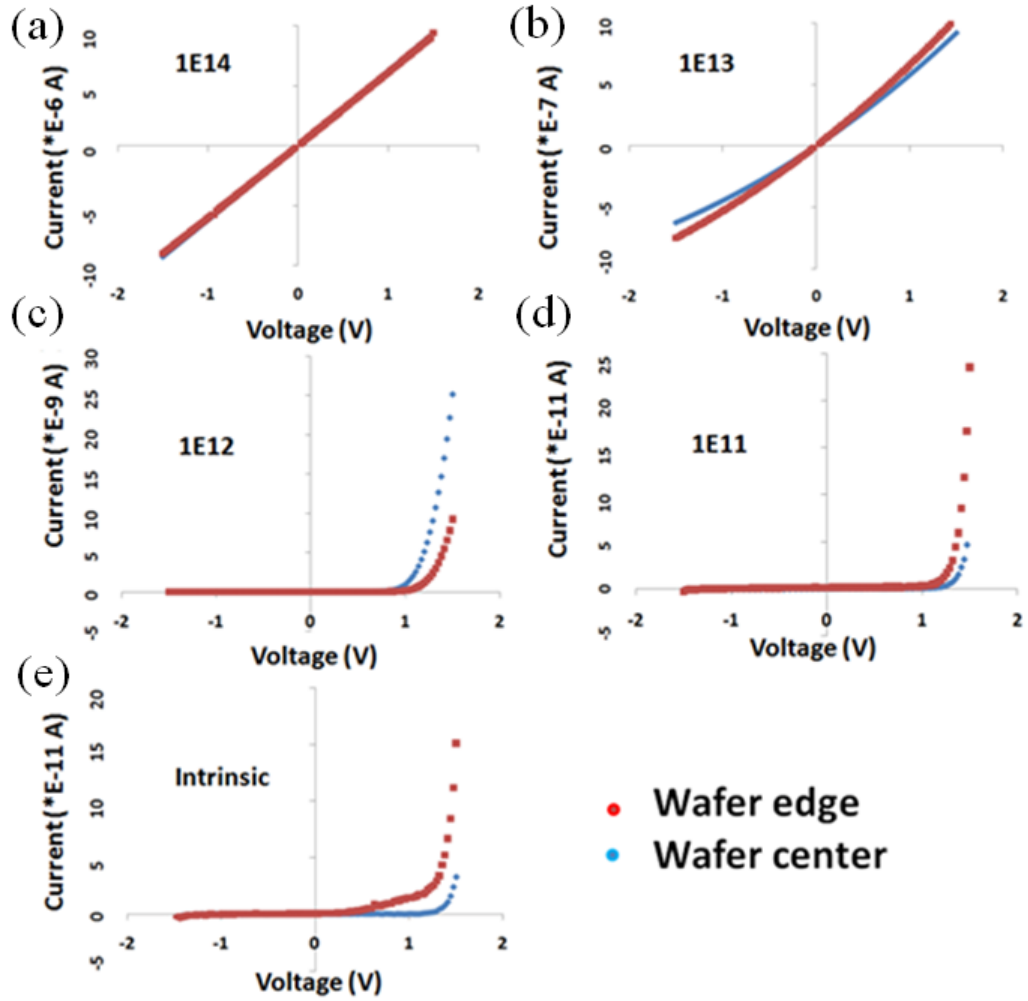
Figure 2. 9 I-V curve measurement of SiNW with different dosage of implantation from (a) 1×10^{14} cm^{-2} (b) 1×10^{13} cm^{-2} (c) 1×10^{12} cm^{-2} (d) 1×10^{11} cm^{-2} (e) intrinsic.

As shown in Figure 2.9, I-V curves of 5μm SiNWs at the wafer edge and center are measured using the parameter analyzer (Keithley 4200-SCS). A voltage sweep ranging from -1.5 V to +1.5 V is applied to the SiNW to avoid joule heating effect. As plotted in Figure 2.9 (a), the SiNWs (dosage of 1×10^{14} cm^{-2}) shows very good linearity and indicates a pure resistive behavior. In addition, the I-V curves extracted from the wafer center and edge perfectly overlapped each other, indicating good uniformity across the wafer. On the other hand, when the SiNW dosage level is lower than 1×10^{11} cm^{-2} (Figure 2.9 (c) to (e)) the SiNW shows rather high resistance, resulting in very low current of pico-ampere (pA) magnitude with obvious nonlinear biasing range. The variation between wafer center and edge also becomes more

distinct with the lower dosage level. Such I-V curves of SiNW with clear non-linear phenomena are probably due to Schottky effect. This is especially obvious for the intrinsic SiNW and SiNWs with doping of 1×10^{11} cm^{-2} and 1×10^{12} cm^{-2} i.e. Figure 2.9 (c), (d) and (e). As the positive bias increases, the width of the Schottky barrier becomes narrower. This is evident from the tunneling effect appearing at around 1.5 volts where the sudden current jump shows. On the contrary, the negative bias makes the tunneling current relatively harder to form because it tends to widen the width of the barrier. Thus the current jump does not show in the negative voltage region in the I-V curve. With our experimental findings, this is reasonable to concluded that the reported so-call "Giant piezoresistance" effect (refer to Chapter 1.1.2.1) may vary with a large non-linearity and be too sensitive to be implemented for the piezoresistive MEMS sensor design.
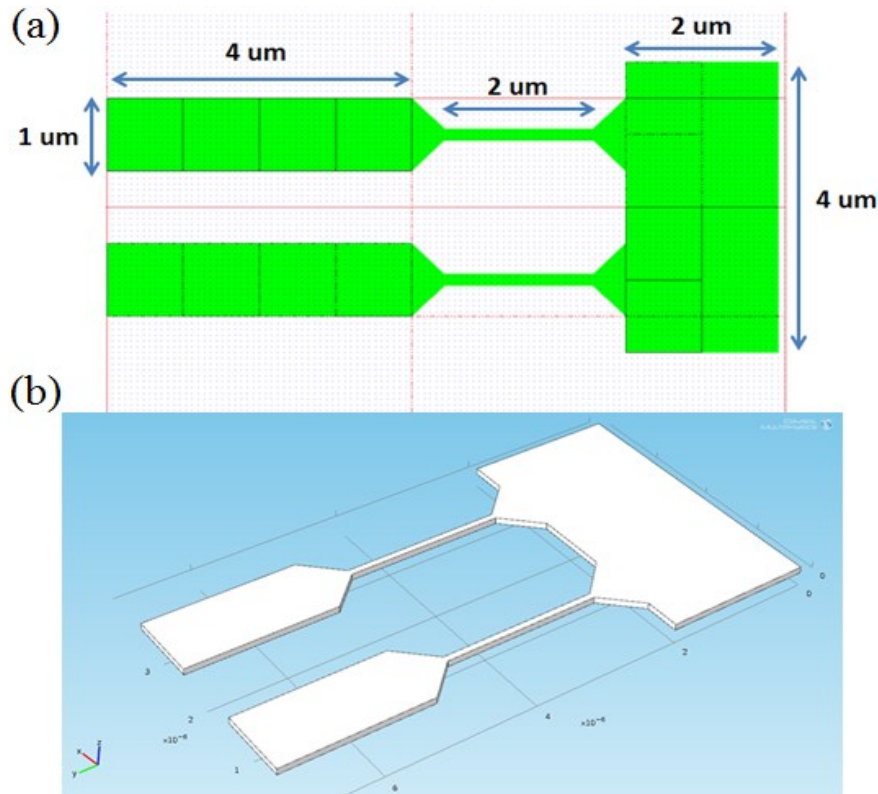
Figure 2. 10 (a) Layout of a 2μm long SiNWs, and (b) COMSOL model for resistivity extraction.

The resistance of the 2μm SiNWs is measured around 100 KΩ. The doping concentration of the SiNW (dosage of 1×10^{14} cm^{-2}) is deduced through the combination of both FEM modeling and theoretical study. Firstly, the COMSOL Multiphysics was conducted to extract the resistivity of the p-type doped silicon. The structure used in the COMSOL modeling (Figure 2.10 (b)) strictly follows the structure in the mask layout (shown in Figure 2.10 (a)). The extracted resistivity is around 0.021 Ω·cm. Hence, the actual doping concentration can be extrapolated from the chart introduced by M. Sze *et al.* [162]. As indicated by the blue dash line in Figure 2.11, the estimated doping concentration of our fabricated SiNWs (dosage of 1×10^{14} cm^{-2}) is around 3.5×10^{18} ion/cm^{-3}.
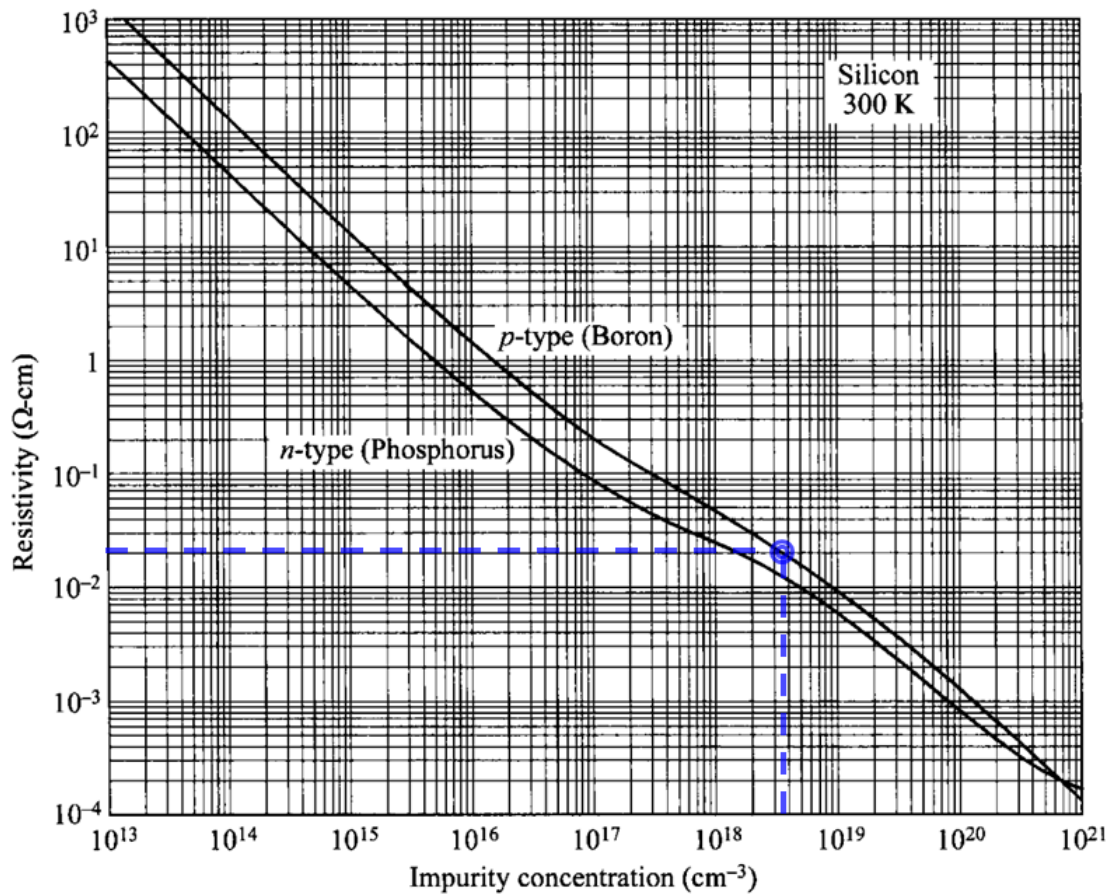
Figure 2. 11 Chart of impurity concentration *vs.* resistivity at room temperature [162].

2.3 Optimization of Passivation Layer

It's been aforementioned that the choice of the dielectric layer thickness depends on the application of the fabricated NEMS device. By using SiO_2 layer as the 1st passivation, the good adhesion with aluminum interconnects can be expected. However, it has been reported that the SiO_2 layer (PECVD) presents the large constant compressive stress (~ 200MPa) [163]. As consequences, the maximum initial diaphragm (diameter ~ 200μm) deflection can be as high as 6.1μm with 1.4μm SiO_2 thick pressure sensor (BOX layer ~ 1μm and PECVD SiO_2 ~ 0.4μm) [164]. It is thus necessary to compensate such residual stress by using other dielectric material. Si_3N_4 layer can be used for such purpose, since the Si_3N_4 with low tensile stress (100 ~ 150MPa) can be achieved with a proper deposition recipe. In most fabrication process, the thickness of SiO_2 layer (PECVD) is fixed (~ 400nm) due to standardized deposition recipe and simplicity of stress optimization process (only need to fine-tune the thickness of one passivation layer -- Si_3N_4). Besides the stress issue, we will discuss the selection for the thickness of Si_3N_4 layer with respect to various applications.

2.3.1 Cantilever Shaped Air Flow Sensor

The resonant frequency is one of the major concerns for piezoresistive based cantilever air flow sensor design [165]. The fundamental resonant frequency is usually required above 10 kHz to avoid environmental excitation. Theoretically, the resonant frequency (*f*) of cantilever is defined as**:**

$$f = \frac{1}{2\pi}\sqrt{\frac{k}{m}}$$

(2.1)

Where k is spring constant and m is the mass the cantilever. In semiconductor world

mass is difficult to be manipulated, especially when device shrinks down to micrometer scale. However, the optimization of spring constant is much applicable.

$$k = \frac{Ew}{4} \frac{t^3}{l^2}$$ (2.2)

Where, w, t and l are the width, thickness and length of the cantilever. E is the young's modulus. Based on the equation above, the spring constant can be improved by either varying the cantilever geometry or changing the material with higher young's modulus. It's been previously mentioned that two different materials (SiO_2 and SiN_x) are selected as the passivation materials. With the help of the FEM modeling (Abaqus 6.10), three different cantilever size variations are explored. FEM results with different combinations of passivation thickness are listed in Table 2.1.

As observed in Table 2.1, the resonant frequency is proportional to the cantilever thickness and inverse proportional to their effective sensing area as predicted from (10). Compared to SiO_2, the passivation layer of Si_3N_4 provides almost 30% improvement of resonant frequency with fixed geometry factor. This is contributed by the higher Young's modulus (around 170 GPa) of the nitride layer [166]. Although SiO_2 results in low spring constant, on the other hand, the pure SiO_2 fabricated cantilever shares the merit of higher sensitivity due to its relatively low Young's Modulus around 60 GPa [164]. However, such cantilever suffers high initial deflection issues due the large compressive stress [167] and might even result in cantilever broken during the process. Thus, the trade-off was made to compromise between device sensitivities and initial deflection issues. The discussion of the nitride layer for the purpose of the stress compensation will be provided in the next chapter as the preliminary consideration during pressure sensor design. Here, based on the FEM results, the optimum choice of cantilever shaped flow sensor design is 2.5um thick Si_3N_4 on top of the 1st passivation layer (400nm PECVD SiO_2).

Table 2. 1 Comparison resonant frequency for different combination of materials and different cantilever sizes.

Combinations of passivation	Resonant frequency (kHz)			Cantilever size (μm^2)
	First	Second	Third	
0.5 μm SiO_2	308	1930	2993	10 × 50
2.5μm SiO_2	923	2994	5697	10 × 50
2.5μm Si_3N_4	1205	4261	7450	10 × 50
0.5 μm SiO_2	95	596	896	20 × 90
2.5μm SiO_2	285	1781	1864	20 × 90
2.5μm Si_3N_4	373	2328	2611	20 × 90
1 μm SiO_2	67	371	420	40 × 100
2.5μm SiO_2	232	1254	1447	40 × 100
2.5μm Si_3N_4	304	1592	1895	40 × 100

2.3.2 Pressure Sensors

For the concern of a pressure sensor design, the minimum initial deflection of the diaphragm is required to reduce the non-linear component contributed by the geometry factor. In order to avoid the large mechanical non-linearity, the initial diaphragm deflection should be kept lower than 30% of the total diaphragm thickness. Hence, a thicker diaphragm is always beneficial to a linear piezoresistive response. However, the increase of diaphragm thickness will drastically reduce the pressure sensing capability (The detailed contributing factors for the total non-linearity and the diaphragm structure design of pressure sensor will be address in chapter 4). Therefore, the optimized thickness should be investigated for the concern of a better trade-off.

To investigate the surface profile of the Si_3N_4 layer with different thickness on oxide layer, the pressure sensors (in reticle level) with Si_3N_4 thickness of 2.5μm (the thickness is suggested based on FEM result in Table 2.1) is used. The reverse diaphragm thin down process is conducted by globally etching away 2.5μm nitride

layer through RIE (etchant: CHF_3) based on time control. Meanwhile, a white light interferometer (VEECO NT3300) system is used to record the surface profile as the proof of etching result.
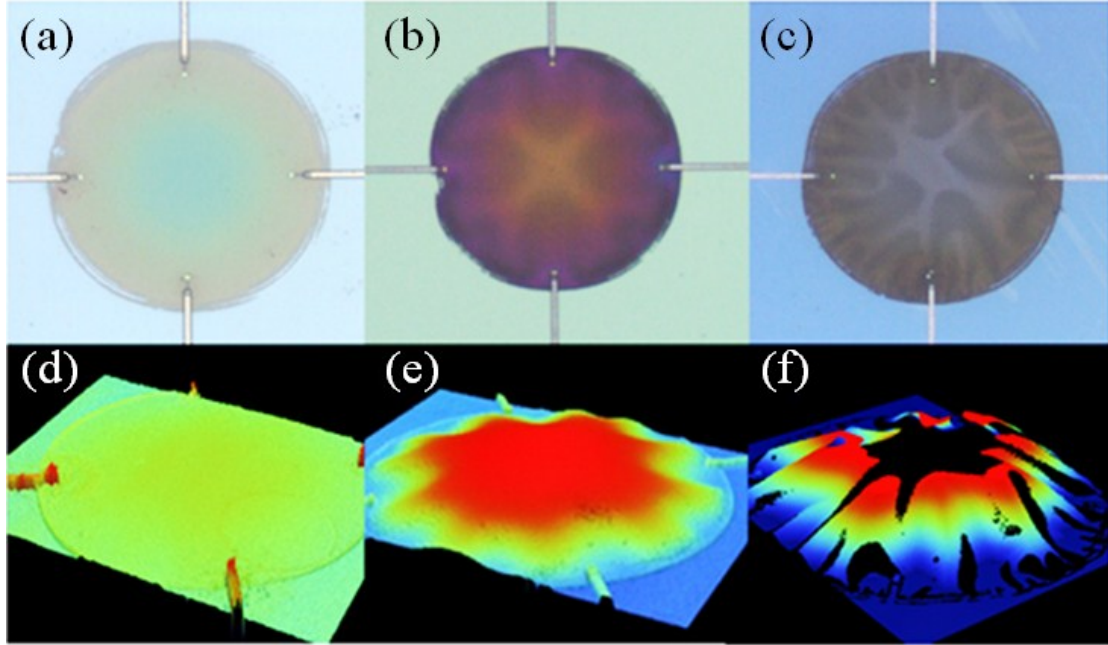
Figure 2. 12 Changes of the diaphragm surface profile for (a) & (d) after 30mins RIE etching, (b) & (e) after 45mins RIE etching, and (c) & (f) after 60 min RIE etching. The upper three graphs show the optical images and the bottom three graphs indicated the 3D surface profiles captured by white light interferometer (VEECO NT3300).

After first 30 minutes of RIE etching, the results of both optical and 3D surface profile are shown in Figure 2.12 (a) and (d). The diaphragm surface remains flat. With another 15 minutes etching, the Si_3N_4 layer is fully removed and the corresponding results are shown in Figure 2.12 (b) and (e). It is worth noting that the edge of diaphragm is in a star shape after the Si_3N_4 is just stripped. This indicates the stress distribution inside the SiO_2 layer along the membrane edge. The star shape shows on set stage in between the flat multi-layered diaphragm and the wrinkled diaphragm. After the Si_3N_4 layer is stripped, the membranes swelling in both upward and downward directions are observed as well. Finally, an extra 15 minutes etching is added in order to observe the surface profile of the further thinned down diaphragm

(extra etching on 400nm PECVD SiO$_2$). In Figure 2.12 (f), the surface profiler picture cannot be fully reviewed because of the large deflection exceeding the equipment limitation, but the wrinkling status can be clearly observed as shown in the optical image in Figure 2.12 (c). These three pairs of diaphragm pictures show clear transformation from a regular diaphragm of good flatness into a wrinkled diaphragm of irregular deformation with respect to RIE etching time increment.

To quantitatively explore the relationship between the diaphragm deflection and the Si$_3$N$_4$ thickness, the plot of diaphragm initial deflection as a function of the nitride layer thickness is provided in Figure 2.13. The inset provides the captured surface profile using the interferometer. As indicated in the figure, the vertical deflection at the diaphragm center increases from 0.05 μm to 4.90 μm with respect to thickness of nitride layer decreasing from 2.5 μm to 0 μm. By fitting the scattered data, we can clearly observe that the diaphragm central deflection change is relatively small within the variation of Si$_3$N$_4$ thickness ranging from 2.5μm to 0.7μm. However, the deflection abruptly increases after the thickness of Si$_3$N$_4$ reduced to 0.7μm. This clear non-linear relationship indicates that the nitride layer is able to modulate the diaphragm profile in an effective manner before the thickness of nitride reaches 0.7μm; whereas in the case of deposition of more than 0.5μm Si$_3$N$_4$, the improvement becomes less effective. Please also be noticed that the above optimization process is conducted with the flat diaphragm structure with diameter of 200μm. If any of these parameters vary, the required thickness of nitride layer may subject to the individual case of each design. In addition, a further etching process on dioxide layer (after complete removal of nitride) leads to the wrinkled diaphragm with maximum deflection up to 8.3 μm.
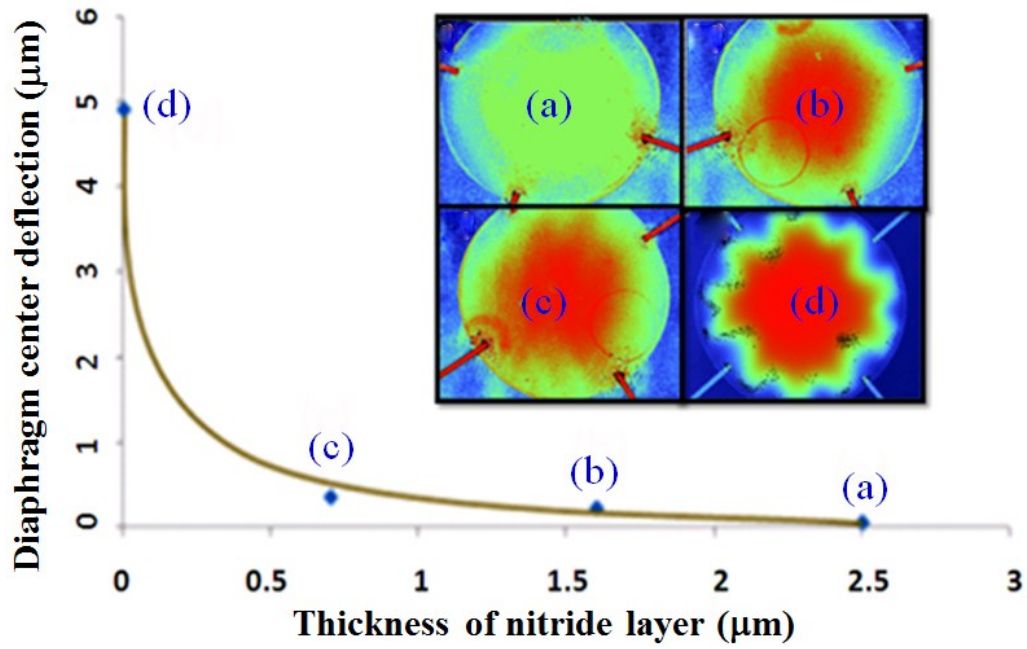
Figure 2. 13 Diaphragm center deflection as a function of nitride layer thickness for case: (a) 2.5μm, (b) 1.6μm, (c) 0.7μm and (d) 0μm. Inset shows the captured surface profile under each case. The flat diaphragm pressure sensor (diameter ~ 200μm) is used for this experiment.

2.4 Release of the device

We have discussed the fabrication of the SiNWs and the choice of passivation layers in previous sections. In the section, we will focus the final stage of the device fabrication—release of the device. Based on the device applications, various releasing method will be introduced as the following.

2.4.1 Backside DRIE

Backside deep-reactive ion etching (DRIE) is commonly used for the MEMS device releasing process. An example of general process flows for the release of the pressure sensing diaphragm is shown in the Figure 2.14.
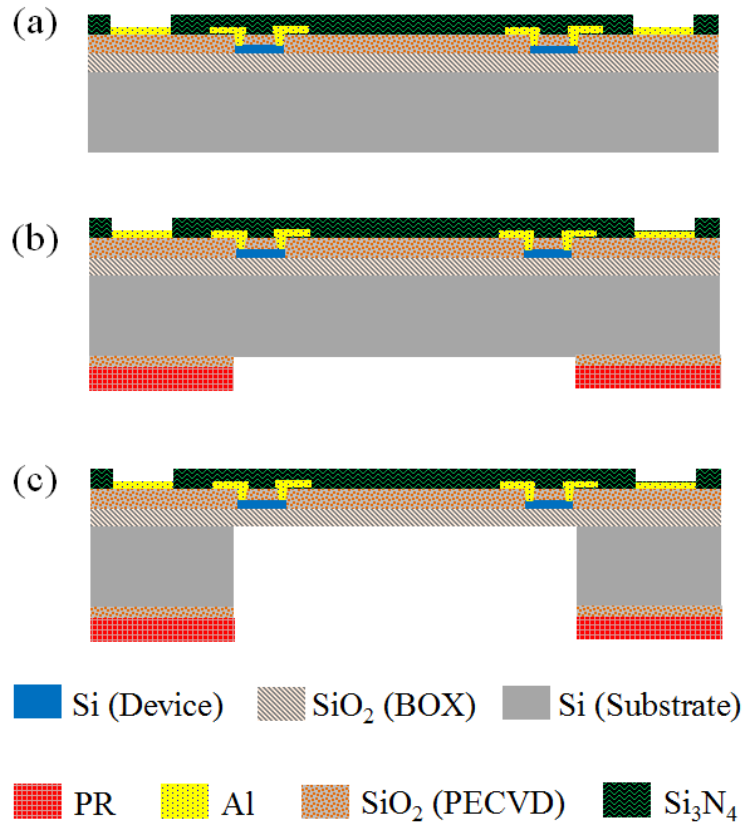
Figure 2. 14 Process flows of using backside DRIE for the release of pressure sensing diaphragm.

After finishing the fabrication of the device sensing element (e.g. SiNWs as indicated in Figure 2.14 (a)), the function of a pressure induced diaphragm deformation can only be realized after releasing the diaphragm from rigid silicon substrate. Following the backside to frontside alignment, the hard masks (usually, both SiO_2 (1μm) and PR (2μm) are applied as shown in Figure 2.14 (b)) are patterned using backside RIE. With the support of another dummy wafer attached on the frontside, the backside DRIE process is then completed by using high power etching tool as shown in Figure 2.14 (c).

In most cases, a good etching stop layer (a high etching selectivity, e.g. SiO_2) is necessary to setup the clear etching boundary condition. However, it is also challenging to make a proper judgment based on the observation. Figure 2.15 exhibits an optical image after etching away the substrate silicon and reaching the BOX layer.

However, it is even difficult to standardize the DRIE process over entire 8 inch wafer. Thus, the etching uniformity between each device may vary up to 10-12%. Figure 2.16 illustrates the optical images of an over-etched diaphragm (Figure 2.16 (b)) in contrast to the precisely released diaphragm (Figure 2.16 (a)). Such over-etching seems to be inevitable in most fabrications and it will cause the performance variation even in the same batch design. We will discuss the possible method to minimize this variation in chapter 4.2.2.
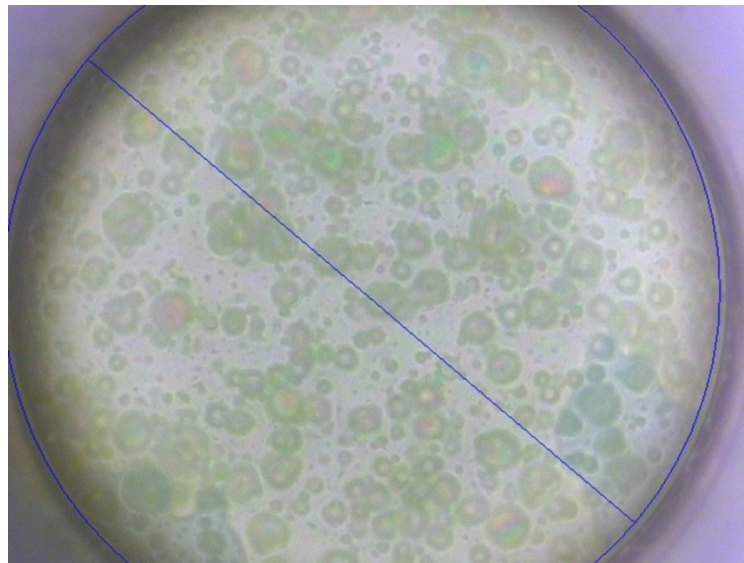
Figure 2. 15 Optical image of the etching stop layer (SiO_2) for the observation of a proper etching time.
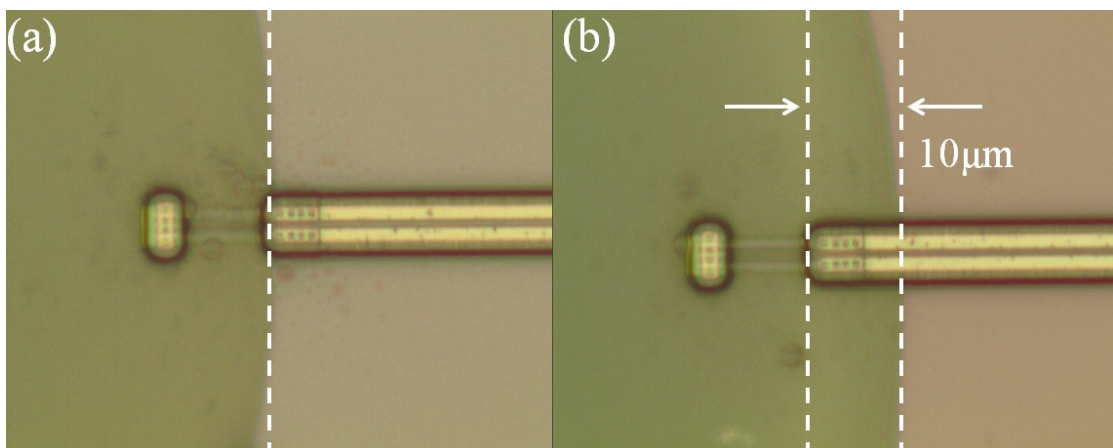
Figure 2. 16 Optical images of (a) the edge of a precisely released diaphragm and (b) the edge of an over-released diaphragm.

2.4.2 Frontside Isotropic Etching
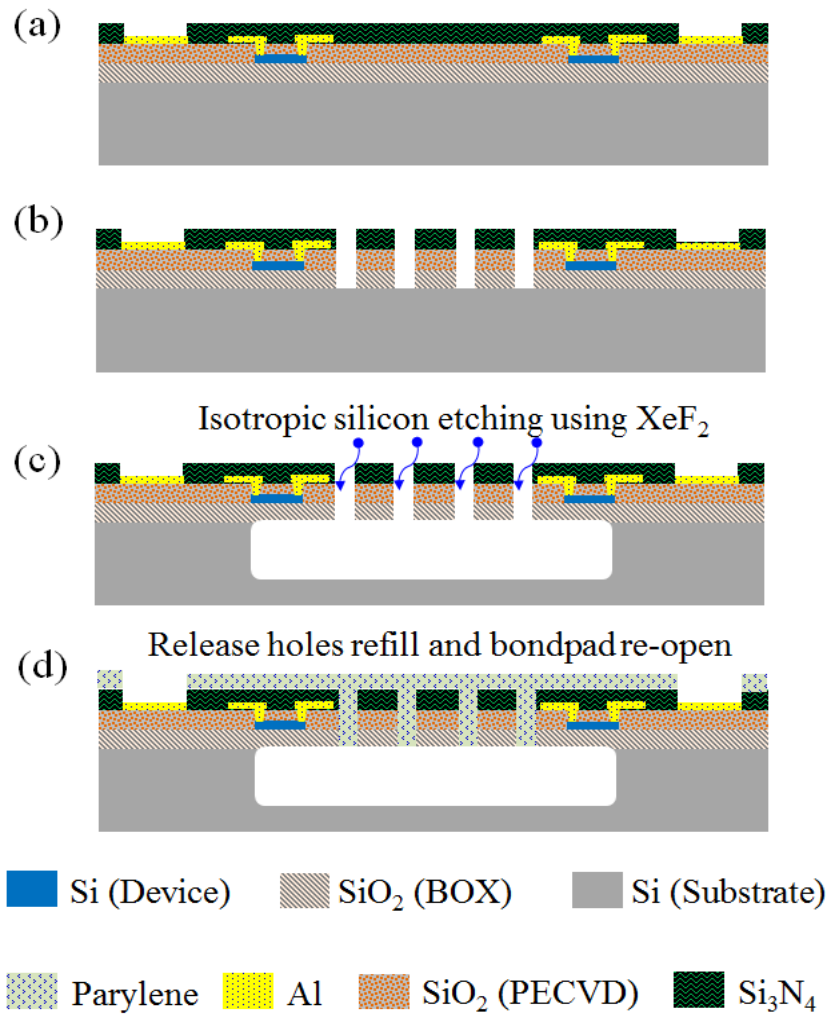
Figure 2. 17 Process flows of using frontside isotropic etching for the release of pressure sensing diaphragm.

Another common practice for the diaphragm release is to use the isotropic etching process from the frontside. This surface-micromachining approach takes advantage of a more precise alignment between each layer. After fabrication of the release hole on the frontside of the diaphragm (Figure 2.17 (b)), Xeon difluoride (XeF_2) is usually applied as the etchant (Figure 2.17 (c)) due to its high isotropy and good etching selectivity between silicon and other passivation dielectrics (e.g. SiO_2 and Si_3N_4). In order to encapsulate the release hole and apply the pressure difference, another layer of passivation (e.g. sputtering of polysilicon or evaporation of parylene-C) is coated

as depicted in Figure 2.17 (d). In sequence, the bonding pads have to be re-opened after process with a cost of one extra mask.
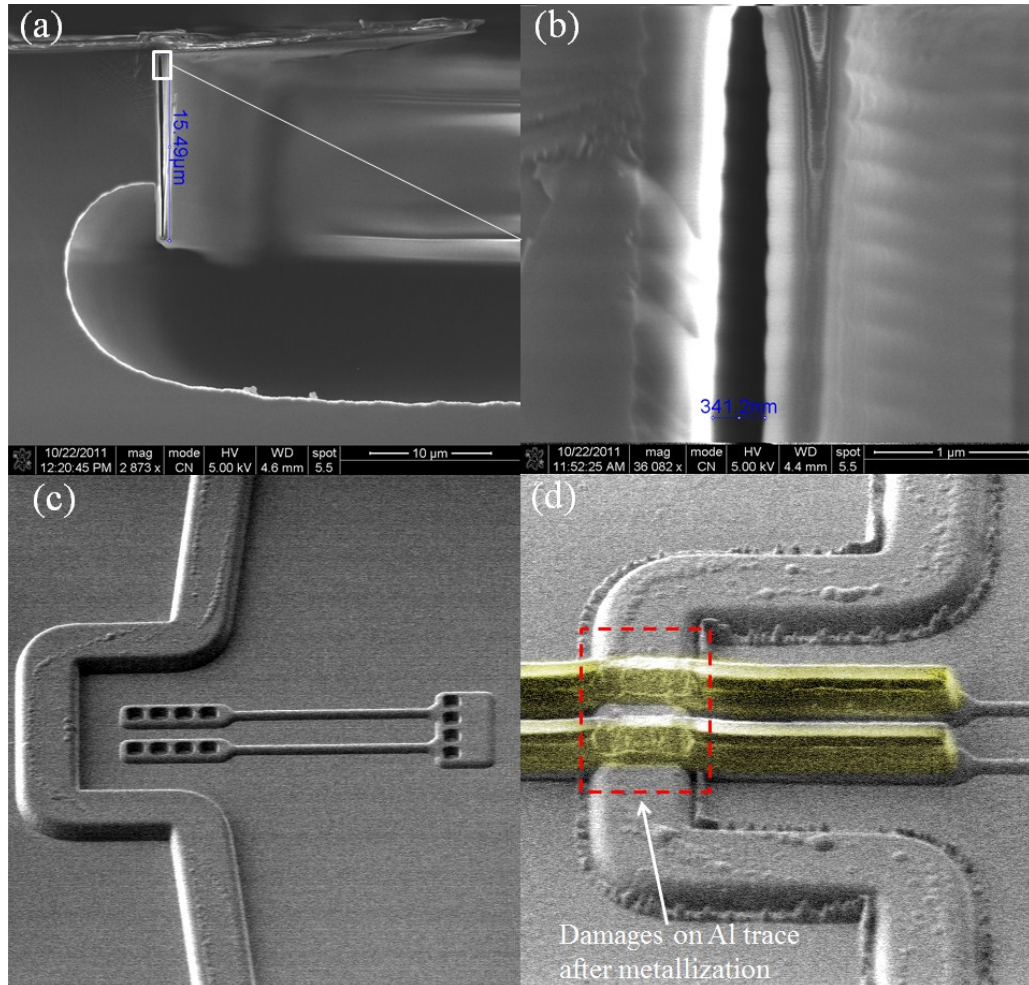
Figure 2. 18 SEM photos of (a) the trench structure after XeF_2 etching (over-etched), (b) the zoom-in view of the trench, (c) the surface hump after the trench refill and (d) the Al interconnection after metallization (Al trace is highlighted in yellow).

Additionally, the extra trench protection will be necessary to avoid the unwanted over-etching, since this etching process is targeted in all direction. Figure 2.18 demonstrates SEM images of the trench structure (made by SiO_2) after an isotropic attack by XeF_2. Figure 2.18 (a) indicates a successful trench stop against XeF_2, however, over-etching process will result in a under-cut beneath the trench. Due to the process imperfection, the keyhole will always be introduced during the trench refilling process (Figure 2.18 (b)), but a reasonable extent of keyhole does not affect the

functionality of the trench. However, in order to completely cover the keyhole, a hump structure on wafer surface (Figure 2.18 (c)) will be created after the trench refill. Such non-flat surface topography lays another challenge for the following metallization process. With the non-uniform coating of PR, the PR pattern cannot be preserved as its expected shape over the hump. Hence, over-etching of the Al trace in the hump region due to less hard-mask protection as indicated in Figure 2.18 (d). Unfortunately, such over-etching seems to be inevitable. Thus, besides a careful time-controlled etching process, it is important to make sure a wider PR coverage in the mask layout with resultant less PR losses after development. In addition, the space between each metal trace should be kept away by certain distance (wider than the minimum width of Al trace) to avoid the etching residual and electrical short.

2.4.3 Backside Grinding Process
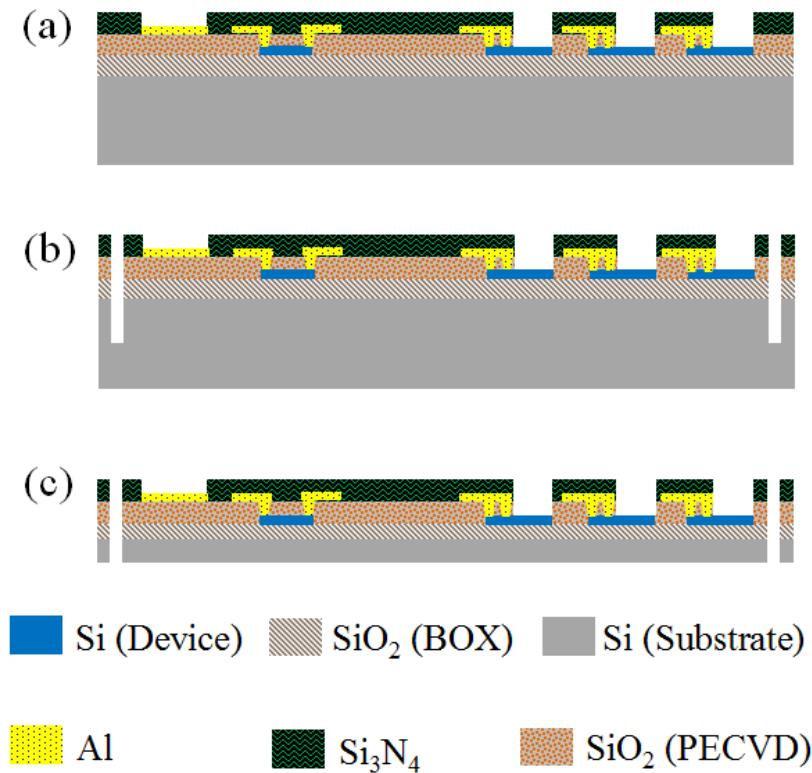
Figure 2. 19 Process flows of using backside grinding to release silicon probe from the wafer.

In case of silicon probe design, thinner probe may be too fragile to be handled during the transferring and wire-bonding, while the thicker probe will be too bulky and cause larger tissue damages. It has been recommended to have the probe thickness less 100μm [131, 153], thus, we target the released probe with a thickness of 50μm. In comparison with previously introduced release processes, there is no etching stop to be set, if the backside DRIE is chosen for the probe release. The resultant probe thickness would be significantly varied from batch to batch. Therefore, the DRIE is performed from the wafer frontside as shown in Figure 2.19 (b). The final trench thickness is in the range from 60μm to 70μm. Sequentially, a backside grinding process is then conducted from the backside of wafer. With a pure mechanical grinding process, both etching remaining wafer thickness and uniformity over 8 inch wafer can be guaranteed. After the remaining thickness less than the depth of the frontside trench, the device is automatically released from the wafer. Figure 2.20 (a) shows the trench structure after a frontside DRIE and (b) provides the SEM photo of a released silicon probe.
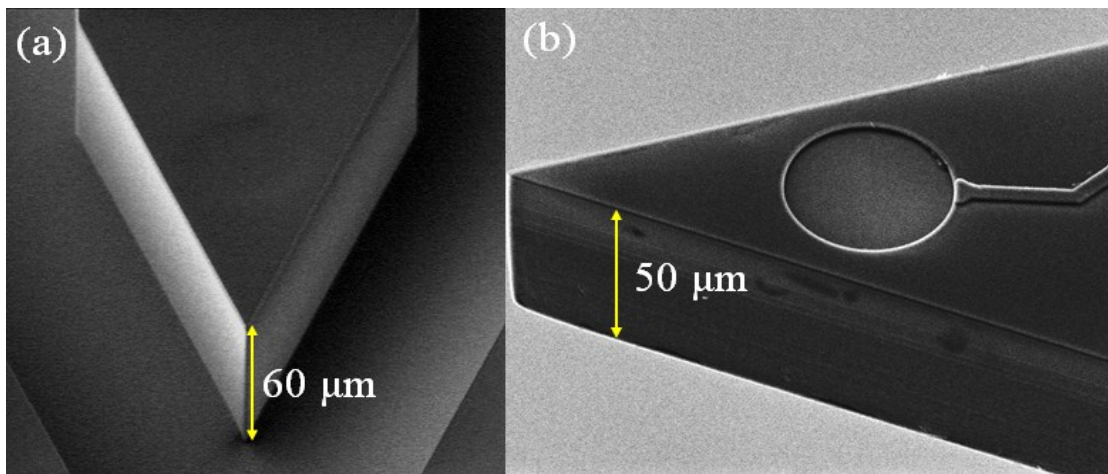
Figure 2. 20 SEM pictures of (a) the tip of a silicon probe after the frontside DRIE (the probe shape is defined), (b) the tip of a released silicon probe after backside grinding.

Chapter 3 Cantilever Shaped NEMS Piezoresistive Air Flow Sensor

The background of the current piezoresistive flow sensor and the motivation for the design of silicon nanowires (SiNWs) based counterpart have been briefly introduced in chapter 1.2.1. In additional to the superior piezoresistance effect compared to the traditional metal stain gauge and polysilicon material, the reduced cross-section of SiNWs provides higher initial piezoresistance in contrast to bulk silicon wires, therefore a lower power consumption at the given supply voltage. Furthermore, the scalability of the device will be significantly improved and such improvement has been demonstrated in many modern MEMS sensor designs [168-169].

In this chapter, we will discuss detailed design consideration and characterization of the SiNWs based cantilever shaped air flow sensor (see Figure 3.1 for the device schematic). It also has been demonstrated in chapter 2 that the device is fabricated on the (100) SOI wafer with the CMOS-compatible process. SiNWs in three different lengths (2μm, 5μm and 10μm) with the same average cross section of 90nm × 90nm are used as the piezoresistive sensing element. By leveraging the piezoresistive effect of SiNWs, significant improvements of flow sensing performance in terms of sensitivity, linearity and hysteresis are reported. In addition, the ultra-low input power (less than 1 μW) can be achieved due to the high piezoresistance (> 150KΩ) and a low supply voltage (0.1V) used in the experiment. Additionally, the design optimization is also carried out among three different effective sensing areas (10 × 50 μm^2, 20 × 90 μm^2, 40 × 100 μm^2) and various lengths of SiNWs.
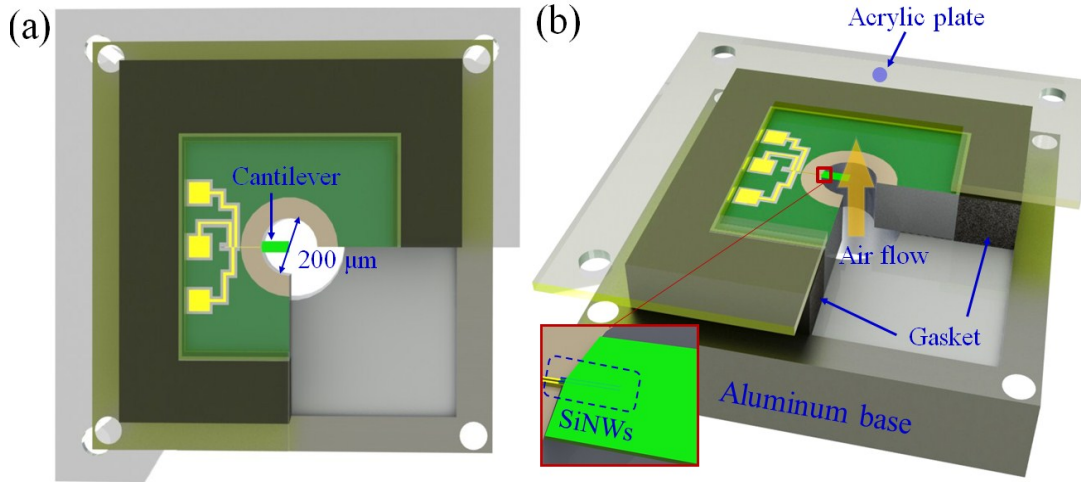
Figure 3. 1 The schematics of cantilever shaped air flow sensor for (a) top view and (b) 45° angle view.

3.1 Design Considerations

For most reported cantilever shaped piezoresistive flow sensors, the flow induced mechanical force is loaded on the cantilever structure and results in piezoresistance changes. Such mechanical force is highly dependent on the flow direction, velocity, channel dimension and the nature of the fluid. Based on the flow viscosity and velocity, the status of the flow can be defined in laminar or turbulence or transition regime, which is characterized by Reynolds number (R_e) as shown below:

$$R_e = \frac{\varsigma VL}{u} = \frac{VL}{v} \tag{3.1}$$

Where ς is the density of fluid, L is the characteristic linear dimension (or diameter (d) in the case of the bounded pipe), V is mean velocity of the object relative to the fluid, u is the dynamic viscosity of the fluid and v is the Kinematic viscosity defined as u/ς. However, regardless of the laminar and turbulent flow, dependent on the channel dimension, flows can also be categorized by their boundary, i.e., internal or bounded by walls and external or unbounded [170]. As indicated in Figure 3.1 (a), in our SiNWs based cantilever air flow senor design, the air flow is confined within a

tunnel of 400 μm long with diameter of 200 μm. Figure 3.1 (b) shows the overall view of the device and indicates the flow direction by yellowish arrow bar. In our design the internal situation is applied instead of the external situation, but similar to the external situation, the velocity and boundary layer profile need to be considered first.
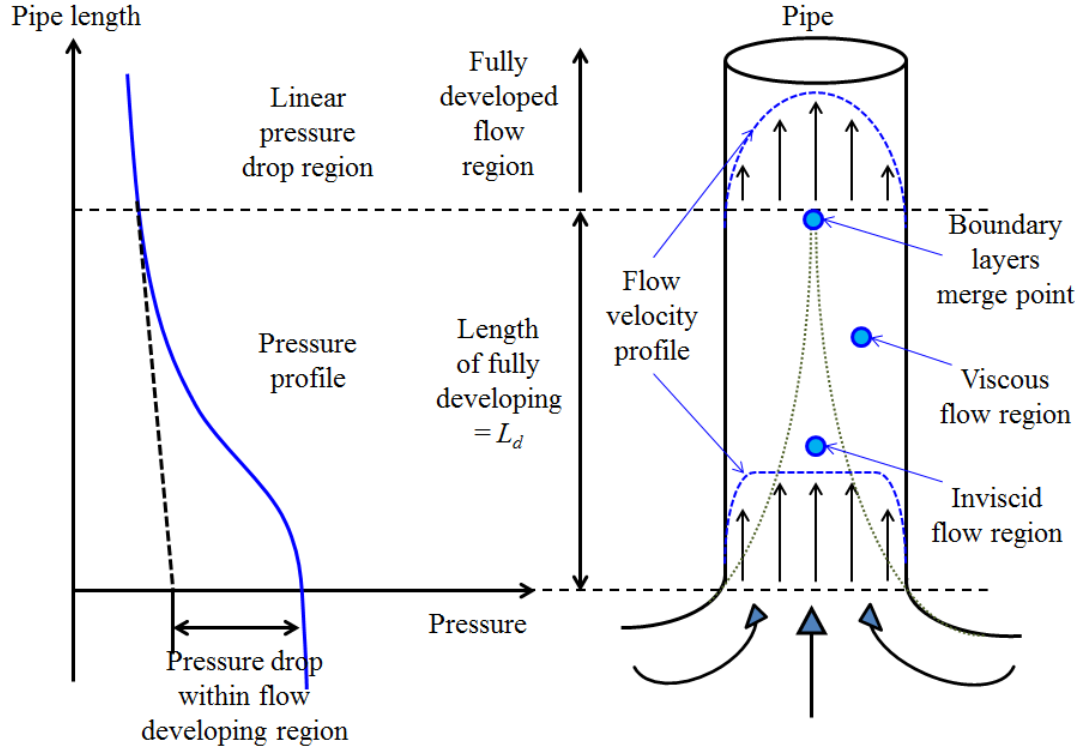
Figure 3. 2 The illustration of flow development for internal situation.

Figure 3.2 explains the both flow velocity and pressure profile for a long pipe flow [170]. At the entrance region of the pipe, where the fluid (e.g air) flows from relatively open space into a more confined tube, the viscous boundary layers grow downstream, retarding in the vertical direction at the pipe wall and thereby accelerating the center-core flow to maintain the incompressible continuity requirement:

$$Q = \int u dA = Constant \qquad (3.2)$$

Where Q is the total flow rate, u is the local flow velocity and A is pipe

cross-section area. At a given distance (L_d) from the entering point, the boundary layers merge each other and the inviscid core disappears. Thus, the flow is said to be fully developed and the velocity is fixed. Dimensional analysis shows that the Reynolds number is the only parameter affecting flow development length. If

$$L_d = f(d, V, \varsigma, u) \quad \& \quad V = \frac{Q}{A}$$

then
$$\frac{L_d}{d} = g(\varsigma V d / u) = g(R_e) \tag{3.3}$$

For laminar flow, the accepted correlation is

$$\frac{L_d}{d} \approx 0.06 R_e \tag{3.4}$$

In turbulent flow, the boundary layer grows faster and L_d is relatively shorted as,

$$\frac{L_d}{d} \approx 4.4 R_{ed}^{1/6} \tag{3.5}$$

With the maximum flow velocity of 65 m/s in our case, according to (1) the Reynolds number is approximately 870, which is definitely in laminar flow regime ($R_e < 2300$). After applying (3.4), the L_d/d is calculated to be 52. Therefore, the distance required for a fully developed flow is around 10400μm, which is much longer than the physical channel length (flow tunnel ~ 400μm) in our actual design. Since the actual distance is significant shorter than the distance required for air flow to be fully developed, an assumption is proposed that the air is uniformly flowing through channel from the entering point to the cantilever surface. Thus, the pressure drop along the channel is negligible. Based on this assumption, instead of the drag force caused by viscous fluids, the uniform pressure is loaded on the cantilever beam. According to reference [171], the equation of cantilever tip deflection (δ_{max}) is defined

as:

$$\delta_{max} = \frac{\omega l^4}{8EI} \tag{3.6}$$

Where ω is the uniformly distributed load, l is the length of the cantilever, E is the Young's modulus and I is the moment of inertia,

$$I = \frac{wt^3}{12} \tag{3.7}$$

Here, w is the width of the cantilever beam and t is the thickness of the cantilever. To verify the assumption of uniform pressure loaded on the cantilever, the validation test will be discussed in the next section.

3.2 Device Characterizations
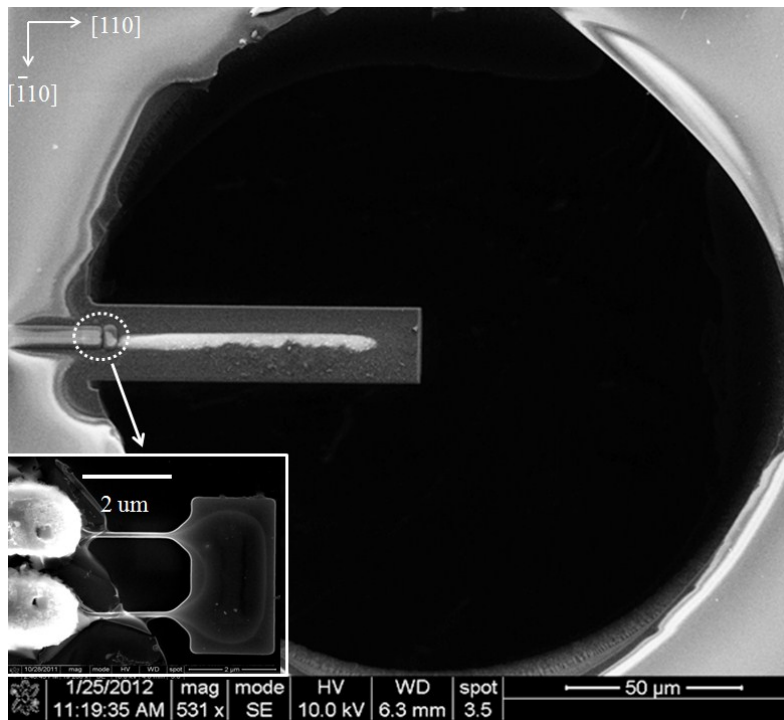
Figure 3. 3 The SEM image of SiNWs based cantilever flow sensor (cantilever size is 20 μm × 90 μm with SiNW length of 2 μm). Inset shows the 2 μm SiNWs after etching back top passivation layers.

The general fabrication steps have been mentioned in previous. After the backside

DRIE to create the flow tunnel, the cantilever shape is finally defined through the frontside dielectric layer etching using focus ion beam (FIB). An SEM example of a cantilever with 2μm SiNWs embedded at the conjunction is given in Figure 3.3. We will discuss the testing procedure and results in the following content.

3.2.1 Testing setup

The test is conducted at room temperature (25°C) with the supply voltage as low as 0.1 V to prove the proper device functionality under an ultra-low power. As depicted in Figure 3.4, the compressed air is directed through the flow meter, which controls the flow rate changes. Before air reaching the aluminum base for a hermetic seal, a pressure regulator (ALICAT PCD series) is placed in between to measure the air pressure feedback from the air channel. Based on the assumption made in section 3.1, this read back pressure is supposed to be the same amount as the uniform load applied on the cantilever beam. The semiconductor characterization system (Keithley 4200-SCS) is used to measure the piezoresistance variation with respect to the change in flow velocity. To avoid incorrect feedback readings caused by the air leakage, the hermetic sealing jig is applied (shown in Figure 3.4). The device is slotted into an aluminum base. A gasket is used to encapsulate the device and the air is confined only within the flow channel. An acrylic plate is covered on top of the device with an opening window available for the air flow passing and signals probing. Screws at the each corner attach the acrylic plate to the aluminum base and tighten the sealing gasket surrounding the device body. Please refer to Figure 3.1 for the hermetic sealing design.
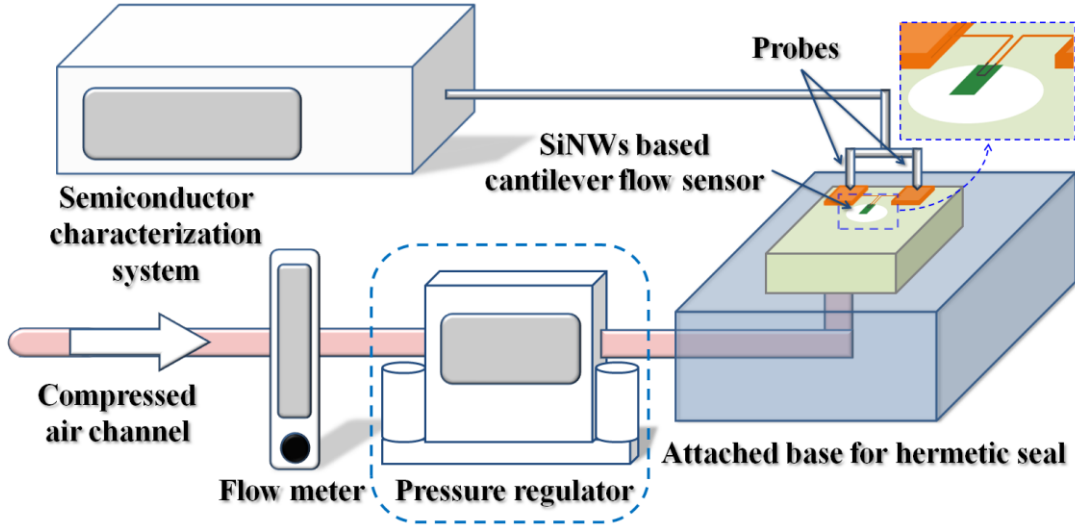
Figure 3. 4 Illustration of test setup for the cantilever air flow sensor.

3.2.2 Testing result and discussion

3.2.2.1 Effect of cantilever dimension variations on the SiNWs based flow sensor

As mentioned before, devices with three different sizes (10×50 μm^2, 20×90 μm^2 and 40×100 μm^2) are fabricated. Their SEM pictures are given in Figure 3.5. In this section, the length of SiNWs embedded in all cantilevers is fixed to 5 μm (shown in the inset of Figure 3.5).
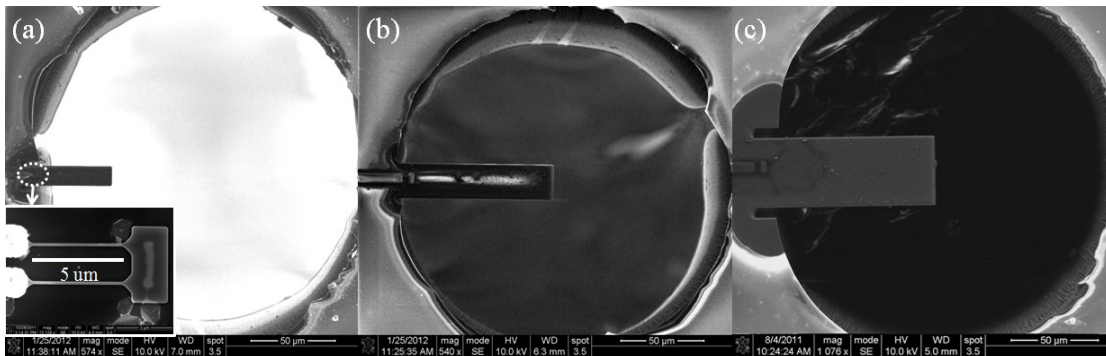
Figure 3. 5 SEM photos of air flow sensor with 3 different cantilever sizes: 10×50 μm^2, (b) 20×90 μm^2 and (c) 40×100 μm^2. The length of SiNWs is fixed to 5 μm in all cantilevers
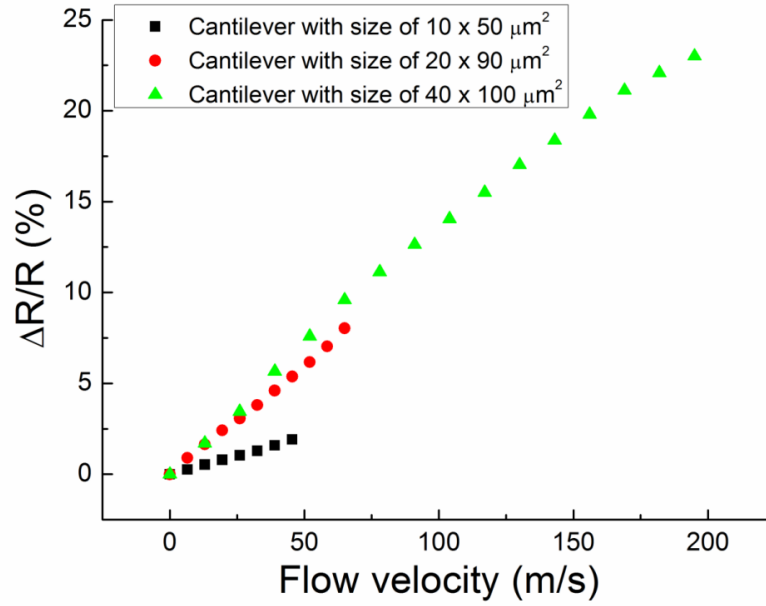
Figure 3. 6 Plots of the piezoresistance percentage changes with respect to the flow velocity increment for cantilevers with the area of 10×50 µm² (black curve), 20×90 µm² (red curve) and 40×100 µm² (green curve). The length of the SiNWs is fixed to 5 µm for all cantilevers

The similar testing regarding to the effect of geometry variations had been demonstrated before and the device sensitivity was reported proportional to their effective sensing area (cantilever size) [89]. However, in our case, the sensitivity is not simply proportional to their area. As shown in Figure 3.6, the percentage of the piezoresistance changes is plotted. The percentage changes are calculated by firstly averaging the resistance values recorded from at least three identical designs. Such average value is normalized by the original piezoresistance measured at the initial state ($V= 0$ m/s) in the second step. The overall percentage changes of piezoresistance are 1.92%, 8.05% and 23% for the cantilevers with the area of 10×50 µm², 20×90 µm² and 40×100 µm² respectively. Please be noticed that these resistance changes are corresponding to the different sensing range due to the safety working limit of the device. As indicated in Figure 3.6, the safety working range for cantilever of 10×50 µm² is only up to 45 m/s. The safety working range for cantilevers with area of 20×90 µm² and 40×100 µm² are 65 m/s and 195 m/s receptively. In each cantilever size,

the proper device working range is verified through the fatigue test, which is conducted for three cantilevers with identical size under the gradually increased air flow. As a result, the working range is guaranteed without the cantilever broken for at least three trials. To provide the fair comparison among three designs, the percentage changes of average piezoresistance over flow velocity are calculated. The highest average change is 0.124%/m/s recorded for the cantilever with the area of 20 × 90 μm^2 and the lowest change of 0.043%/m/s recorded for cantilever with size of 10 × 50 μm^2. For the cantilever with the largest size of 40 × 100 μm^2, the average percentage change is 0.116%/m/s. With the tensile stress up to 110 MPa (equivalent to the flow velocity of 65 m/s) extracted from the simulation, the plots of resistance changes in Figure 3.6 are in a good agreement with previously reported data [16]. For cantilever with the size of 40 × 100 μm^2, the stress extracted is up to 340 MPa (equivalent to the flow velocity of 195 m/s) and it is difficult to correlate such large stress to any reported test data. However, the similar trend of resistance percentage changes (ΔR/R %) has just been reported by J. Wei *et al.* [172]. In their report, the slope of percentage changes (ΔR/R %) drops after reaching 15% and that is almost identical to our findings under the larger tensile stress (as the green curve shown in Figure 3.6). The slight difference is that the slope drops after ΔR/R reaches 10% in our case. This early drop of resistance changes could be the combination of the piezoresistive effect under large tensile stress together with the effect of the flow status changes (from laminar to transition regime) due to the increment of flow velocity. Recall equations of flow developing length (L_d) in section 3.1. In turbulent regime, the developing length is much shorter than that of laminar flow. Thus, the actual L_d may become shorter even in transition regime, which results in the deviation from the assumption for the uniform load on cantilever. In conclusion, the cantilever with the dimension of

20×90 μm^2 provides a better linearity and higher average resistance percentage changes.

3.2.2.2 Effect of SiNWs length variations on the cantilever flow sensor
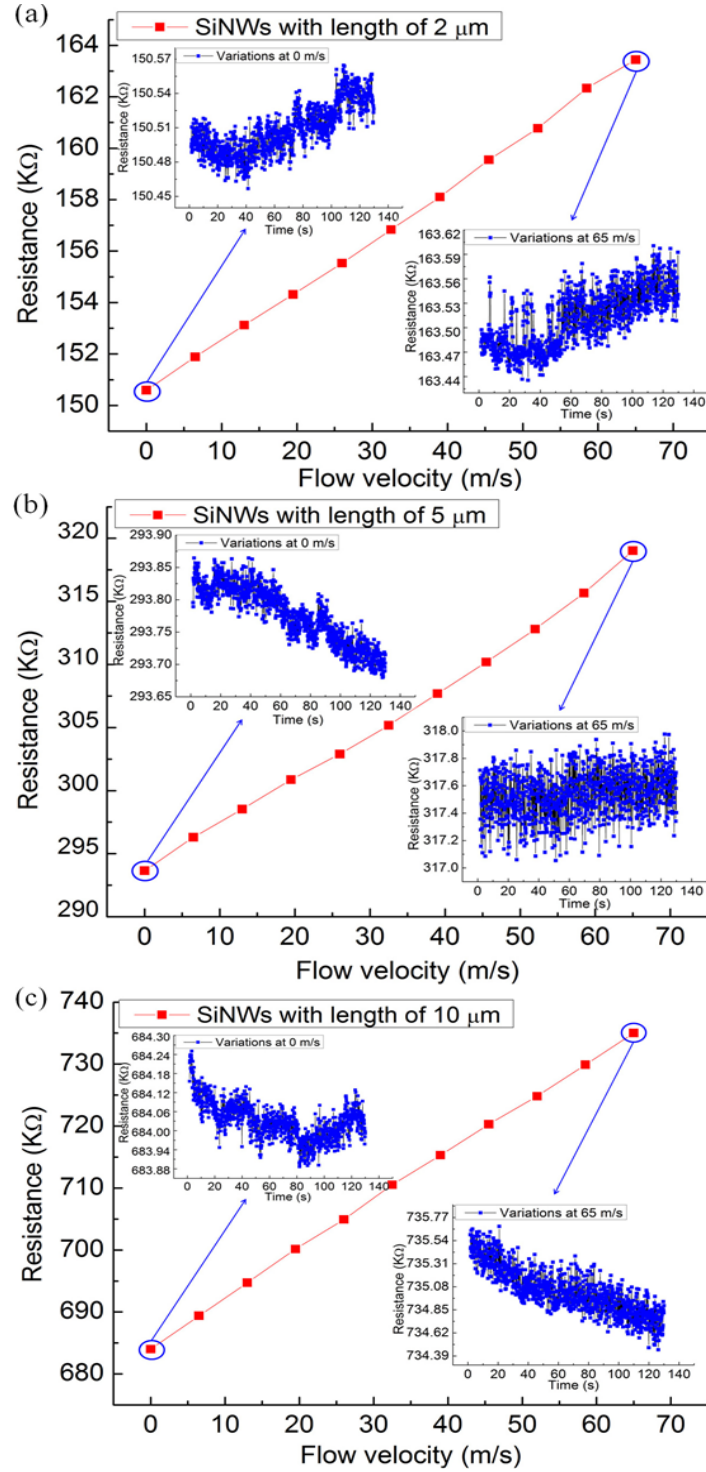
Figure 3. 7 The resistance changes with respect to the flow velocity variations for cantilever flow sensor with the SiNWs length of (a) 2µm, (b) 5µm and (c) 10µm.

After finalized the geometry factor of the cantilever (20×90 μm^2), the characterization for length of SiNWs is conducted with three different variations: 2 μm, 5 μm and 10 μm. Fig. 3.7 plots the piezoresistance changes with respect to the flow velocity (V) increment for designs with different length of SiNWs. The insets in each plot indicate the piezoresistance variations at initial state ($V = 0$ m/s) and finial state ($V = 65$ m/s).

Table 3. 1 Summarized information from Figure 3.7.

Length of SiNWs (μm)	Normalized Sensitivity (Ω/m/s)	Piezoresistance variations (Ω)		Cantilever area (μm^2)
		Initial state	Final state	
2	198	100	170	20×90
5	386	170	800	20×90
10	785	360	1250	20×90

As summarized in Table 3.1, the highest average sensitivity is obtained for 10 μm SiNWs design, which is almost 4 times higher than that of 2 μm SiNWs design, but it is still around 500 Ω lower than the resistance fluctuation at the final state. An even severe resistance fluctuation happens in 5μm SiNWs design and thereby both designs fail to detect the unit flow velocity change (1 m/s) due to an increased flow induced fluctuation. However, the average piezoresistance changes (198 Ω/m/s) is almost 30 Ω higher than its resistance fluctuation at the final state for the 2 um SiNWs design. Therefore, the air flow sensing resolution down to 1 m/s can be realized. In addition, the device non-linearity [173] is calculated to be around 0.1%, which is improved by an order of magnitude compared with recently reported piezoresistive cantilever flow sensor designs [92-93]. To make a fair comparison with recently reported flow sensor design, Table 3.2 summarizes the sensitivity and linearity of SiNWs based cantilever flow sensors together with other recently reported

piezoresistive cantilever flow sensors. As indicated in the second last column of Table 3.2, compared with reported designs using other piezoresistive sensing elements, the SiNWs based cantilever flow sensor does significantly improve the device sensitivity. To eliminating the geometry effect for further fair comparisons, the effective sensing area of the device has also been normalized and listed in the last column of Table 3.2.

Table 3. 2 Summary of device sensitivity for recently reported designs together with our designs.

References	Piezoresistive element	Cantilever area (μm^2)	Linearity	Sensitivity	Normalized sensitivity [a]	Normalized sensitivity [b]
Ma et al. [167]	Pt resistor	400 × 4000	N.A	0.0533 $\Omega/m/s$	1.757×10^{-4} $\Delta\Omega/\Omega/m/s$	1.1×10^{-10} $\Delta\Omega/\Omega/m/s/\mu m^2$
Lee et al. [90]	Pt resistor	2000×2000 +400×2000	N.A	0.0785 $\Omega/m/s$	2.243×10^{-4} $\Delta\Omega/\Omega/m/s$	4.67×10^{-11} $\Delta\Omega/\Omega/m/s/\mu m^2$
Aiyar et al. [91]	Conductive elastomer	1500 × 400	N.A	66 $\Omega/m/s$	2.295×10^{-4} $\Delta\Omega/\Omega/m/s$	3.825×10^{-10} $\Delta\Omega/\Omega/m/s/\mu m^2$
Li et al. [93]	P-doped bulk silicon wire	400 ×1100	~ 1%	0.71 $mV/m/s$	4.733×10^{-5} $\Delta\Omega/\Omega/m/s$	1.08×10^{-10} $\Delta\Omega/\Omega/m/s/\mu m^2$
Song et al. [92]	Conductive elastomer	3500 × 600	~ 1%	14.5 $mV/m/s$	7.25×10^{-4} $\Delta\Omega/\Omega/m/s$	3.45×10^{-10} $\Delta\Omega/\Omega/m/s/\mu m^2$
2μm SiNW design	P-doped SiNWs	20 × 90	~ 0.2%	198 $\Omega/m/s$	1.32×10^{-3} $\Delta\Omega/\Omega/m/s$	7.33×10^{-7} $\Delta\Omega/\Omega/m/s/\mu m^2$
5μm SiNW design	P-doped SiNWs	20 × 90	~ 0.4%	386 $\Omega/m/s$	1.314×10^{-3} $\Delta\Omega/\Omega/m/s$	7.3×10^{-7} $\Delta\Omega/\Omega/m/s/\mu m^2$
10μm SiNW design	P-doped SiNWs	20 × 90	~ 0.3%	785 $\Omega/m/s$	1.148×10^{-3} $\Delta\Omega/\Omega/m/s$	6.376×10^{-7} $\Delta\Omega/\Omega/m/s/\mu m^2$

[a] First normalization by its original piezoresistance at initial state (V = 0 m/s).
[b] Based on first normalization, second normalization based on the different effective sensing area.

The average percentage changes of the resistance are extracted to further analyze the sensitivity variations based on the different SiNWs lengths. As shown in Figure 3.8, the cantilever with 2 μm long SiNWs shows high percentage change (8.6%). For the 5 μm and 10 μm SiNWs designs, the percentage changes are 8.05% and 7.45% respectively. Therefore, the trend of percentage changes is inversely proportional to the length of SiNWs and this can be explained by the gauge factor difference, which will be introduced in Section 3.2.2.3.
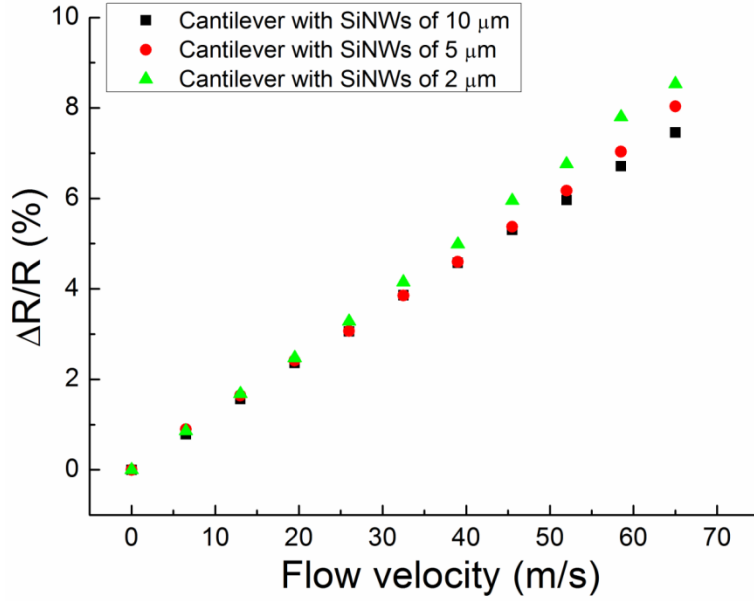
Figure 3. 8 Plots of percentage changes of the piezoresistance (normalization refers to the resistance at initial state) with respect to the flow velocity increment for cantilevers with SiNWs length of 10µm (black curve), 5µm (red curve) and 2µm (green curve).The dimension of cantilever is fixed to $20 \times 90\ \mu m^2$ for all designs.

Besides of the less remarkable piezoresistive effect, the reported cantilever based piezoresistive air flow sensors also suffer poor hysteresis [91, 167]. Thus, in order to verify the air flow sensing consistence of our device, the repeatability test is conducted. The flow meter (shown in Figure 3.4) is programmed with a given increasing step of 13 m/s and starting at the flow velocity of 0 m/s. The duration between each step is set to 5 seconds. After reaching the flow velocity of 65 m/s, the air flow is decreased back to its initial state with the same velocity changing step and duration to complete one cycle. There total 2 complete cycles are recorded over 130 seconds (limited by the maximum data storage capacity of semiconductor characterization system). Results of the repeatability test are plotted on the right of Figure 3.9 with the extracted hysteresis shown on the left. The numbers (1-4) indicated in the hysteresis plots are referring to four different testing cycles plotted in the corresponding repeatability test. With a matched result of the constant flow sensing behavior demonstrated in the repeatability test, the almost overlapped

hysteresis curve is plotted for the cantilever flow sensor with 2µm long SiNWs (shown in Figure 3.9 (a)).
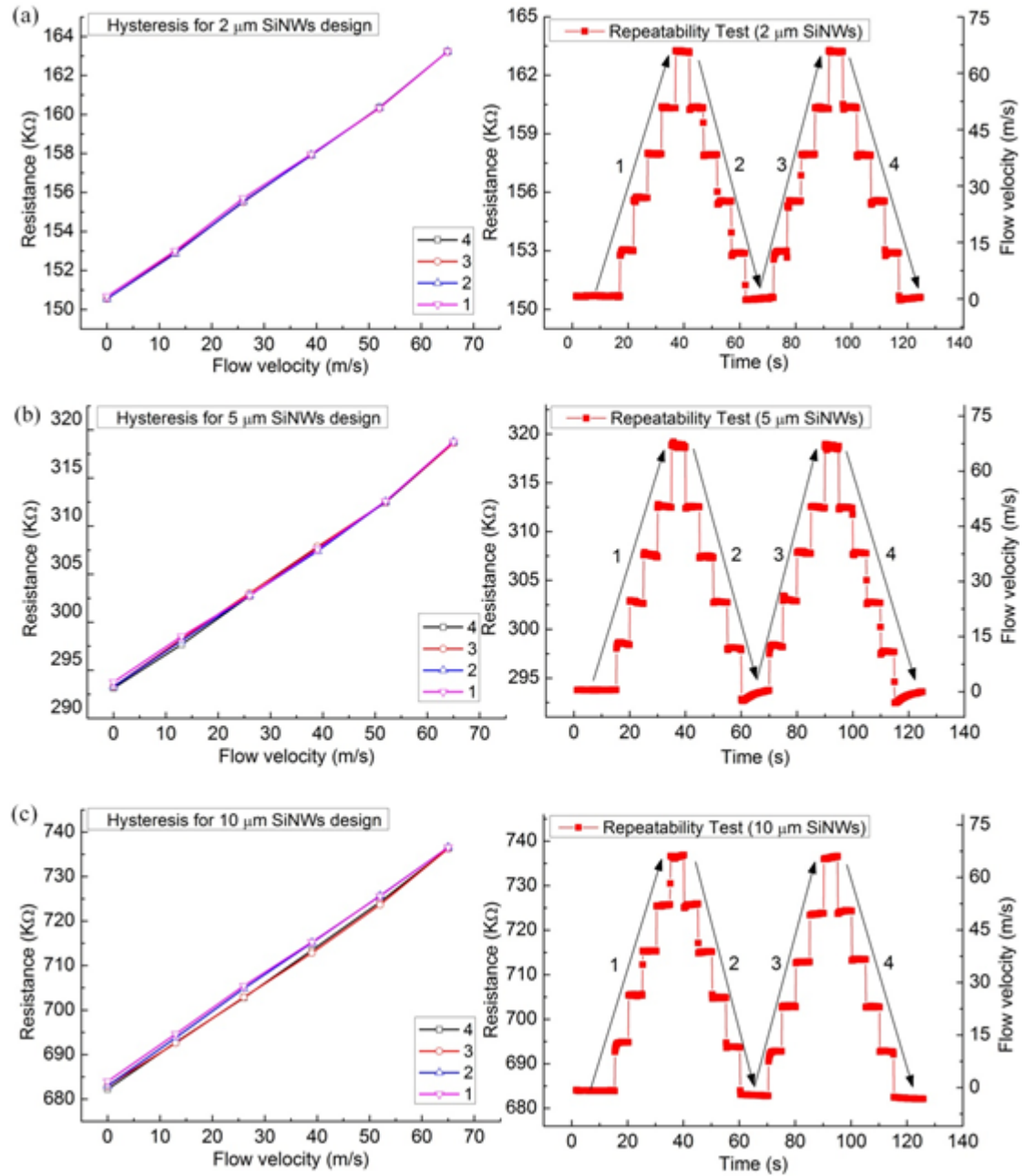
Figure 3. 9 The repeatability/hysteresis tests for cantilever flow sensors with the SiNWs length of (a) 2µm, (b) 5µm and (c) 10µm.

For 5µm SiNWs design, whereas the inconsistence is spotted during the test, especially at the region after reaching the initial state. Although the resistance is able to be restored back to almost the original value during 10 seconds before starting the

next cycle, such slightly drifts of the original resistance are accumulated to the next test cycle and result in even larger total resistance drifts. The worst situation is recorded for the design with 10μm SiNWs as plotted in Figure 3.9 (c). Similar to that of 5μm design, the resistance drifts after one complete test cycle, but unlike the 5μm design, the piezoresistance is not able to return back to the original value at the initial state during the 10 seconds interval between two test cycles. For longer SiNWs, which is located relatively far away from the supporting substrate, it is more subject to the mechanical movement. As a result, it is less immune to the air flow induced fluctuation and needs longer relaxation time for resistance to be restored. Therefore, the design with shorter SiNWs (2μm) gives better performance in term of the flow sensing consistence. The same explanation may be also applied on the larger piezoresistance variations of longer SiNWs designs at the final state shown in Figure 3.7.

In summary, the cantilever flow sensor with 2μm SiNWs design demonstrates better air sensing capabilities in terms of sensitivity, linear and repeatability/hysteresis. In addition, the higher gauge factor of 2μm will also be extracted in the following part.

3.2.2.3 Pressure validation test and gauge factor extraction

As mentioned previously, to verify the assumption of uniform load worked on the cantilever beam, a pressure regulator (ALICAT PCD series) is placed just before air flows entering the hermetic sealing base (shown in Figure 3.1). The values of feedback air pressure are taken at four different velocity points. Meanwhile, the cantilever tip deflections are captured by a white light interferometer (Veeco NT3300) at four corresponding air velocity moments. Meanwhile the FEM modeling (Abaqus

6.10) is also conducted based on same values of four recorded air pressures.
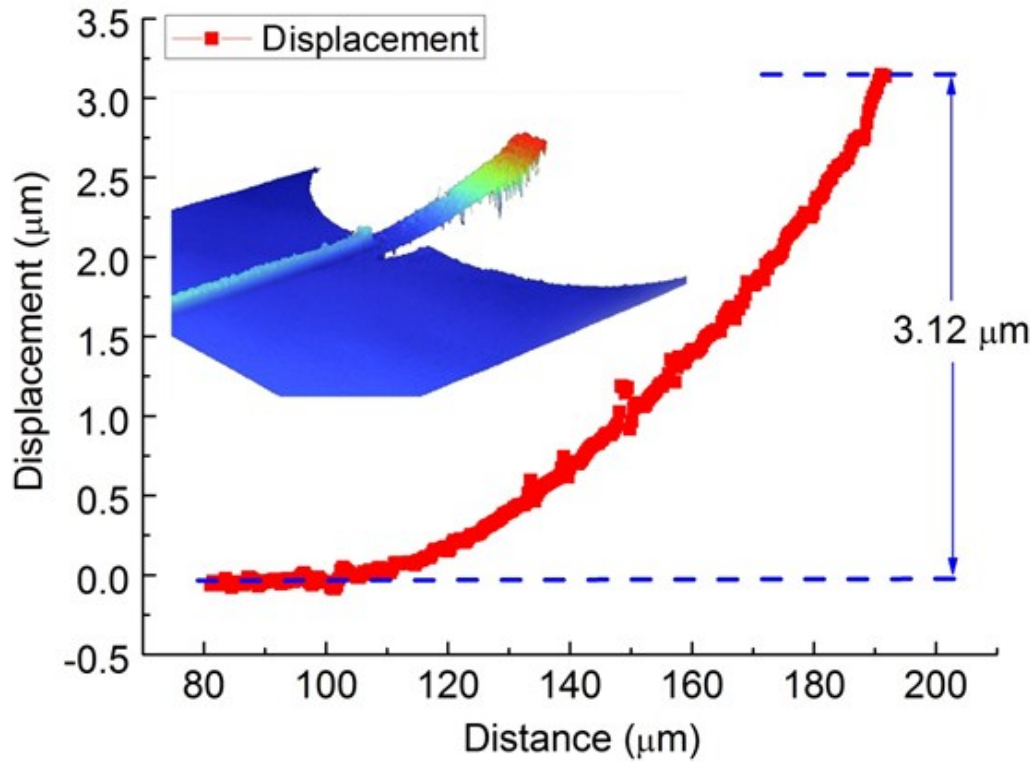
Figure 3. 10 Plot of initial deflection of the flow sensor with the cantilever size of 20μm × 90μm. The inset shows the surface profile picture captured by a white light interferometer (Veeco NT3300) system.

The final goal is to match cantilever tip deflections extracted from the FEM modeling to actual measurement results under the same applied pressure in both cases. In addition, results from theoretical calculation based on equation (3.6) are also provided as a basic reference for comparisons. The small initial tip deflections are spotted for all shapes of cantilever designs due to the unbalanced initial stress. An example of the initial stress for the released cantilever with the area of 20×90 μm^2 is demonstrated in Figure 3.10. Such initial bending is not able to be found based on theoretical calculation, but it can be estimated by applying the proper pre-stressed condition in the FEM modeling and the values of applied pre-stress are 150 MPa (tensile) for Si_3N_4 and 250 MPa (compressive) for SiO_2 [163].

Table 3. 3 Comparisons of cantilever tip deflections between measurement result (captured by Veeco NT3300) and FEM result.

Pressure (Pa)	Flow velocity (m/s)	Cantilever tip deflection (μm)		
		Veeco	FEM	Calculation
0	0	3.12	3.09	N.A
13790	13	3.48	3.47	3.44
41360	39	4.21	4.24	4.07
68940	65	4.95	4.99	4.69

As tabulated in Table 3.3, the simulation results are in a good agreement with measurement results, which validates of the assumption made in section 3.1. To further explore the piezoresistive effect of silicon nanowires, the strain (ε) on SiNWs with different lengths is extracted from the FEM modeling as well. With definition of gauge factor (G) given in equation (1.4), the average gauge factor of 75 for 2μm SiNWs is reported. For SiNWs with the length of 5μm and 10μm, the average gauge factor of 68 and 64 are extracted, respectively. These results are in a good agreement with recently reported data [14]. In general, the gauge factor is inversely proportional to the length of SiNWs. As discussed in the previous section, the longer SiNWs stay relatively far away from the supported substrate or clamp point. From the mechanical point of view, less mechanical strain is distributed at the region away from the conjunction point, thus a smaller gauge factor.

3.3   Conclusions

In this chapter, we first describe the flow sensing principle in a fully developed internal boundary situation. Confined by the physical channel length, an assumption of uniformly loaded pressure on cantilever is made and also validated by measurement results. Despite the tradeoff of slightly lower sensitivity, Si_3N_4 is used as the passivation material due to its higher Young's modulus and the tensile range stress

(compensation of initial compressive stress). In addition, with an ultra-low supply voltage (0.1V) and the high piezoresistance (> 150KΩ), the power consumption of the device is dramatically reduced to be less than 1 μW. After optimization of the device geometry factor, our reported cantilever flow sensor demonstrates the excellent air flow sensing performances in terms of the device sensitivity, linearity and repeatability/hysteresis. Compared with the recently reported designs, our SiNWs based flow sensor shows the great scalability for the device dimension variation. Moreover, such miniaturized device could be implemented in more technology oriented biomedical applications such as the blood flow sensor. Finally, the reasonable gauge factor is extracted, which is in a good agreement with the value recently reported in literature.

Chapter 4 SiNWs embedded Diaphragm Pressure Sensors with Annular Grooves for Low Pressure Sensing

We have briefly introduced the history of piezoresistive pressure sensor and pointed out the bottle neck for the current design, especially for the application under low pressure within a limited space (refer to chapter 1.2.2). As the reasonable solution, the SiNWs integrated NEMS pressure sensor validates the feasibility for using the nano-scale piezoresistor with significant improvements in sensing performance (refer to chapter 1.3). In this chapter, by leveraging the higher concentrated stress profile contributed by annular groove structures on a thin diaphragm (0.5μm thick in hinge region and 3μm thick in the rest of the diaphragm area), we successfully demonstrate a new annularly grooved diaphragm pressure sensor using embedded SiNWs as piezoresistors for the low pressure application. The reported proof-of-concept NEMS pressure sensor with a miniaturized sensing area, which suits the demands of minimum invasive implantation, can be potentially used for bio-medical applications under low pressure range.

4.1 Design Considerations

It's been aforementioned in the introduction that it is difficult to obtain a good low pressure sensing characteristics by simply reducing the diaphragm thickness of the conventional flat diaphragm structure. A balance between excellent sensing resolution and optimum linearity is always the key concern. Thus, the previously

reported flat pressure sensor [164] has to be redesigned in order to serve the purpose of low pressure detection. Rather than complicated diaphragm structures as reported [6, 102, 105, 107], only the simple structure with annular grooves and ribs around the diaphragm edge is chosen to simplify the fabrication process as well as to prove the concept.
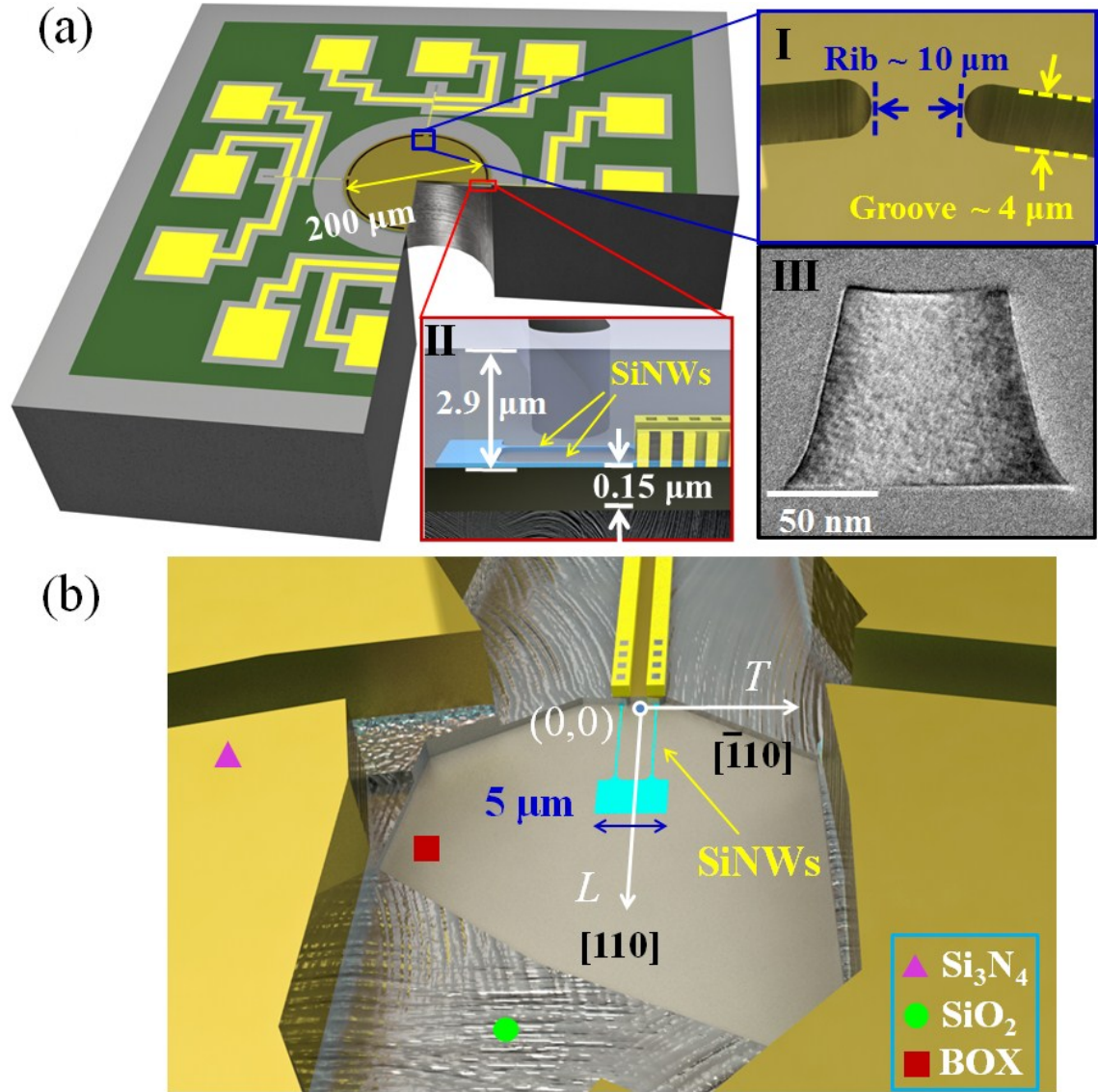
Figure 4. 1 The schematic of SiNWs embedded pressure with groove and rib structures on the circular sensing diaphragm (released from the back side); (b) The spot view in the location of SiNWs after etching back top passivation layers (2.5μm Si_3N_4 and 0.4μm SiO_2). SiNWs are patterned along [110] direction as indicated by white arrow. Inset I: the close-up view of the micro-groove; Inset II: the cross-section view of the multilayer diaphragm. Inset III: a TEM image for the cross-section of the nanowire.

The device drawing of our annularly grooved diaphragm pressure sensor is shown in Figure 4.1 (a) with the detailed groove geometry and diaphragm cross section provided in inset I & II (In Inset II, the top passivation layer (Si_3N_4) has been turned into transparent for a clearer view). According to the previous study reported by Yasukawa *et. al*. [174], the induced surface strain (ε_{total}) of the both circular boss diaphragm (structure – **B**) and circular boss diaphragm with rib (structure – **B&R**) can be expressed as following:

$$\varepsilon_{total} = \frac{3h_r\xi}{w_g^2}\varphi + \frac{\pi^2}{16(1+\beta)w_g^2}\varphi^2 \tag{4.1}$$

$$\beta = \frac{h_rw_rE_r + h(\pi aE_d - w_rE_r)}{\pi aw_gk_s} \tag{4.2}$$

Where h_r and h are the thickness of the rib/center boss and hinge region, which is the remaining diaphragm portion below groove structures and connected to the device substrate. φ is the diaphragm deflection, w_g is the width of the groove, w_r is the width of rib, and ξ is the non-dimensional coordinate of the gauge position (varies from 1 to -1). β is defined in (4.2), a is the radius of the diaphragm, E_d and E_r are the equivalent Young's modulus of the diaphragm and rib respectively. k_s is the support stiffness.

In their study, the total induced strain can be treated as the combination of rib/beam bending strain (the 1st portion of the equation (4.1)) plus the diaphragm deforming strain (the 2nd portion of equation (4.1)). When only **structure – B** is applied, the equation can be simplified by equal h_r to h. Therefore, for **structure – B&R**, the sensitivity can be further improved by reducing the thickness at the hinge region. In another word, the thickness at the boss region is virtually increased. In order to validate the assumption of a boss structure, the thickness of the center boss region should be at least 6 times of the thickness of the hinge (the remaining thickness at groove region). Additionally, one of initial conditions for the equation of boss

structure assumes a negligible bending moment at the center boss region under a given applied pressure. Thus, the mechanical stiffness at the center boss has to be the much higher than that of the hinge region. Such stiffness can be characterized by flexural rigidity as expressed in equation (4.3)

$$D = \frac{Eh^3}{12(1-v^2)}$$

(4.3)

Where E is the equivalent Young's modulus of the structure and h is the structure thickness and v is the Poisson's ratio. With a fixed equivalent Young's modulus, the stiffness is highly dependent on the diaphragm thickness. Therefore, the thickness is usually above 10μm for a good linearity according to the literature [175], especially for those with the center boss structure [101]. In our case, however, the initial diaphragm does not perfectly match the boss configuration (the ratio of the thickness between center and hinge area is only 5.5) and the center thickness may be too thin (~ 3μm as indicated in Inset II of Figure 4.1) to be considered as a rigid structure for minimizing center deflections. Nevertheless, the analysis of equation (4.1) does provide the design guideline for the reconfiguration of original diaphragm structure and to demonstrate the concept of the sensing capability for the SiNWs based NEMS device under a low pressure. The location of piezoresistors (SiNWs in our case) is usually placed along beam/rib region and buried away from the neutral axis. In our design, SiNWs are placed on the BOX layer (buried thermal oxide) and close to bottom surface as shown in Inset II of Figure 4.1. In addition, the thickness of rib should be the same as that of the center diaphragm. As indicated in the equation (4.3), hence, a smaller deflection will be observed at rib region compared to the deflection at hinge region and a resultant lower non-linearity will be accomplished [105].

Besides the sensitivity and linearity improvement for structure – B&R, another advantage of such structure is to minimize the fabrication variation due to the front to

backside misalignment. As a result of the frontside fabrication, the groove can be patterned with a relatively higher accuracy compared with the result based on backside alignments. Moreover, the well aligned groove re-defines the original stress distribution confined by the edge of the conventional flat diaphragm structure, which is released by the back side process. Such stress re-distribution is realized by concentrating the stress along the rib region [107]. Consequently, less performance variations among each individual die is ensured during the final device characterization. The detailed experimental result for minimizing the device variation will be elucidated in section 4.2. Additionally, to achieve a better sensitivity and optimum non-linearity, both groove and rib width should be kept as narrow as possible [105, 107]. However, the practical consideration limits the minimization of both groove and rib width in our case. As shown in Figure 4.1 (b), the width of the paddle connecting two nanowires is around 5μm. To tolerance alignment errors and etching processes, the width of rib and groove are set to be 10μm and 4μm respectively (Shown in Inset I of Figure 4.1).

Apart from diaphragm geometry parameters, the nanowire itself also needs to be optimized for better sensing performances. The p-type impurity concentration is firstly designed within the range of 1 to 3.5×10^{18} cm^{-3} (refer to chapter 2.2 for the detailed doping optimization). In addition, such doping level optimizes the balance between a reasonably large piezoresistive coefficient (lower the impurity higher the value) and a relatively acceptable temperature dependency of the piezoresistor (higher the impurity less the temperature induced variation) [35, 38, 40]. It has also been reported that the non-linearity component of piezoresistance is also related to the impurity concentration [109, 176] due to the non-proportional relationship between the splitting of valence band states caused by the energy band shift between heavy and

light hole [173]. Details on temperature effects will be discussed in the following chapter 4.2. Meanwhile, the cross-section geometry is another important factor to maximize the piezoresistance effect of SiNWs. The ideal cross-section should have a higher aspect ratio between width and thickness with a straight sidewall profile [14-15]. However, due to the imperfection of photolithography process, the practical shape of the cross section is always trapezoidal (as shown in Inset III of Figure 4.1). Furthermore, the resistance change due to the longitudinal (defined by L in Figure 4.1 (b)) stress component should be maximized and the resistance change caused by transverse (defined by T in Figure 4.1 (b)) stress component has to be kept as minimum for a better overall performance under a given applied normal pressure. According to equation (1.5), the longitudinal piezoresistance effect can be enhanced by reducing the cross section area of the silicon nanowire. On the other hand, the effect of transverse piezoresistance can be minimized by proper design of the aspect ratio, which is defined as the nanowire thickness divided by its mean width. With the aspect ratio close to 1 (thickness ≈ width), the stress transmission ratio = (σ_T/σ_0) along the transverse direction can ideally approximate to 1, therefore, maximizing the transformation of stress component in the longitudinal direction. Here, σ_0 is the normal stress applied to the substrate. Meanwhile, the change of aspect ratio does not affect the stress component along the longitudinal direction. The detailed process and optimization of the SiNWs cross-section geometry have been described in chapter 2.1.

4.2 Testing result and discussion

4.2.1 Sensitivity and Linearity

The optical image of the release diaphragm with groove and rib structures is given in the inset of Figure 4.2. The zoom-in image on the groove region indicates a

successful etching stop on beneath SiO_2 layers and this is further verified by capturing the diaphragm topography using white light interferometer (Veeco NT3300). With the depth of groove about 2.57μm, the over etch of SiO_2 layer (~ 70nm) is about 12% of the total thickness of SiO_2 layers (400nm PECVD SiO_2 layer plus 145nm BOX layer).
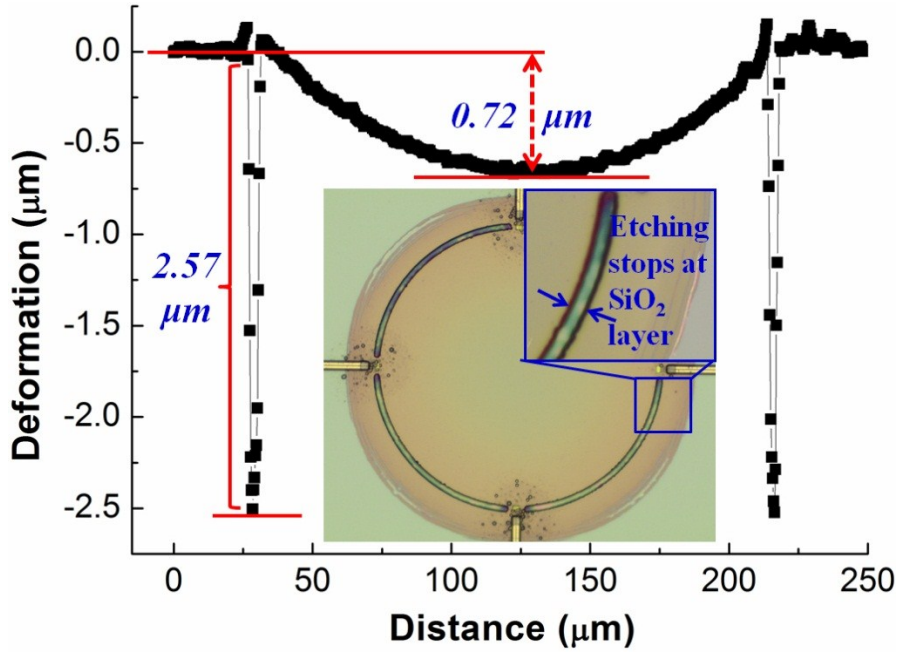
Figure 4. 2 Plot for the initial deflection the annularly grooved diaphragm. The diaphragm deforms downward and forms a concave shape. Inset shows the optical image of the pressure diaphragm and a zoom-in view of the groove.
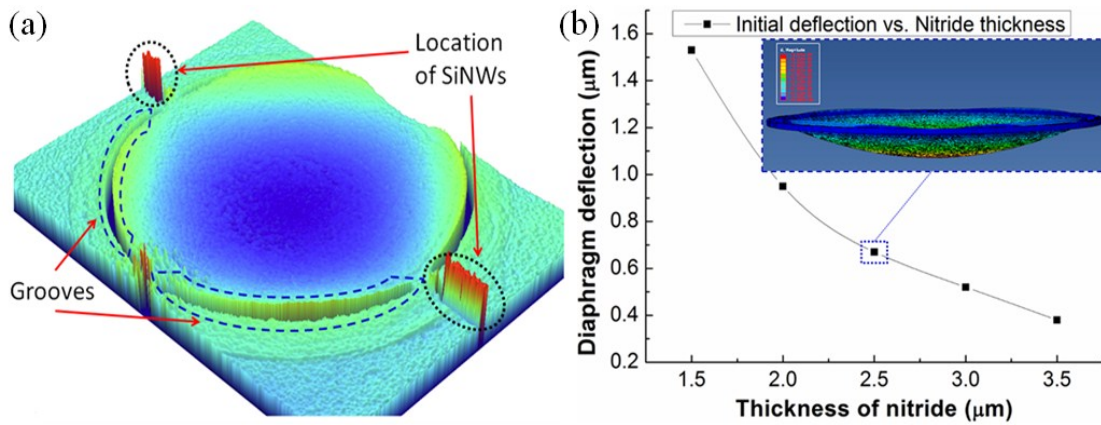
Figure 4. 3 (a) The surface profile captured by Veeco white light system and (b) the simulated relationship between the nitride layer thickness and the initial diaphragm deflection. The inset shows the simulated diaphragm shape (concave) when a 2.5μm thick nitride is used as the cladding layer

However, it is also plotted as the trade-off of a significantly reduction in the hinge

region (thus the reduction of the flexural rigidity), the initial diaphragm deflection of 0.72μm is found and it is about a quarter of the total diaphragm thickness (~ 3μm). To further understand the initial diaphragm deflection, the simulation on the effect of residual stresses contributed by the multi-layered diaphragm (named in the sequence from bottom to top: BOX layer, PECVD oxide layer and PECVD low stress nitride layer) is conducted. The simulation is conducted by using Abaqus 6.10 and all parameters used in simulation are listed in Table 4.1. The result of diaphragm deflections with respect to different thicknesses of nitride layer is plotted in Figure 4.3 (b) and it reveals the inverse proportionality between the diaphragm deflection and the cladding nitride layer thickness. In addition, both the simulation result (inset of Figure 4.3 (b)) and the measurement data (Figure 4.3 (a)) indicate a concave shape diaphragm. The value of the simulated deflection (~0.67μm) is very close to the experimental data (~0.72 μm) captured by Veeco white light system. As a rule of thumb, a deflection less than 10 % of the total diaphragm thickness will introduce a mechanical non-linearity of 0.2 % and a deflection less than 30 % of the total thickness will cause a non-linearity component as large as 2 %. For a deflection large than 30% of the diaphragm thickness, this assumption of the small deflection principle is no longer valid [177].

Table 4. 1 Material properties applied in the Finite Element Method (FEM).

Material	Young's modulus	Poisson's ratio	Residual stress (MPa)	Density (g/cm^3)
Si$_3$N$_4$	170 GPa	0.27	100 (tensile)	3.44
SiO$_2$	60 GPa	0.20	-250 (compressive)	2.65

To verify the performance difference of the SiNWs based pressure sensor with the new annularly grooved diaphragm in contrast to the previously reported flat

diaphragm counterpart, the percentage of resistance changes over the initial resistance (when no pressure is applied) are measured in the form of *ΔR/R (%)* by varying pressure changes on *X*-axis. The testing is firstly conducted under room temperature (25 ^{0}C) with supply voltage of 0.5 V. The resistance change is measured by the semiconductor characterization system (Keithley 4200-SCS) with the compressed air source applied by the pressure regulator (ALICAT PCD Series) from the backside of the device. As a result, piezoresistors will experience a uniform tensile stress. Please refer to Figure 3.4 in chapter 3.2.1 for details of the similar testing setups.
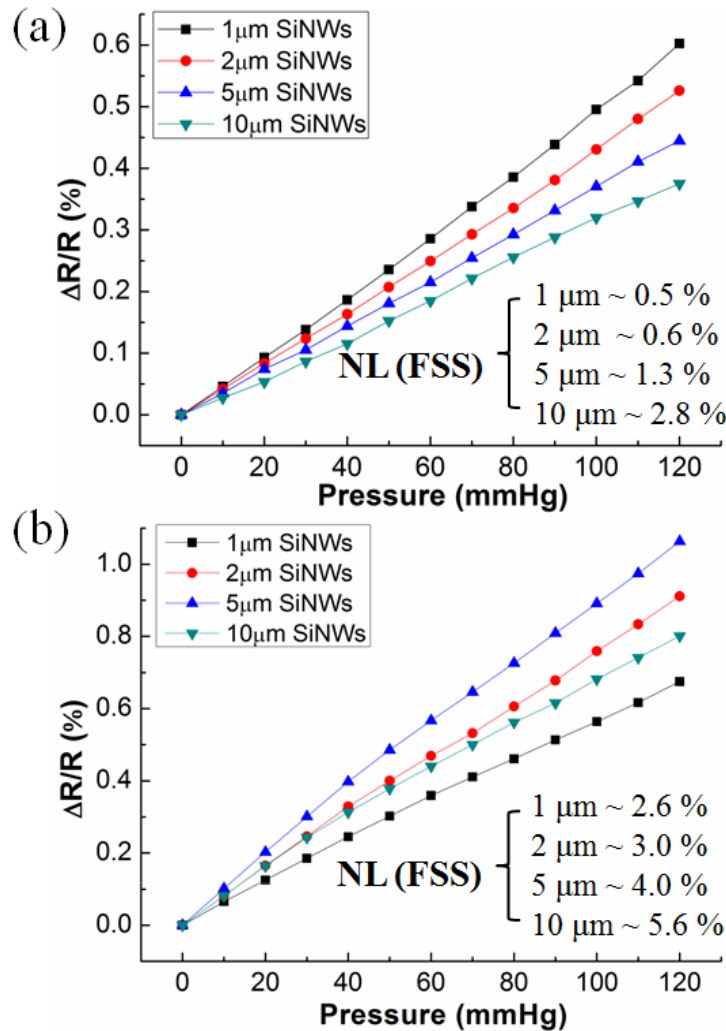
Figure 4. 4 Plots of the percentage changes of resistance (*ΔR/R (%)*) with respect to pressure changes for (a) the conventional flat diaphragm SiNWs pressure sensor and (b) the annularly grooved diaphragm SiNWs pressure sensor. The calculated nonlinearity for pressure sensors with different lengths of SiNWs (1 μm, 2 μm, 5 μm and 10 μm) is given in insets.

Figure 4.4 (a) illustrates the resistance change of the traditional flat diaphragm pressure sensor, the maximum average percentage change (~ 0.6 %) occurs for the 1 μm SiNWs embedded pressure sensor among other designs with longer length of embedded SiNWs. The reasonable explanation has been addressed based on changes of stress distribution profiles along the radial direction of the diaphragm [164]. When SiNWs are located away from the diaphragm edge, the average longitudinal stress experienced along the nanowires gradually decays as the stress distribution profile shown in Figure 4.5 (f). In the case of the grooved diaphragm pressure sensor, the maximum average percentage change of 1.07 % for 5 μm SiNWs pressure sensor is observed (Figure 4.4 (b)). In contrast to the 5 μm SiNWs embedded flat diaphragm pressure sensor, the improvement of percentage changes is about 2.5 times and this change is in a good agreement with the finding of the increment of the average stress distribution along longitudinal direction from the simulation.

The non-linearity (*NL*) for both the flat diaphragm and the grooved diaphragm pressure sensor with different lengths of SiNWs over full-scale span (FSS) are also calculated based on equation (4.1) [173] and provided in insets.

$$NL = \frac{R(\text{T}) - \{[R(\text{T}_m) - R(0)](\text{T}/\text{T}_m) + R(0)\}}{R(\text{T}_m) - R(0)} \qquad (4.4)$$

Where, *R*(0) & *R*(T) are output resistance values at the initial condition (pressure = 0) and a given pressure status (pressure = T), respectively. The pressure varies from 0 to T_m (maximum pressure applied). As predicted from the initial deflection profile plotted in Figure 4.2, a larger non-linearity is introduced after reconfigurations of the original flat diaphragm structure. Beside an extra increment of non-linearity, an obvious sensitivity shift from the previously reported flat diaphragm with 1μm SiNWs to the currently reported grooved diaphragm with 5μm SiNWs is observed. To understand this shift, the FEM is conducted and zoom-in views of the beam/rib

structure are also provided in Figure 4.5 (b)-(c) with a reference image showing the

high stress distribution region from FEM (Figure 4.5 (a)).
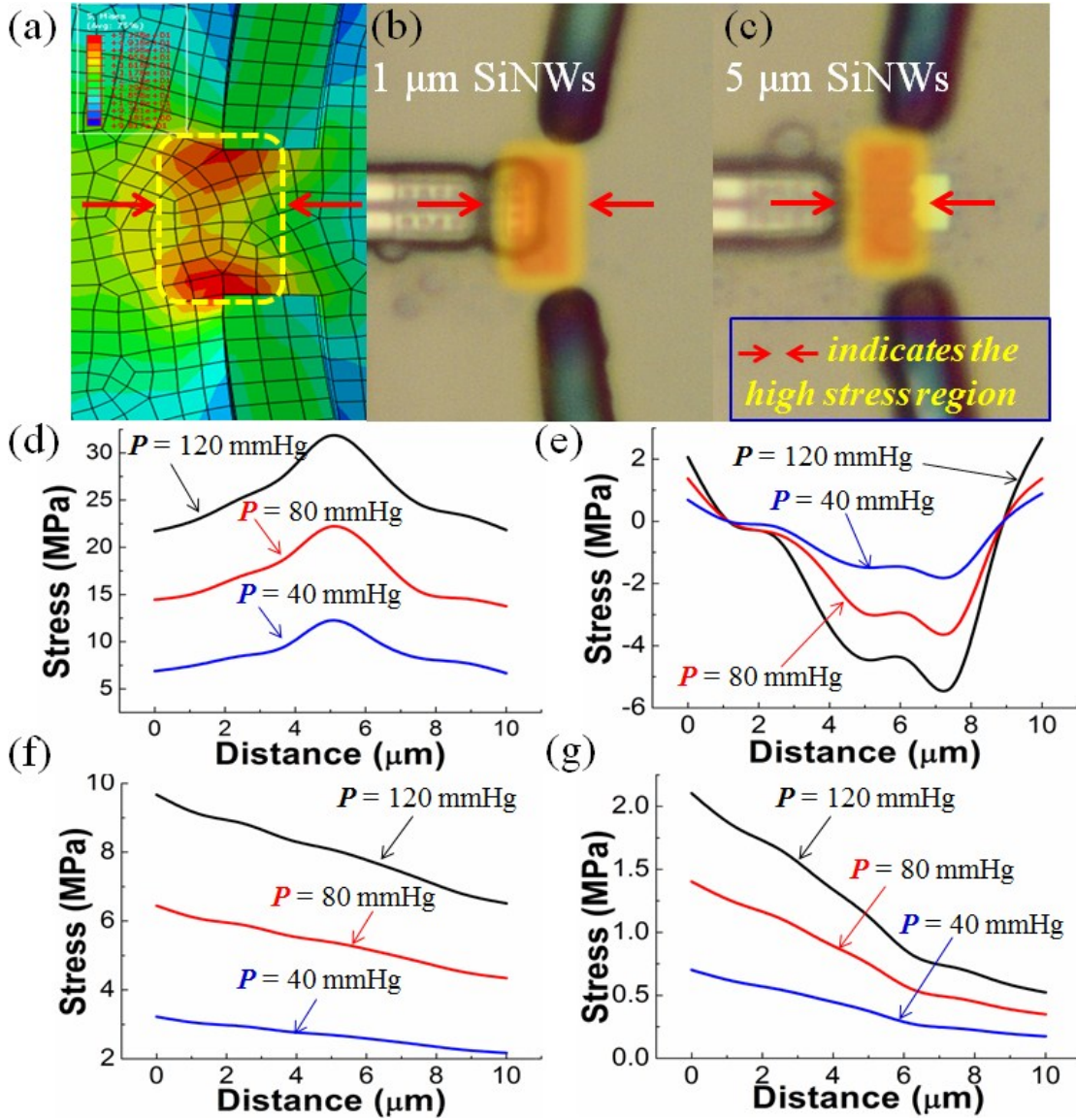
Figure 4. 5 (a) Illustration of high stress region captured from FEM, (b) - (c) zoom-in optical images of rib region for 1 and 5μm SiNWs designs respectively. Simulation results of (d) - (e) extracted stress distributions for both longitudinal and transverse stress component along *L*-direction of the grooved diaphragm pressure sensor, (f) – (g) extracted stress distributions for both longitudinal and transverse stress component along *L*-direction of the conventional flat diaphragm pressure sensor

As depicted in Figure 4.5 (a), the highest stress region is located slightly behind

(around 2μm behind) where groove structures are fabricated along the rib. The

location of 1μm SiNWs (shown in Figure 4.5 (b)) is out of the high stress region,

whereas, 75~80% portion of 5μm nanowire (shown in Figure 4.5 (c)) is completely merged within such high stress region. The detailed stress distribution profiles along the rib (*L*-direction defined in Figure 4.1 (b)) under three different external pressures are plotted in Figure 4.5 (d). The point (*0, 0*) (indicated in Figure 4.1 (b)) is defined as the origin for the *X-axis* (distance). With the same explanation, the average stress distributed along 2μm SiNWs is higher than that of 1μm SiNWs design but lower than the average stress of 5μm SiNWs design. For the 10μm SiNWs, however, it is too long to be entirely confined within the high stress region, thus, experiencing a lower average stress. In addition, the transverse stress distribution profile with the same origin, span and direction are plotted in Figure 4.5 (e) as well. Unlike the linearly decayed stress distribution from edge (tensile stress) to the center (compressive stress) in the case of flat diaphragm pressure sensor (indicated in Figure 4.5 (g)), it is worth noting that the stress distribution profile is no longer linear after fabrication with grooves. The stress profile ramps from the small tensile down to relatively larger compressive region and reaches its maximum (compressive) at distance about 7μm away from the origin. It then ramps up again to tensile stress region. Although this stress change does not dominate the difference in the final resistance value, it theoretically reduces the average transverse resistance changes by approximate 10%, if the same length (7μm) of the nanowires is allocated within exact the compressive stress region. Hence it leads to improvement of the total resistance change as defined in equation (1.5). However, the larger transverse stress will also cause an increased non-linearity component regardless of the stress polarity (both compressive and tensile) [173], therefore, such compressive stress profile may also provide a negative contribution to the device linearity. To further understand the non-linearity component, a more closed-from expression of non-linearity between an

applied pressure and the final resistance change of a given piezoresistor can be described as the following [174]:

$$NL_{p-R} = NL_{\varepsilon-R} + NL_{\omega-\varepsilon} + NL_{p-\omega} \qquad (4.5)$$

Where NL_{p-R} is the total non-linearity component between applied pressure and final resistance changes; $NL_{\varepsilon-R}$ is non-linearity component introduced between strain/stress and resistance changes; $NL_{\omega-\varepsilon}$ is non-linearity component introduced between deflection and strain changes; $NL_{p-\omega}$ is non-linearity component introduced between applied pressure and mechanical deflection changes. We have examined non-linearity components contributed by both $NL_{p-\omega}$ (~ 2 % due to the initial diaphragm deflection) and $NL_{\varepsilon-R}$. The $NL_{\omega-\varepsilon}$ is usually small and can be removed by an external circuit. For instance, by applying the Wheatstone bridge structure, $NL_{\omega-\varepsilon}$ can be further minimized [174].

4.2.2 Improvement on Process Variations
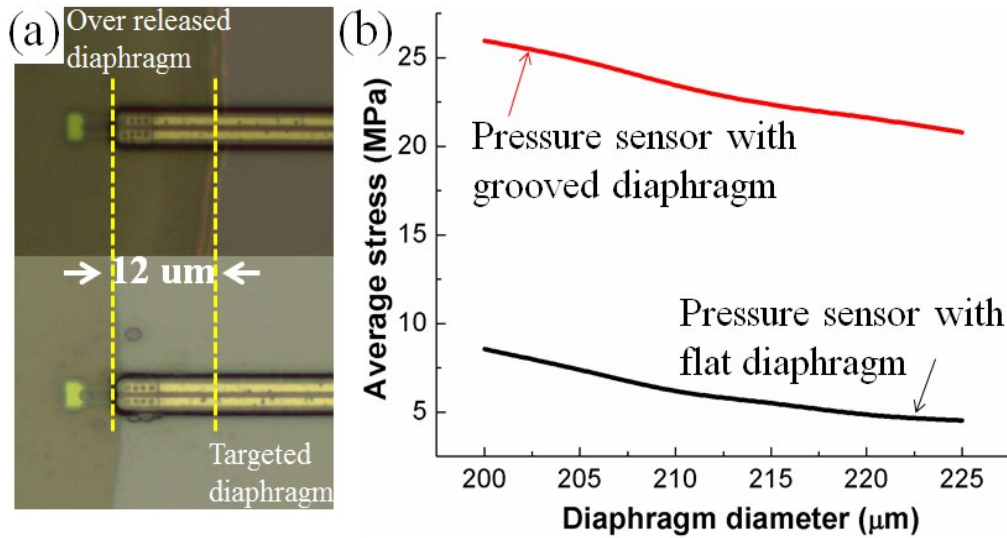
Figure 4. 6 (a) Optical images of over-release diaphragm (top) and targeted diaphragm (bottom) with embedded 5μm SiNWs, (b) Simulation results of extracted average stress along 5μm SiNWs for both grooved and flat diaphragm pressure sensor with respect to the diaphragm diameter variation.

We have addressed variations of pressure diaphragm due to the non-uniform

backside DRIE process (refer to chapter 2.4.1). The resultant stress/strain profile will deviate from the designed location, where SiNWs are fabricated. Without change the main process flow, however, the stress/strain distribution along the diaphragm edge can be re-concentrated along SiNWs after the diaphragm reconfiguration with groove structures.

As illustrated in Figure 4.6 (a), the backside release process has introduced significant fabrication variations and the over-release of the diaphragm can be up to 12% from the targeted diameter of 200µm. As a consequence, the performance of the released device varies dramatically from reticle to reticle. The average stress distributed along 5µm SiNWs with respect to the diaphragm size variation for both the flat and the grooved diaphragm pressure sensor is extracted by using FEM (plotted in Figure 4.6 (b)). For a flat diaphragm structure, the amount of average stress drops more than 45 % by varying the diaphragm diameter from 200µm up to 225µm. In case of the grooved diaphragm, such diameter variation affects the average stress change up to only 18 %. The FEM is conducted based on a linear perturbation model. For a further verification, the experiment is conducted on different pressure sensor samples (n = 10) with various diaphragm diameters. Output resistance variations for 5 µm SiNWs embedded in both flat and groove diaphragm pressure sensor are shown in Figure 4.7. The blue curve with error bars reflects results for the flat diaphragm pressure sensor (referring to bottom *X*- and left *Y*-axis) with the deviation of resistance changes up to 33% of its mean value at pressure of 120 mmHg. On the other hand, as plotted in red curve with error bars (referring to top *X*- and right *Y*-axis), the variation of diaphragm size only introduces 14 % of performance differences to the annularly grooved pressure sensor within the same pressure range. The obvious improvement of the device sensing performance over process variations is hereby

reported and it is contributed by the groove structure, which forces the stress distribution along the rib.
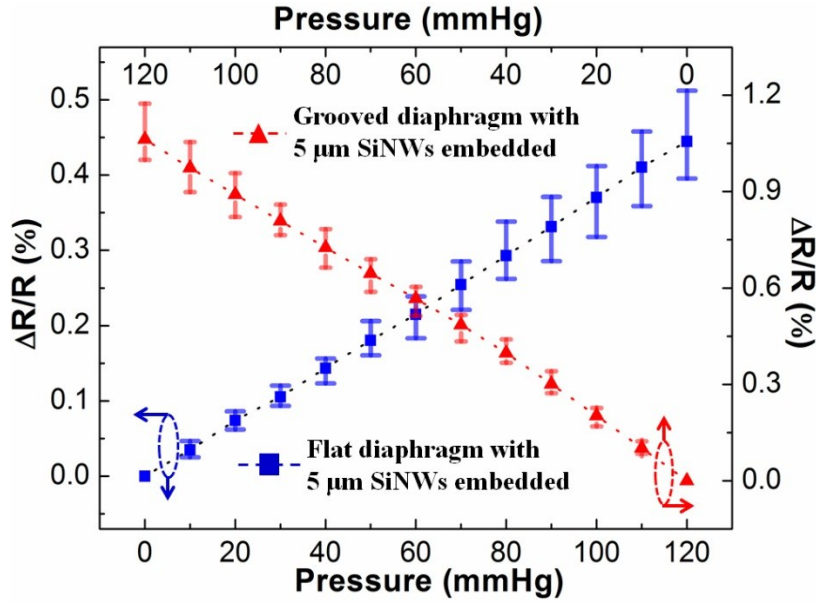
Figure 4. 7 Plot of output resistance variations with the blue curve and error bars for the flat diaphragm pressure sensor (refer to bottom *X* and left *Y*-axis) and the red curve and error bars (refer to top *X* and right *Y*-axis) for the grooved diaphragm pressure sensor with 5 μm SiNWs embedded in both cases.

The reported device is targeted to proof-of-concept for the sensing capability of SiNWs embedded sensor under a low pressure and the design has not been completely optimized yet. Further sensitivity improvement can be realized by changing circular diaphragm to a square shape. This change may lead to the sensitivity improvement up to 60 % base on flat plate design theory [177]. Additionally, the optimum location of SiNWs with respect to the annular groove has not been determined. The location of 1μm SiNWs can be re-adjusted to completely within the high stress region. This will further improve the piezoresistance changes by ~ 40 % due to the reported higher average stress experienced along 1μm SiNWs than that of 5μm design. The orientation of shorter SiNWs can also be re-aligned along the tangential direction (*T*-direction as defined in Figure 4.1 (b)) without increasing the width of rib. As a result, further sensitivity enhancement will be achieved due to a relatively uniform

average stress along the tangential direction at the narrow rib. In addition, non-linearity components will also be compensated among piezoresistors, when they are subjected to lateral stress [178]. Furthermore, the dimension and thickness of both rib and groove can be refined for a higher stress distribution profile and lower non-linearity.

4.2.3 Temperature Effects

Temperature variation is another key factor, which affects several parameters like material property, feature geometry and mostly importantly the piezoresistive effect [28, 35, 179]. The contribution from other temperature dependent factors varies and is relatively smaller compared with that from the piezoresistor itself [108]. For the p-type piezoresistor, the reported experimental result reveals the dependency of shear piezoresistance coefficient on both impurity concentrations and temperature variations [38, 40]. A more general expression for the relationship between the pieozresistance and its temperature dependency is defined by Y. Kanda [34] as:

$$\Pi(N,T) = P(N,T) * \Pi(300) \tag{4.6}$$

Where $\Pi(N,T)$ is the piezoresistance coefficient with an impurity concentration N at a temperature T. $\Pi(300)$ is the piezoresistance coefficient at temperature of 300 K. $P(N,T)$ is the piezoresistance factor and can be expressed as:

$$P(N,T) = \frac{300}{T \ln(1+e^{E_f/kT})(1+e^{-E_f/kT})} \tag{4.7}$$

Where, the E_f is the Fermi energy and it is related to the impurity concentration. It has been reported that equation (4.7) may be suitable for the first-order approximation and the simulated result matches the experimental data in case of pure circular and square diaphragm based pressure sensors [108]. In order to explore the temperature response of our device, the hot plate is used as the heat source. Temperature changes are

monitored by thermocouple with accuracy around ±2°C of its display value. The device is assembled on top of an aluminum block by an acrylic plate. The gasket is used to surround the testing sample for air sealing purpose. The air pressure is applied from the backside of the test sample by a pressure regulator. The similar hermetic sealing is also applied in the test for the cantilever flow sensor (refer to chapter 3.2.1). The electrical path is established by probing bonding pads through a small opening window on the acrylic plate and resistance changes are recorded by the parametric analyzer. The detailed setup and the schematic for hermetic sealing are shown in Figure 4.8.
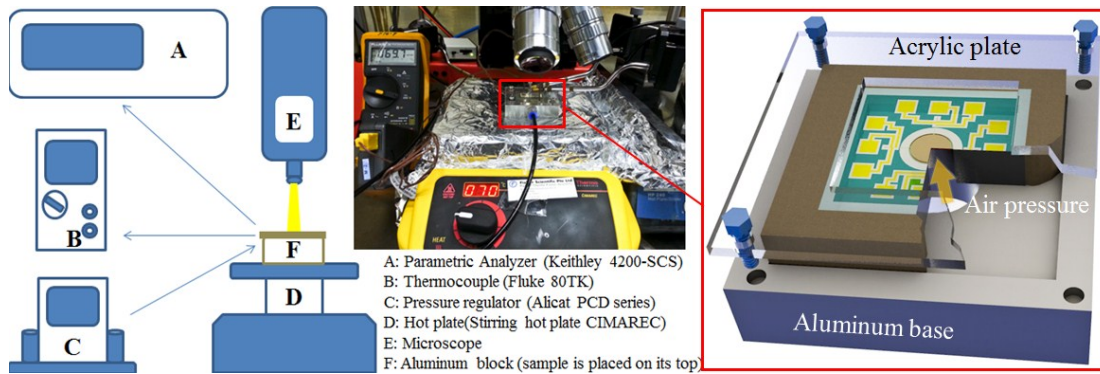
Figure 4. 8 Testing setups for the measurement of temperature response of the reported pressure sensor.

The response of the device is examined within temperatures varying from 27°C (room temperature) to 70 °C, which is a reasonable temperature range for most bio-medical related applications. The tip portion of the thermocouple is closely attached on the top surface of the aluminum block (just beside the test sample). Once the reading from the thermocouple is stabilized, another 20 minutes interval is spent before tightening the acrylic plate by screws. This minimizes any testing errors introduced by the setup. Additionally, the entire hot plate is covered with aluminum foils, which is connected to the common ground, to reduce the noise signal generated from the testing instrument. The temperature testing result of the grooved pressure

sensor with 5μm SiNWs is plotted in Figure 4.9. The obvious sensitivity drop over temperature increment is reported. Compared with the output resistance change at room temperature (27°C), this drop of output performance is as large as 23% at 70°C. Contrary to the sensitivity degradation, the linearity component improves at higher temperature. Based on equation (4.4), the non-linearity under the full scale span is around 3 % (shown in the set of Figure 4.9) at 70°C. Such temperature dependent linearity change is in a good agreement with the literature [103].
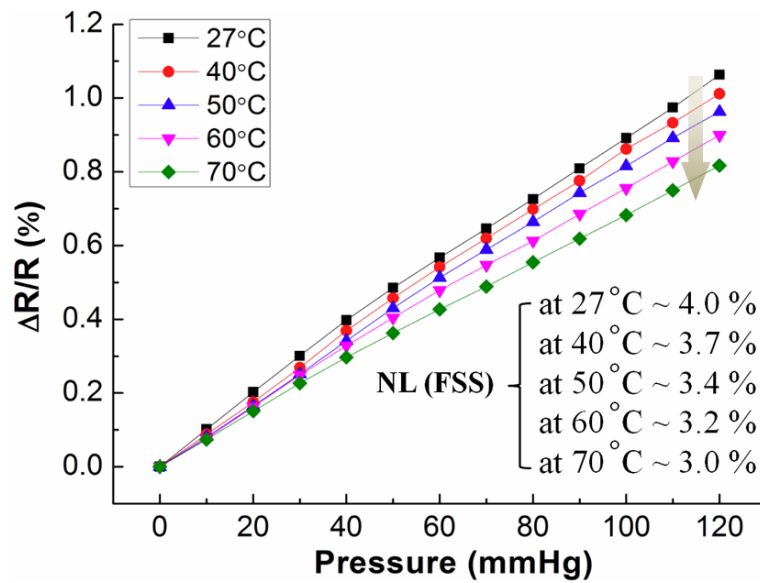
Figure 4. 9 Output resistance changes under different ambient temperatures (27°C to 70°C). The plotted data is measured from reported groove diaphragm pressure sensors with 5μm long SiNWs as piezoresistors. Insets show the non-linearity (NL) component with respect to outputs at different temperatures.

4.3   Conclusions

To provide a clearer view for the performance of the grooved diaphragm based SiNWs sensing device under a low pressure, especially for bio-medical applications, a comparison is tabulated in Table 4.2 with all references reported for bio-medical applications except our previous work. It is shown in Table 4.2 that our reported SiNWs based devices demonstrate the great scalability (indicated in column 4). The

sensitivity (($\Delta R/R$)/mmHg) for all devices is also summarized in column 5. It seems that the performance is highly dependent on the area of sensing diaphragm. In fact, the relationship between the effective sensing area and the device sensitivity should be proportional as predicted by the plate theory [111]. Thus, a fair sensitivity comparison among all types of pressure sensing devices is listed in the last column of the table. After normalizations of variations in the effective sensing area, the sensitivity improvement of the previously reported flat diaphragm based SiNWs pressure sensor is almost an order over other literature reports. With a further improvement benefited by the groove structure, the currently reported device boosts up the sensitivity by at least 17 times compared with results reported by other groups. Such significant improvement proves the feasibility for implementing SiNWs based device for low pressure sensing applications by simply reconfiguring the device diaphragm.

Table 4. 2 The comparison of bio-medical piezoresistive pressure sensing devices between this work and other reported designs.

Ref.	Applications of sensing	Sensing element	Effective sensing area (μm^2)	Sensitivity (($\Delta R/R$)/mmHg)	Normalized Sensitivity (($\Delta R/R$)/mmHg/μm^2)
[180]	Intracranial pressure	P-doped polysilicon wires	$\pi * 500^2$ = 785398	~ 13×10^{-5}	~ 1.66×10^{-10}
[102]	Cardiovascular blood pressure	P-doped silicon wires	$600 * 600$ = 360000	~ 4×10^{-5}	~ 1.1×10^{-10}
[78]	Coronary blood pressure	Polysilicon strain gauge	$100 * 100$ = 10000	~ 0.07×10^{-5}	~ 0.7×10^{-10}
[181]	Intraocular pressure	NiCr	$5400 * 5400$ =29160000	~ 80.8×10^{-5}	~ 0.28×10^{-10}
Previous work (Flat)	Other applications	P-doped SiNWs	$\pi * 100^2$ = 31416	~ 5×10^{-5}	~ 15.9×10^{-10}
This work (Groove)	low pressure bio-medical purpose	P-doped SiNWs	$\pi * 100^2$ = 31416	~ 8.92×10^{-5}	~ 28.4×10^{-10}

In summary, the new annularly grooved diaphragm pressure sensor with SiNWs

embedded as a piezoresistor is reported here. Various design considerations for both sensitivity improvement and minimization of nonlinearity have been discussed in detail. Experimental results are summarized and analyzed with respect to results from the previous flat diaphragm based SiNWs pressure sensor. Both FEM and measurement data explain the benefit of the groove structure that forces the stress to be concentrated around the rib region and results in a greater resistance change. The performance variation of the device over a reasonable temperature range is examined. A table is also summarized with an explicit indication for the enhancement of SiNWs based devices over other reported traditional piezoresistive pressure sensors. Benefiting by the superiority of SiNWs, the reported proof-of-concept device with the groove diaphragm structure further enhances the sensing capability and fulfills the demand for working under the low pressure range required by implantable bio-medical applications.

Chapter 5   CMOS fabricated Silicon Neural Probe with SiNWs based Mechanical Strain Sensing Element

It has been discussed in chapter 1.3; the challenge for integrating the built-in integrated circuit into the neural probe is mainly attributed to the process incompatibility between the standard CMOS fabrication for the integrated circuit and the sequential MEMS process for the neural probe. To address this issue, we have developed a Si-based neural probe with highly doped (i.e. highly electrically conductive) Si to replace Au metal as electrode site in the neural probe thus allowing a fully CMOS compatible MEMS fabrication process. On the other hand, as it is generally believed that the reliability of the neural probe is critically dependent on the brain tissue response triggering from the mechanical stain on the brain tissue due to the probe insertion and the micro-movement at the probe-tissue interface, arising from physiological event (e.g. respiration, pulsation) after insertion, Hence, in this work, we have integrated the SiNWs based mechanical stain sensing element into the neural probe through the same fabrication process by leveraging different doping profiles on the single crystal silicon layer.

As illustrated in Figure 5.1 (c), two sets of SiNWs with moderate P-type doping (highlighted in blue boxes along the shank) are fabricated at both the middle and base of probe shank for the purpose of strain sensing. Full Wheatstone bridge structures (as indicated in upper insets of Figure 5.1 (c)) are applied for a higher sensing resolution and a better noise immunity. Four highly P-doped silicon electrodes with a diameter

of 50μm and a pitch of 200μm (refer to bottom inset of Figure 5.1(c)) are located at the tip of probe.
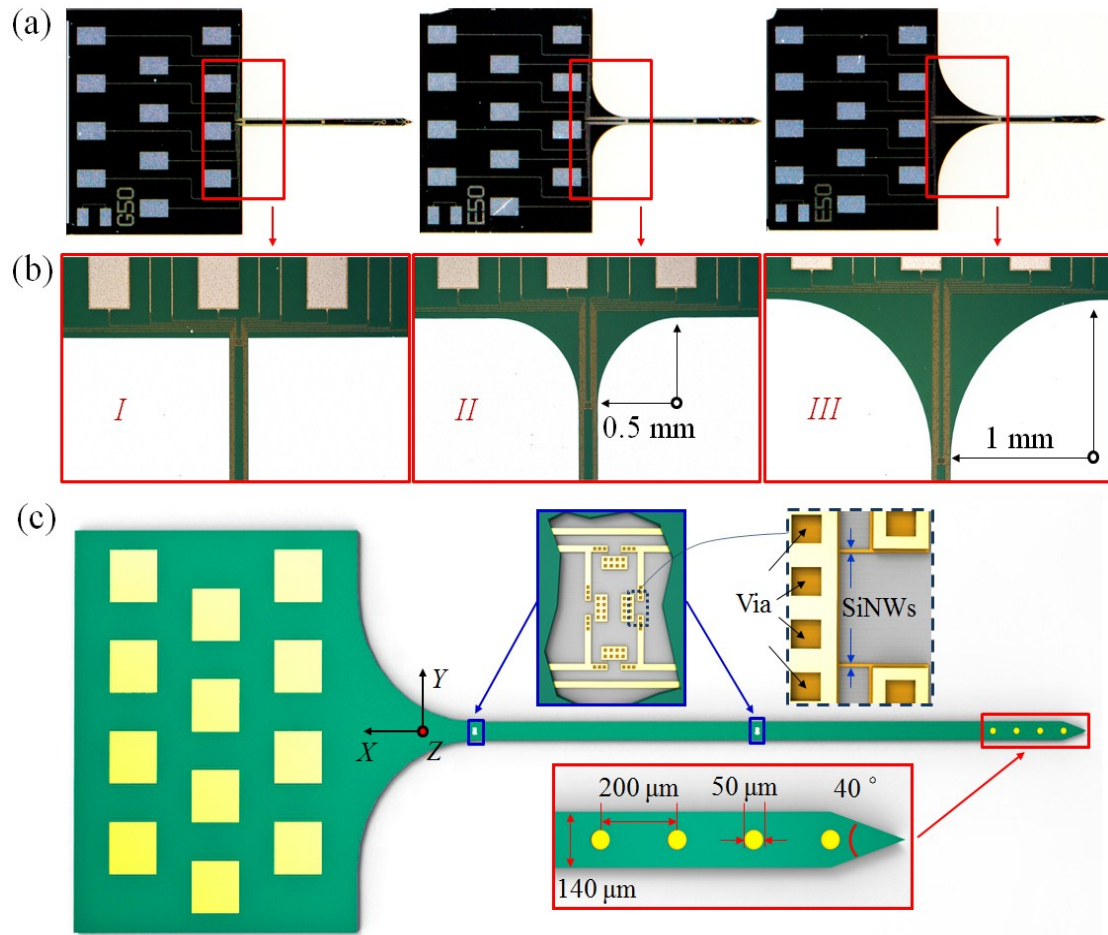
Figure 5. 1 (a) Device photos of silicon nanowires (SiNWs) embedded neural electrode probes with fixed shank length ~ 3mm. (b) The optical zoom-in views on three different base structures (*I-III*). (c) The general schematic drawing of the probe with insets show four pairs of SiNWs configured in a Wheatstone bridge structure and the detailed layout of electrodes at the tip.

In addition, three different shank base designs (as illustrated in Figure 5.1 (a) & (b)) are to verify the strain sensing function of SiNWs against the probe geometry variation. The detailed fabrication step on SiNWs embedded neural electrode probe are presented in chapter 2. Furthermore, nano-composites including multi-wall carbon nanotubes (MWCNTs) plus Au nanoparticles are coated on silicon electrodes to facilitate a larger amount of ion transportations through the electrode-electrolyte interface, thus achieving a better charge storage capacity (CSC) [182-183]. Both

coating adhesions and neural recording performance are validated through impedance spectroscopy and *in vivo* characterization. The strain sensing feature of probe is firstly examined through experimental buckling test and sequentially verified with the acute implantation. The *in vivo* acquisition of strain information provides not only the probe insertion mechanics but also the first time demonstration for the possibility of achieving the mechanical stain on the tissue from the respiratory behavior of surgical subject.

5.1   Recording Electrodes

The recording of neural electrical signals helps the paralysis patient to communicate with the external environment and researcher to have a better understanding on brain functions. Additional coatings on the pre-fabricated neural electrode improve the interfacial impedance at the probe-tissue interface leading a better quality of the recorded signals. In the following contents, we will briefly discuss the charge injection mechanism and introduce the composite coatings of multi-wall carbon nanotubes (MWCNT) mixed with Au nanoparticles.

5.1.1 Charge Injection Mechanisms

Generally, recording electrodes are made from metallic conductors and the charge conduction at the electrode-tissue interface requires mediating the transition from electron flow in the electrode to ion flow in the tissue [140]. The charge conduction can either be capacitive charging, which is involving the charging and discharging of the electrode-electrolyte double layer, or faradaic reaction, in which surface-confined species are oxidized and reduced. Capacitive charging can be either electrostatic, involving purely double-layer ion-electron charge separation due to electrolyte

dipole orientation, or electrolytic, involving charge stored across a thin, high-dielectric-constant oxide at the electrode-electrolyte (tissue) interface. Faradaic reactions involve the transfer of an electron across the electrode-electrolyte interface and require that some species, on the surface of the electrode or in solution, undergo a change in valence, i.e., are oxidized or reduced. For noble metal electrodes, primarily Pt and PtIr alloys, the reversible faradaic reactions are confined to a surface monolayer and these reactions are often described as pseudocapacitive, although electron transfer across the interface still occurs [184]. Charge can also be stored and injected into tissue from valence changes in multivalent electrode coatings that undergo reversible reduction-oxidation (redox) reactions. These coatings, which are typified by iridium oxide (IrO_x) and exhibiting both electron and ion transport within the bulk of the coating.

In principle, capacitive charge-injection is more desirable than faradic charge-injection because no chemical species are created or consumed through the stimulation process. However, the double-layer charge capacitance per unit area of the metal at electrode-electrolyte interface is extremely small (~10 $\mu F/cm^2$). A higher capacitive charge injection is only possible with the porous surface by employing high dielectric constant coatings. Moreover, 3D structures created by the coatings provide much larger electrochemical surface area (ESA), thus, further enhance the charge storage capacity (CSC) [140].

Recently, the emerging material like carbon nanotubes (CNTs) has drawn the great interest by researchers with its nearly capacitive charge injection behavior [185]. Besides the excellent mechanical property and the superior CSC, randomly oriented MWCNTs have been reported with the capability of forming intimate contacts with cells and facilitate the neuron growth [186-187]. Moreover, the MWCNTs have been

widely incorporated with other conductive materials to establish better electrode-neuron interfaces [136-137, 186]. Benefiting by high conductivity, minimal toxicity and fabrication simplicity, Au nanoparticles is another promising conductive material introduced in the neural probe [137]. In addition, remarkable performance improvements after coating the incorporative composite consisting of both CNTs and Au nanoparticles have been recently reported, but the application of this composite material is mostly limited on metal electrodes [182, 189]. Here, we have deposited such coating on the highly doped Si electrode. Detailed setups, coating procedure and improvement after coating will be discussed in the next section.

5.1.2 Electroplating of Nano-Composite and Surface Adhesion

The electrode surface treatment is performed before electroplating of MWCNTs and Au nanoparticles. This step is also found to be compulsory to ensure a successful electroplating process on silicon electrodes. The treatment process is completed through XeF_2 vapor etching (~ 2 seconds) in the reticle level. As a result, the original smooth silicon surface turns to porous, thus, creating enough roughness on silicon electrodes. The difference in surface morphology before and after the treatment is confirmed by the image taken from scanning electron microscope (SEM) and shows in Figure 5.2 (b) and (c).
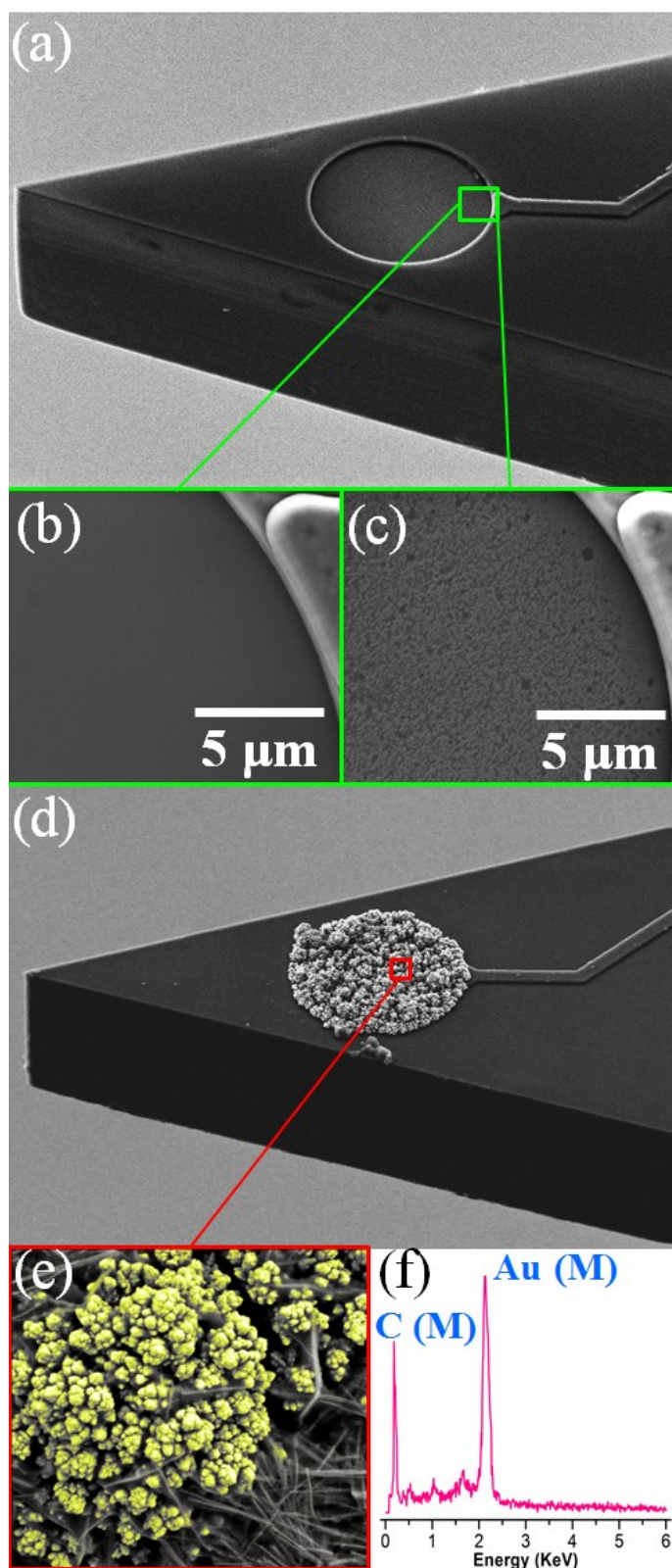
Figure 5. 2 SEMs of silicon electrode (a) and it surface topography before (b) and (c) after the surface treatment, (d) SEM of probe tip after composite coating, and (e) an inset of zoom-in view on electrode surface after composite coatings. Au nanoparticles are highlighted as yellow dots. (f) Plots of EDX result from coated electrode.

In the next step, the CNT and Au nanoparticle composite coating is applied from

an aqueous solution (2mg/mL) consisting of MWCNTs (Cheap Tubes Inc., length ~ 0.5-2 μm, outer diameter < 8 nm) mixed into an Au electrolyte bath (TSG-250, Transene) with applied sine wave pulses (amplitude 1.5 Vpp, 0.75 V DC offset, 50% duty cycle, 60 Sec). As shown in Figure 5.3, the cathode is connected to the silicon electrode and Au wire (diameter ~ 1 mm) is connected to the anode. With the assist of Au nanoparticles (Au ions) in the solution, both Au nanoparticles and Au encapsulated MWCNTs are deposited onto the surface of the electrode during the cathodic cycle.
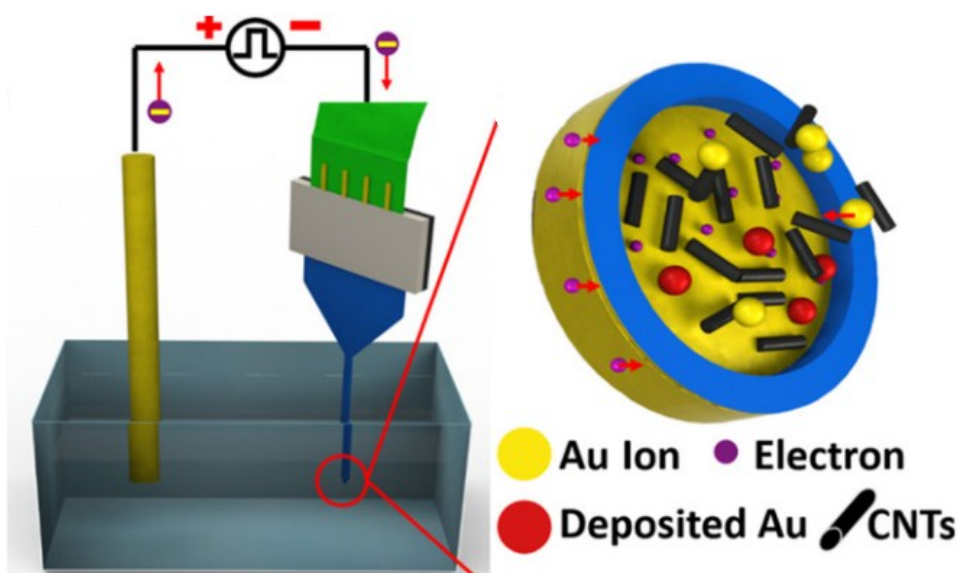
Figure 5. 3 Illustration for electroplating process. Both MWCNTs and Au-nanoparticles are mixed and deposited onto the electrode.

Figure 5.2 (d) shows the SEM of the electrode after electroplating process. MWCNTs and Au nanoparticle composites are electroplated only onto the electrically conductive region (highly doped silicon electrode) only without contaminations of rest areas. In addition, the enlargement of electrode geometry surface area (GSA) is well controlled to be less than 10% (< 55 μm in diameter) of its original size. Figure 5.2 (e) shows the surface morphology of the Au nanoparticles, which is highlighted as yellow globular dots with MWCNTs randomly orientated in fibrous shapes.

Energy-dispersive X-ray (EDX) analysis (Figure 5.2 (f)) confirms the presence of both Au and CNTs on coated electrodes. It is also worth noting that the original silicon electrode (without surface treatment) fails to be electroplated even with a higher biasing voltage (> 2 Vpp) during electroplating. Low surface roughnesses and a thin layer of surface native oxide could be reasonable explanations for such failures. Figure 5.4 (a) – (c) indicates the difference through the electroplating process. An obvious color change from (a) before to (b) after treatment is due to the partical exposure of the BOX layer beneath the silicon device layer.
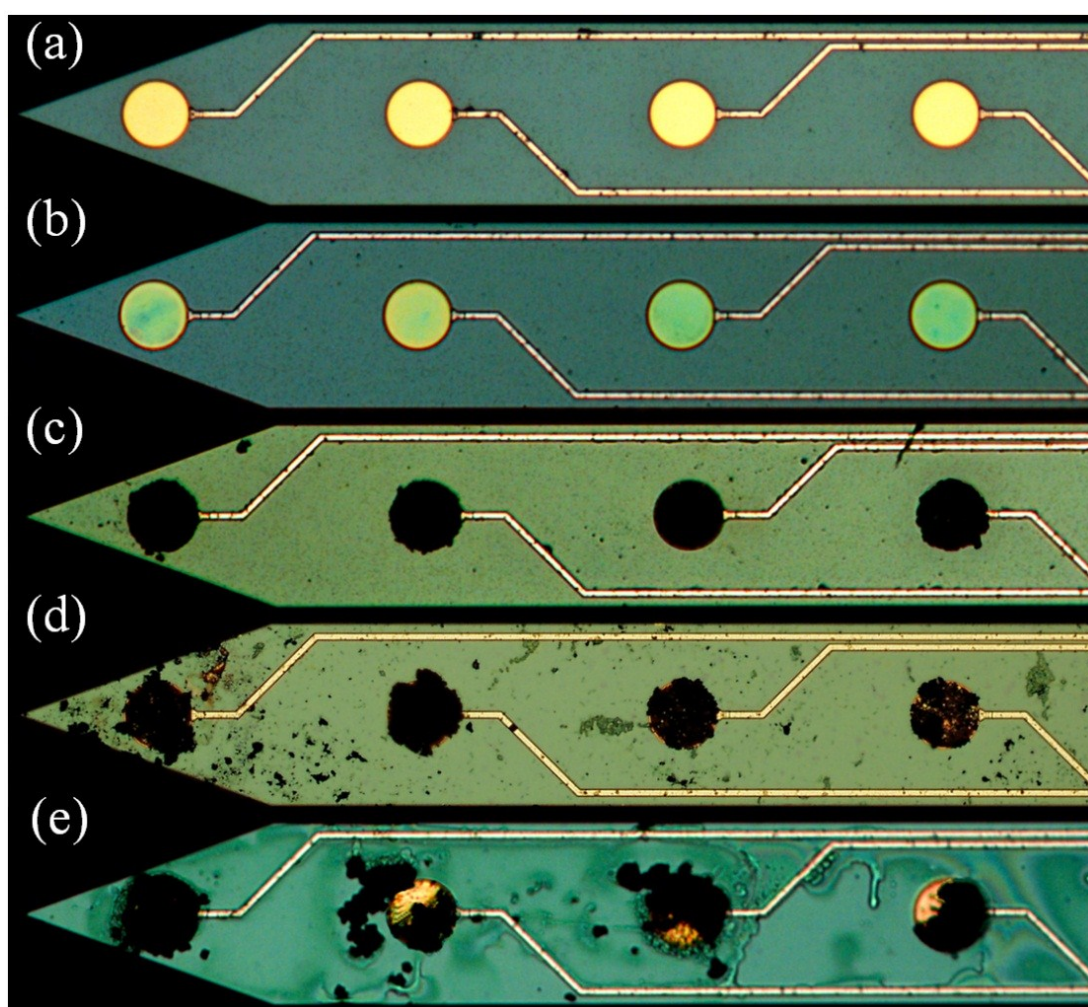
Figure 5. 4 The optical image of neural electrodes (a) before (b) after XeF_2 surface treatments; c) after composites coating; d) after 10 s shaking test in the ultrasonic tank; e) after twice implantation cycles in rat's brain.

To verify the adhesion, the composite coating on Si electrode survives after 10

seconds ultrasonic shaking conducted in ultrasonic cleaner (Branson B3510, 40 KHz, Max input power = 130 W) as shown in Figure 5.4 (d). Only partial delamination for three out of four electrodes is observed even after twice insertion into rat's brain as shown in Figure 5.4 (e) indicating a strong adhesion between the coating and the electrode. The detailed in vivo testing procedure and setups will be provided in chapter 5.3.1.

5.1.3 Electrochemical Impedance and Charge Storage Capacity

5.1.3.1 In vitro testing setup and improvement of interfacial impedance

Electrochemical impedance spectroscopy (EIS) is conduced to determine the interfacial impedcance of the electrode with and without coatings. Phosphate buffered saline (PBS, Biowest, pH 7.4, conductivity ×1) is used as the *in vitro* mediumu. The sinesold wave with amplitude of 50 mV and frequency spans from 100 kHz to 0.7 Hz is applied. The three-terminal-electrode setup is used in the experiment with Ag/AgCl electrode and Pt wire as reference and counter electrode respectively. The output impedance is recorded *in vitro* with an impedance analyzer (Autolab PGSTAT100N voltage potentiostat/galvanostat, Metrohm) and results are plotted in Figure 5.5. Impedances of smooth and porous surface silicon electrode at 1 KHz are recorded as 2.5 ± 0.4 MΩ and 0.9 ± 0.2 MΩ respectivley. The reduction impedance of the porous surface from the flat surface electrode is due to the increament of ESA [83]. Such impedance value can be catergorized in the same level as the result obtained from the equivalent GSA of Au electrode. After deposition of CNT and Au composites, the impedance of the electrode was further reduced with two orders (21 ± 3 KΩ).
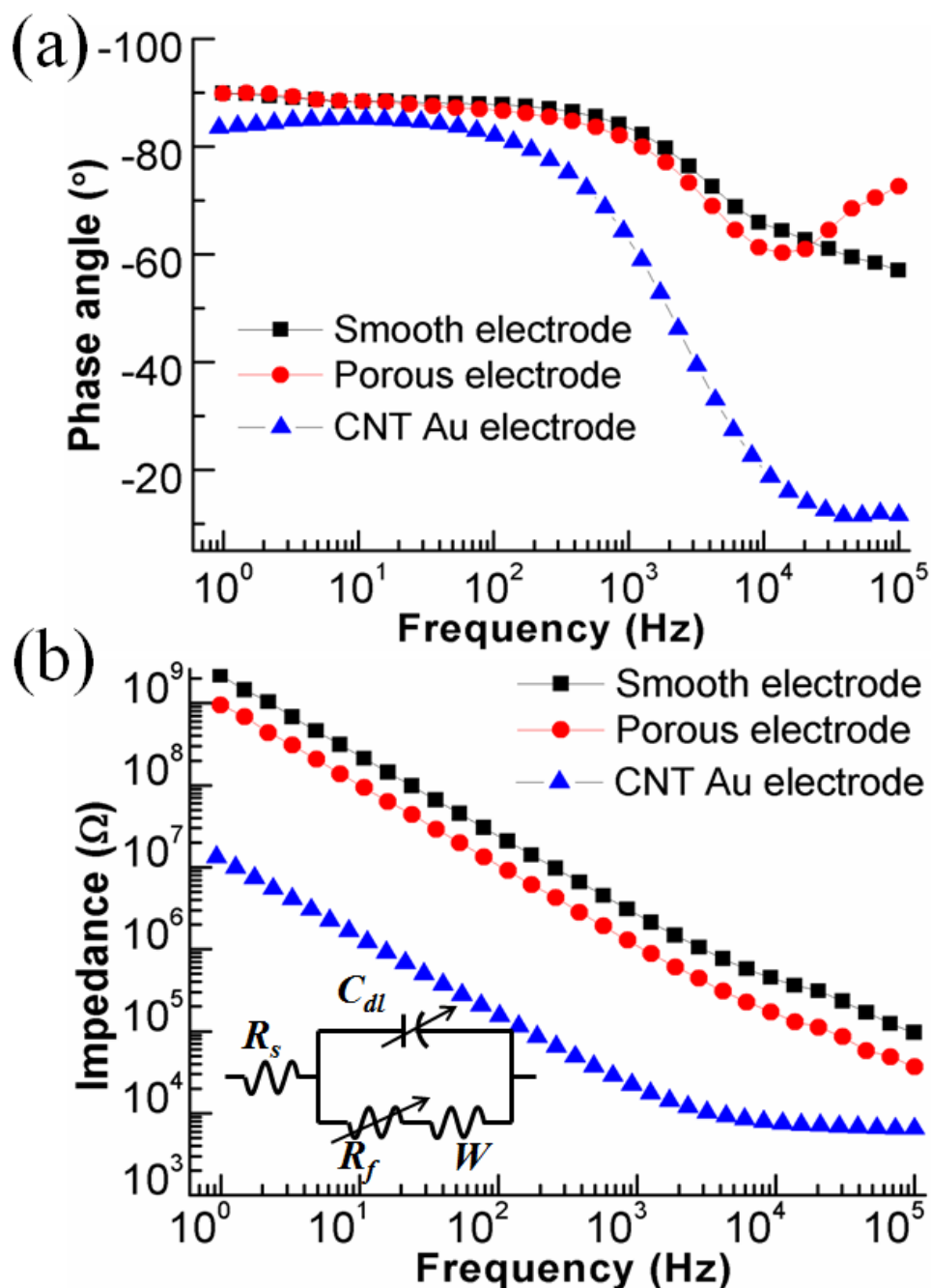
Figure 5. 5 Results from electrochemical impedance spectroscopy for (a) the plot of phase angle and (b) the plot of interfacial impedances for smooth, porous and CNTs & Au nanoparticles coated silicon electrodes. The inset shows Randles equivalent circuit.

The drastic decrease of the interfacial impedance is credited by the high porosity of surface coatings contributed from both CNTs and Au nanoparticles. Such highly porous electrode surface is essential for the large ESA and the resultant huge amount of charge accumulations between electrode-electrolyte interfaces. It has been reported

that the specific surface area of plasma treated MWCNTs is up to 400 $m^2 g^{-1}$ [190]. As a result, the larger amount of charge can be accumulated on CNTs external surfaces than the amount of charge on the traditional planar electrode. In addition, the larger ESA also provides higher electrolyte accessibility over the planar surface electrode. Moreover, it has been proposed that ions can be squeezed into the inner cavity of nanotubes, if the tube has an opening tip. With a small inner diameter of CNTs (<8 nm in our case), the distance (γ) between tube internal surface and the maximum charge density of electrolyte ions would be deduced. Thus, according to $C=\eta A/\gamma$ (where C is capacitance, η is permittivity of the electrolyte, and A is the ESA between electrode and electrolyte), a further increment in total capacitance. In addition, the superior electrical conductivity of Au nanoparticles has been reported by using Layer-by-layer assembly method [137]. Thus, the combination of both CNT and Au nanoparticle will take full advantages of low interfacial impedance (due to higher volume ion transportations) and high electrical conductivity from MWCNTs and Au nanoparticles.

To further interpret the improvement of CSC quantitatively, the Randles equivalent circuit (illustrated in the inset of Figure 5.5 (b)) is introduced and changes in double-layer capacitance are analyzed as below.

5.1.3.2 Randles equivalent circuit

In a simple case, Randles circuit consists of a double-layer capacitor (C_{dl}) in parallel with the series combination of a charge-transfer resistance or Faradaic resistance (R_f) and Warburg impedance (W). When a potential is applied through the measurement system, another series resistance (R_s), which includes the solution resistance (between the working and reference electrodes) plus the electrical resistance of testing electrodes, is added into the circuit as well. The Warburg

impedance is generally negligible at high frequencies. The time interval is too short to be sufficient for the ion diffusion reacted on the electrode surface [191]. Thus, the expression of total impedance can be simplified as:

$$Z(\theta) = R_s + \frac{R_f}{1 + j\omega R_f C_{dl}} = Z^{'}(\theta) + Z^{''}(\theta) \tag{5.1}$$

Where θ is the angular frequency, $Z^{'}$ is the real part of total impedance and $Z^{''}$ is the imaginary part of total impedance. The series resistance (R_s) approximates to the value of total impedance (Z) as the frequency (f) tends to be very high ($f \rightarrow \infty$). Under such assumption, R_f and C_{dl} of at each frequency can be determined by [190]:

$$R_f(\theta) = \frac{Z^{''2} + (Z^{'} - R_s)^2}{Z^{'} - R_s} \tag{5.2}$$

$$C_{dl}(\theta) = -\frac{Z^{''}}{\theta[(Z^{'} - R_s)^2 + Z^{''2}]} \tag{5.3}$$

Assuming the working electrode is placed within 5mm radius from the reference electrode and the conductivity of PBS is specified as $14000 \sim 17800$ μmhos/cm. Thus, series resistances of both smooth and porous silicon electrodes can be assumed to equal to their electrical resistances due to the negligibly small solution resistances (in the range of few tens of Ohms). After the measurement of testing structures, the electrical resistance before coating of composite is around $1 \sim 1.5$ KΩ. After deposition of CNTs and Au composites, the estimated series resistance is around 6.5 KΩ based on the observation from EIS plotted in Figure 5.5 (b). Angular information can be obtained from the plot of phase changes in Figure 5.5 (a). As results, information on double-layer capacitance and faradaic resistance changes at 1 KHz before and after composite depositions is summarized in Table 5.1 according to equation (5.2)-(5.3). Based on information provided in Table 5.1, the significant improvement in interfacial impedances is contributed from the combination of an

increment of double layer capacitances (C_{dl}) and a decrement in faradaic resistances (R_f). This interpretation also stands for the improvement of silicon electrode after surface treatments over the smooth surface counterpart.

Table 5. 1 Parameters extracted from the Randles equivalent circuit based on Si electrodes with different cases of surface conditions.

P-doped silicon electrodes	R_s (KΩ)	R_f (MΩ)	C_{dl} (µF)
Before treatment	~ 1	~ 62	~ 0.7
After treatment	~ 1.5	~ 4	~ 1.1
After coating	~ 6.5	~ 0.14	~ 46.7

5.1.3.3 Cyclic voltammetry (CV) test
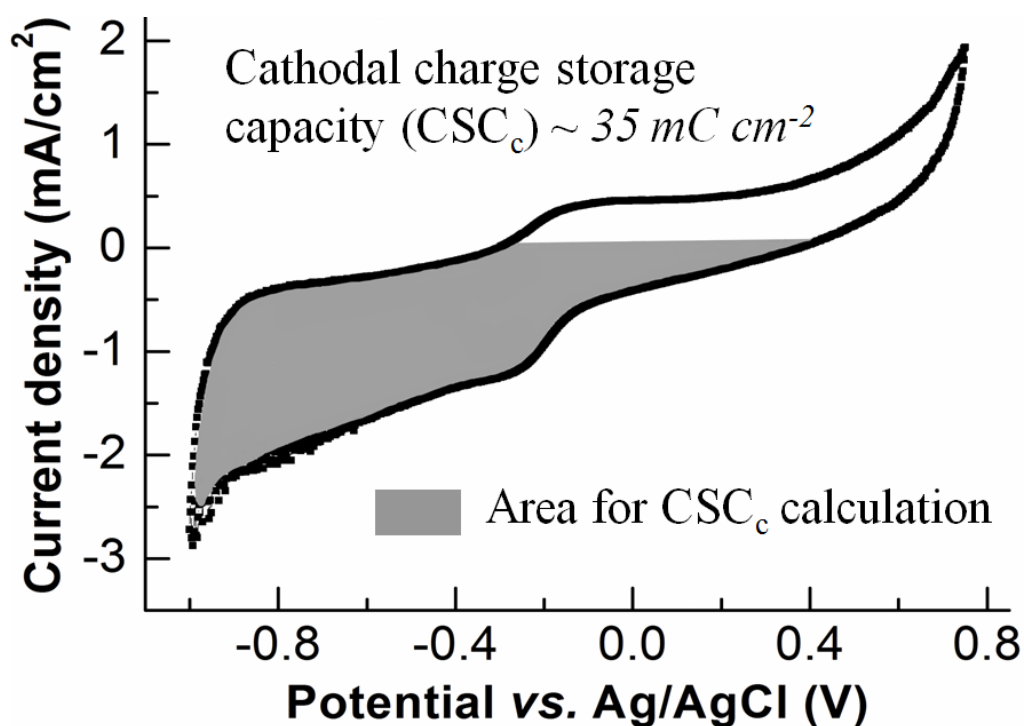
Figure 5. 6 Cyclic voltammetry plot of the silicon electrode after coating with MWCNTs plus Au nanoparticles.

Using the same testing setup, the charge storage capacity (CSC) of electrodes after composite coating is evaluated by the cyclic voltammetry (CV) under a sweep rate of 50 mV s^{-1}. The resulting CV curve is plotted in Figure 5.6 and the electrolysis

window is very similar to the literature [185]. Accroding to our tests, oxygen and hydrogen evolve at +0.75 and -1 V (*vs*. Aug/AgCl) respectively. There are small peaks at about -0.25 V, which is most likely contributed by the reduction of absorbed oxygen [140]. In addition, the relatively featureless CV window suggests that silicon electrodes after coating composites exhibit charging and discharging behaviors with the presensce of only double-layer capacitance instead of faradic reactions. This pure capacitive charge transfering mechanisum implies a safer working range without introducing irreversible electrochemical reactions [83]. The cathodal charge storage capacity (CSC_c) is calcualted from the time intergral of the cathodic current in CV over a potential range just within water electrolysis window. The CSC_c of the highly doped silicon electrode after MWCNTs and Au nanoparitcles coating is around 35 mC cm^{-2}, which is higher than the CSC_c reported from IrO_x film [140] and in the equivalent range to some results reported on other conductive material composites (e.g. PEDOT/MWCNT composites) [188]. The actual neural recording capability will be further discussed in chapter 5.3.

5.2 SiNWs Based Built-in Strain Sensor

Before conducting *in vivo* probe implantation, we will explain the fundamental difference between the integrated strain sensor and the external load cell based on the extracted buckling information from both cases.

5.2.1 Setup of Mechanical Buckling Test

To verify the performance of on-probe strain sensor, the probe buckling test is firstly conducted on the load frame structure using Instron MicroTester (Instron 5848, USA). A load cell (Instron 2530-439; Maximum loading: ± 5N, Resolution < 0.25%

of reading over static rating) is connected in series with the specimen (i.e. SiNWs neural probe) and converts forces into an electrical signal for the control system (Bullhill console) to measure and display both displacements and loadings simultaneously. To conduct the test, the probe is fixed in the metal grip (with the tip facing towards the movable actuator) between a movable actuator and the stationary load cell, which is mounted to the rigid load frame. The movable actuator moves the attached stainless steel cylindrical probe downwards perpendicularly to the tip of SiNWs probe. As a result, the probe starts buckling till its complete fracture. The displacement resolution of the actuator is down to micrometer per second. Meanwhile, the strain information is transferred and recorded as voltage outputs by using National Instruments (NI) data acquisition system (NI USB-6363 and Labview 2013). The testing is conducted under room temperature (25 °C) and a DC supply voltage of 1 V

5.2.2 Result and Discussion

The physical geometry of probe has large influences on its buckling and insertion behaviors. We first start buckling tests of silicon probes with equal length (3 mm) but different shank base design (see Figure 5.1 (a) & (b) for structure *I, II & III*). Figure 5.7 (a) to (c) show mechanical buckling results of SiNWs probe for design *I* to *III*, respectively. Red and blue curves show the changes of output voltage recorded from SiNWs strain sensors located at base and middle of the shank, respective. Readings (including both buckling force and displacement) from the load cell (Instron 2530-439) are presented in purple curves.
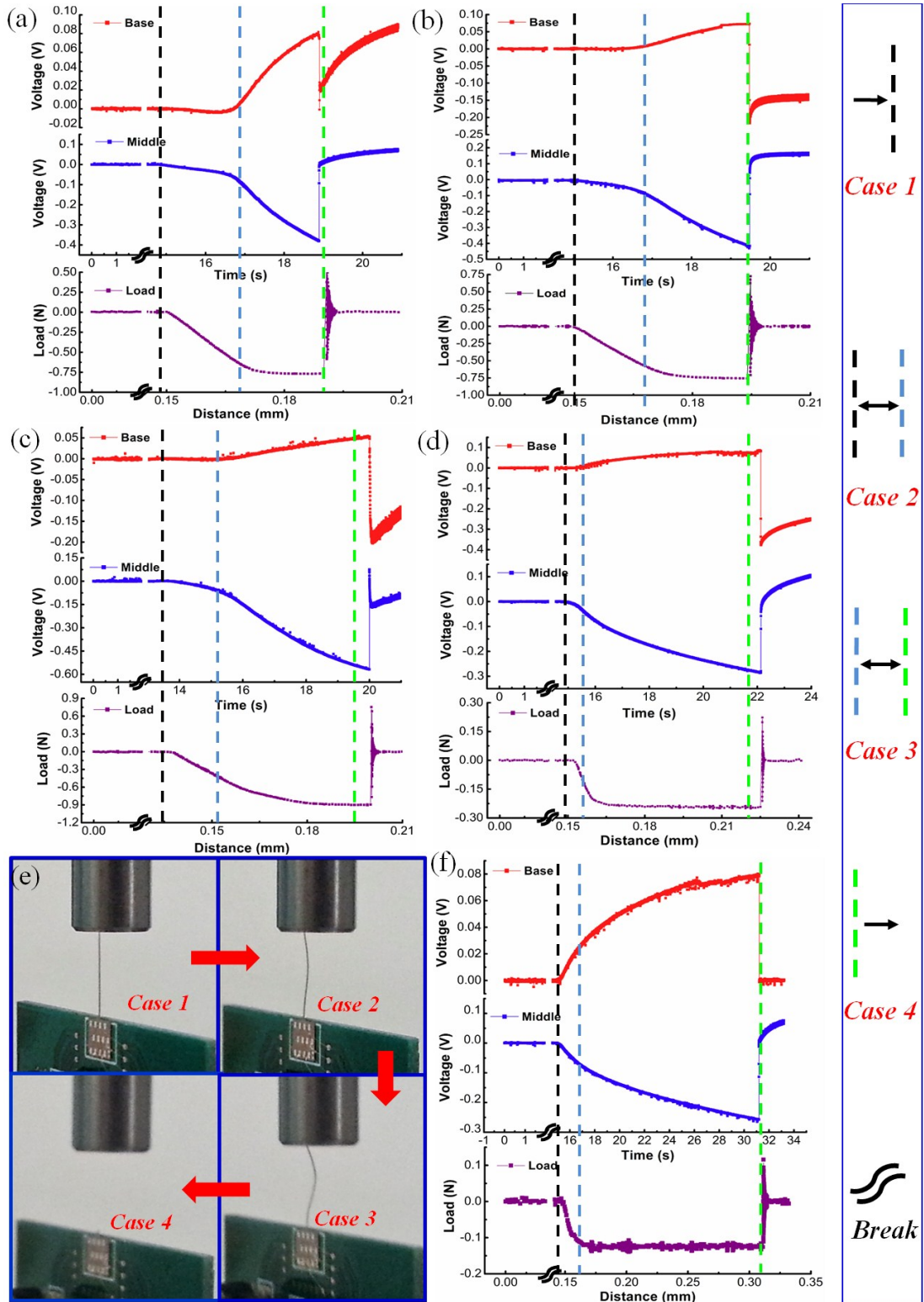
Figure 5. 7 Buckling tests of the probe with fixed probe length (3 mm) for (a) design *I*; (b) design *II*; (c) design *II;* and with fixed shank structure (design *II*) for different probe length of (d) 5 mm; (f) 7 mm. (e) shows snapshots of the probe under different *cases (1-4)* of buckling mechanics. The definition of the mechanical period under each *case* is depicted on the left side of the figure (highlighted with the blue box).

Before the cylindrical fixture in contact with probe tip (*case 1*), all reading

remains at their baseline. Right after the moment of contact between probes tip and fixture, the output from SiNWs strain sensors (both in base and middle of shank) and load cell smoothly change with the movement of cylindrical fixture (*case 2*). The relationship between buckling induced stress and strain is relatively linear and can be characterized by a constant factor (i.e. young's modules of the material) [154]. After load exceeding the critical buckling force (*case 3*), however, this linear relationship is no longer valid. Due to the presence of the torsion mechanism under large buckling, the reading from load cell tends to be saturated even with a continuous external loading applied in cases of all three different shank designs. On the other hand, outputs of strain changes keep varying with the increasing external load till the probe breakage (*case 4*). Such non-linear relationship between applied loads and strain changes under a large buckling force is similar to the mechanical behavior a silicon rod [155]. Hence, it is reasonable to monitoring the strain changes along the probe instead of loading forces in vertical direction. According to the literature [14] and our previous findings on piezoresistance effect of SiNWs under large strain changes [192], gauge factor of P-doped SiNWs in <110> direction can be above 90 [164]. That value is at least doubled when compared to the result from polysilicon piezoresistors, thus, a better sensitivity of using SiNWs.

To further explore the functionality of SiNWs strain sensors, buckling tests on probes with the same base structure (design *II* as defined in of Figure 5.1 (b)) but various lengths (i.e. 3 mm, 5 mm and 7 mm) are also carried out and the results are plotted in Figure 5.7 (b), (d) and (f). The phenomenon of the load cell reading saturation is even obvious for longer silicon probes. It can be concluded by the relationship between the maximum load/force (*P*) required to buckle the shank and other parameters related to probe geometry [156]:

$$P = \frac{Ewt^3\pi^2}{6l^2} \qquad (5.4)$$

Where w is the width, t is the thickness, l is the length and E is the Young's modulus. With fixed other geometric parameters, the longer probe results in a lower buckling force. It is also worth noting that voltage outputs from two SiNWs strain sensors change in opposite polarities, especially after external loads exceeding critical buckling forces. For the strain sensor at the base of shank (red plots in Figure 5.7), the increment of output voltage can be explained by increasing resistance for SiNWs placed longitudinally (along X direction as defined in Figure 5.1 (c)), meanwhile, decreasing resistance for SiNWs aligned transversely (along Y direction as defined in Figure 5.1 (c)). Such resistance changes match the behavior of SiNWs (configured in full bridge structure) under a tensile strain. Specifically, probe shank bends towards to the device surface (Z direction as defined in Figure 5.1 (c)). On the contrary, decreases of output voltage suggest that SiNWs suffer a compressive strain at the middle of the probe. Hence, the probe shank bends downwards to the device surface (opposite to Z direction as defined in Figure 5.1 (c)). Such extracted strain information matches captured probe mechanical behaviors as shown in Figure 5.7 (e). As results, probe bending mechanics can be precisely described based on the localized strain information.

5.3 *In vivo* Experiment

In this section, silicon neural probe are inserted into the rat's brain to verify its functionality of both brain signal recording and mechanical response during implantation.

5.3.1 Procedures for in vivo neural recording and probe implantation

Male Sprague Dawley rats (Weight: 300 ~ 330 g) are anesthetized with pentobarbital sodium (~50 mg/Kg) and immobilized in a stereotaxic apparatus. A supplementary dose around 8~10 mg/Kg per hour is continuously injected to keep the animal under anesthesia. The craniotomy is performed posterior to lambda landmark and a stainless steel screw is also inserted as the reference electrode. The grounding electrode is connected to the tail. Another two craniotomies are carried at dersal hippocampus CA1 region (2.0 mm lateral and 2.3 mm posterior to the bregma landmark) and somatosensory S1 region (2.5 mm lateral and 0.8 mm posterior to the bregma landmark), respectively. Please refer to Figure 5.8 for the detailed location of each region. CA1 is used for acute neuron signal recordings and S1 is only for probe insertion purpose (monitoring mechanical behaviors). As shown in Figure 5.8 (c), the probe is attached on the PCB and wire-bonded for electrical communications to NI data acquisition systems. Movements of the PCB in a vertical direction are manually controlled by the micromanipulator right on top of rat brain (e.g. CA1 or S1 regions) as demonstrated in Figure 5.8 (a). For neural recordings, brain signals are collected and amplified by RZ5D BioAmp Processor (Tucker-Davis Technologies, US). The insertion speed ranges from 0.1 to 1 mm/s for understanding insertion mechanics or neural recording purposes. The final insertion depth is around 2.5 mm for probe implanted at both CA1 and S1 regions. Figure 5.8 (c) displays *in vivo* testing setups with an inset showing a SiNWs probe after packaging. All testing procedures are performed under protocol 095/12(A3)13 and approved by the Institutional Animal Care and Use Committee at National University of Singapore. The rat is euthanized by overdose of CO_2 at the end of experiment.
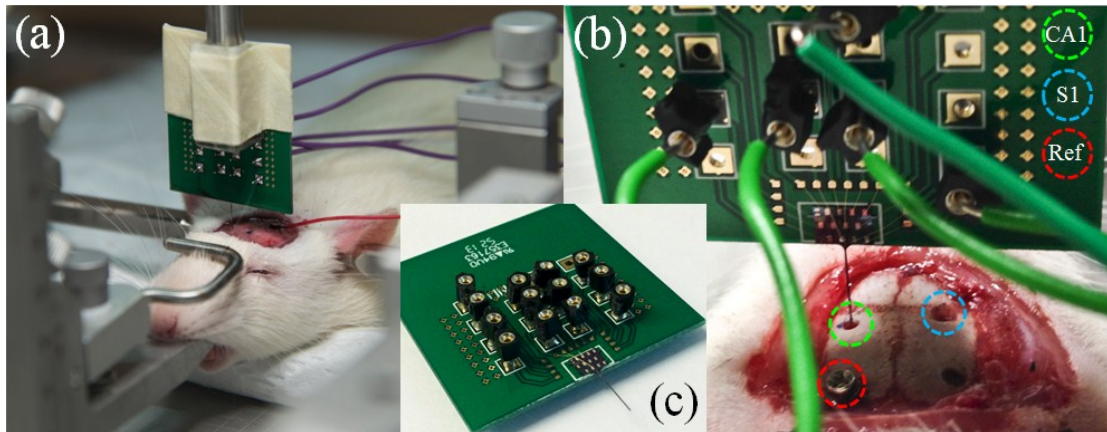
Figure 5. 8 (a) *in vivo* testing setup for probe implantation, (b) a picture of craniotomy on different brain regions, (c) an image of the probe after packaged on PCB.

5.3.2 *In vivo* Neuron Signal Recording
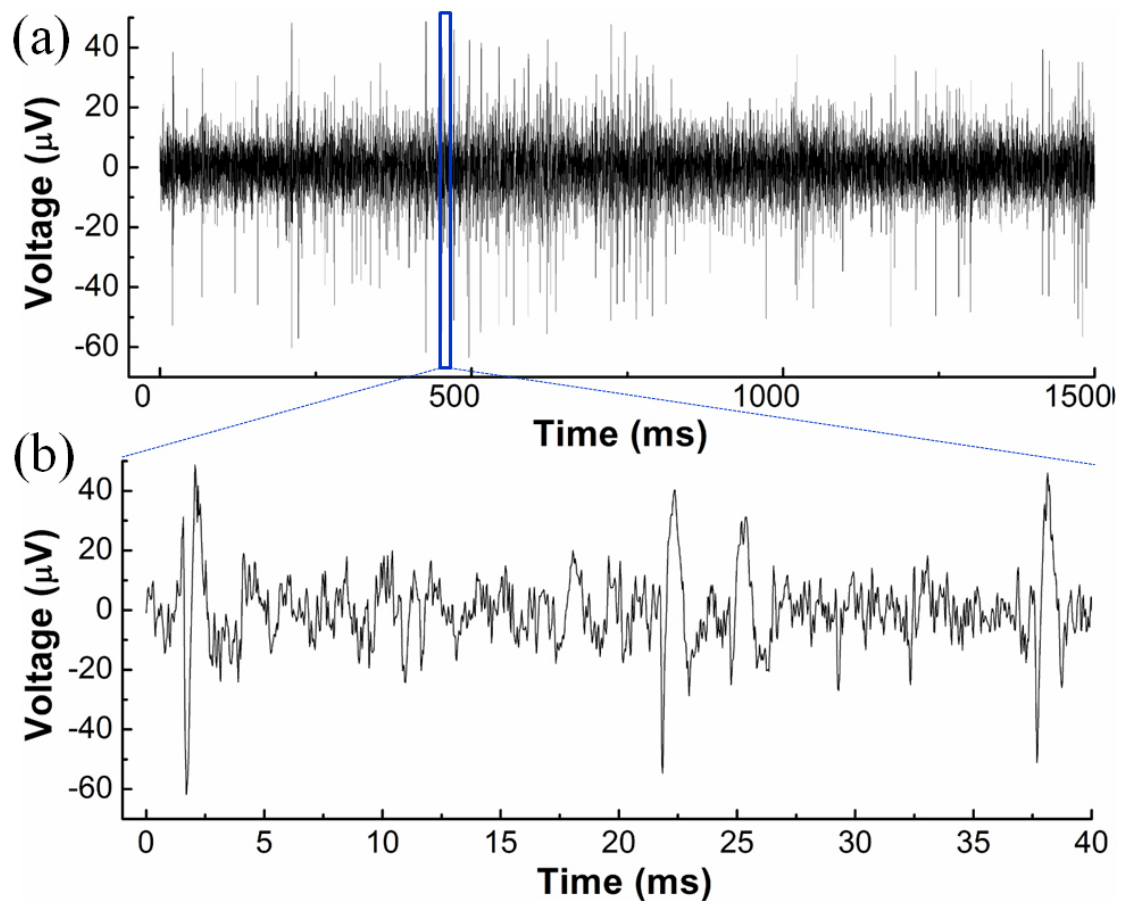
Figure 5. 9 Plots of recorded brain neural signals with periods of (a) 1.5 s and (b) 40 ms (a zoom-in window) from CA 1 region.

The *in vivo* recording capability of silicon electrode after composite coating is

tested. Figure 5.9 (a) illustrates a 1.5 seconds segment (the top plot) and a 40 ms zoom-in view (the bottom plot) from the continuous recordings. It has been reported that the action potential of Central Nerve System (CNS) is typically in the order of 100 µV, however, the signal strength may vary and be very subject to the proximity between electrode and the active neuron, thus, smaller amplitude of action potential is often detected [140]. Beside the signal amplitude, the background noise level is usually taken to quality the recording performance of electrodes. In our measurement results, it is also worth noting that noise level is well controlled below 20 µV, which is identical to the level reported from the electrode coated with other high charge composites (e.g. PEDOT/MWCNT) [136].

5.3.3 Probe *in vivo* implantation mechanics

Insertion behaviors of the probe are recorded in Figure 5.10. Blue and red plots represent signals recorded from SiNWs strain sensors embedded at the middle and base of the shank. As shown in Figure 5.10 (a), clear output glitches (highlighted with red dash box) indicate that probe is in contact with the brain tissue surface. Sequentially, the baseline voltage level gradually increases and decreases with the peak value occurring 10s after the moment of the contact. This explains that the moment of actual penetration into brain tissue happens after the maximum tissue dimpling around 1mm (insertion speed of 100 µm/s).
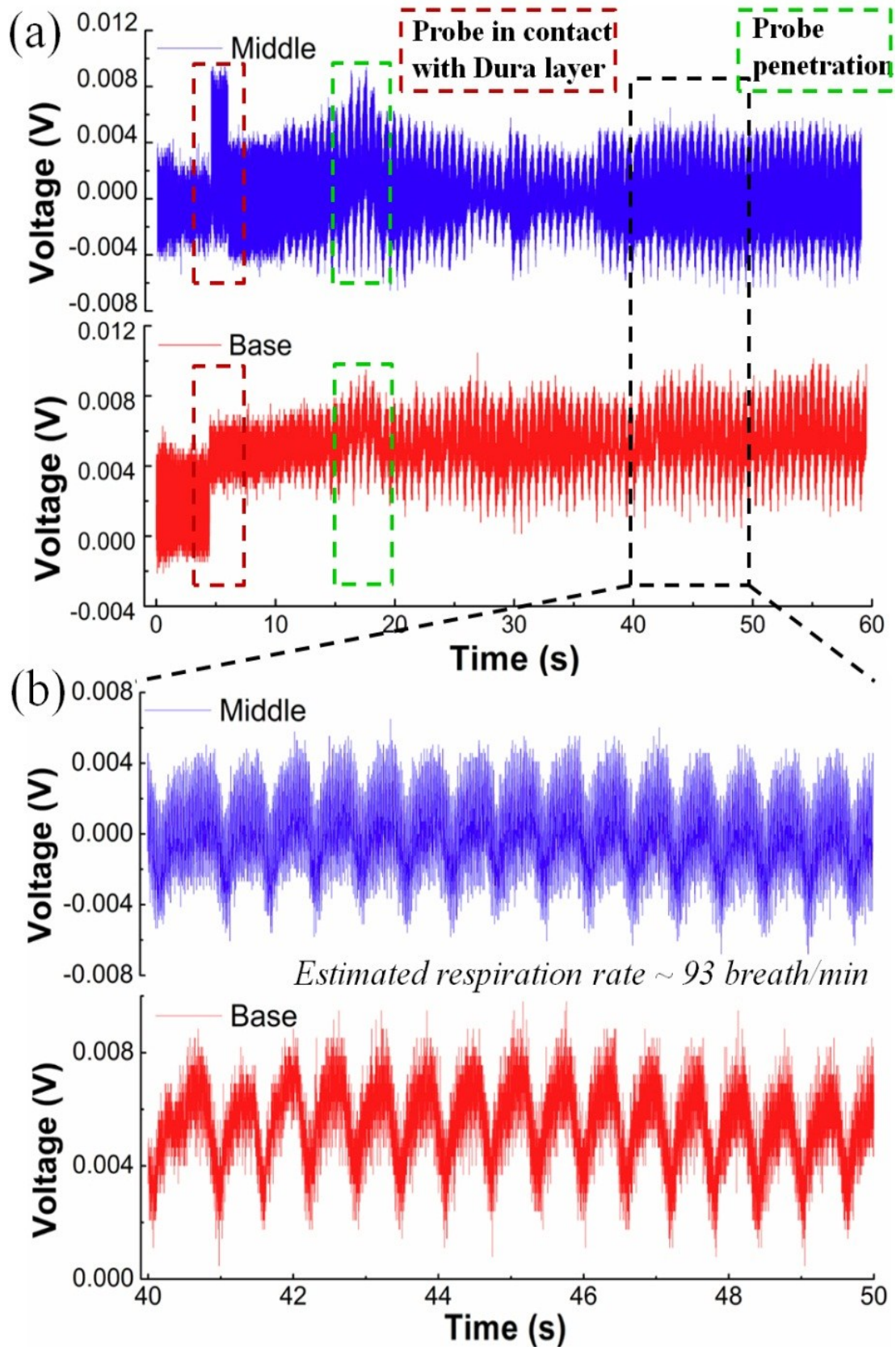
Figure 5. 10 (a) Plot of outputs from SiNWs strain sensors during *in vivo* probe insertions into rat's brain; (b) a highlighted zoom-in period with spans of 10s.
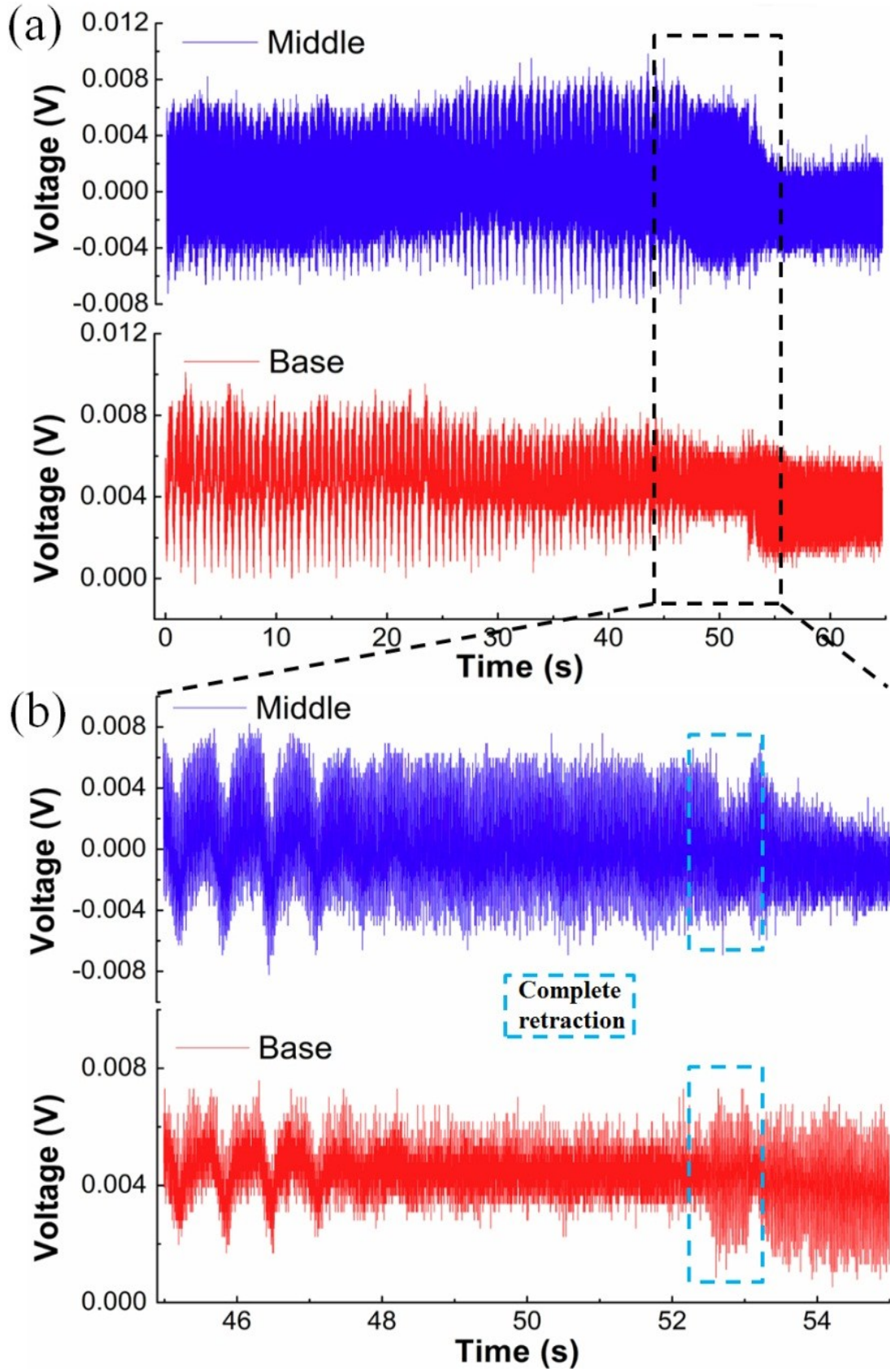
Figure 5. 11 (a) Plot of outputs from SiNWs strain sensors during *in vivo* probe retractions from rat's brain; (b) a highlighted zoom-in period with spans of 10s.

The vertical movement of the probe stops at the point of 30 s and the estimated insertion depth is around 2.5mm. A zoom-in view (period of 10 s as indicated by the black dash box) is provided in Figure 5.10 (b) after 10s interval for tissue relaxations. According to the literature [193], the cycling spike signal is generated by the lateral micro-motion, which is possibly correlated to the respiratory behavior of the testing subject under different stage of anesthesia. Therefore, information about the extent of anesthesia of test subject can be possibly deduced from status of its respiration rate (~ 93 breath/min in our case). Since our primary goal is the demonstration of the probe *in vivo* behavior, the detailed time to time correlation between actual rat respirations and the micro-motions is not covered here.

The output information on the probe retraction is depicted in Figure 5.11 (a) with a zoom-in period of 10s (Figure 5.11 (b)) for a better view. The retraction speed is as low as 10 μm/s to ensure a complete tissue relaxation, so that the clearer understanding of retraction mechanics. Retraction processes can be monitored through the presence of cycling spikes, which disappear slightly before the probe moving out of brain surface. In addition, obvious glitches appear in plots of signals recorded from both the middle and base of shank at the moment of a complete probe retraction.

5.4 Conclusions

In this chapter, we have proposed a MEMS silicon neural electrode probe fabricated with CMOS-compatible process. By leveraging the fabrication compatibility and different doping profiles, both the neural electrodes and on-chip strain sensors are realized using the single crystal silicon layer on an individual shank. The quality for the interfacial impedance of highly P-doped silicon neural electrodes is verified through electrochemical impedance spectroscopy and *in vivo* neural

recording in rat. With additional electroplated nano-composite coatings, the noise level is properly contained (< 20 µV) during the *in vivo* neural recording. Meanwhile, SiNWs configured in full bridge structures are embedded at the middle and base of the shank for localized strain sensing. The experimental buckling study explores the substantial difference in measurements of probe deformation between use of the external load cell and the integrated strain sensor. Intrinsic relationships of deformations and stain changes help in revealing the complete buckling mechanics of silicon probe till the complete fracture. With the superior sensitivity and a better noise immunity of SiNWs based bridge structures, further extracted strain signals from *in vivo* study helps the precise probe manipulation and provides the subject anesthetic information demanded by practical clinic studies.

Chapter 6   Conclusions and Future Works

6.1 Summary of Current Works

We have described the fabrication of nanowires and its application in various fields, e.g. Cantilever shaped air flow sensor, Grooved diaphragm pressure for a low pressure sensing, and the integrated strain sensor in the thesis. The general fabrication process is beneficial to all kinds of the design with embedded SiNWs as piezoresistor. To ensure a good piezoresistance effect and minimize the non-linearity factor contributed by SiNW itself, the proper optimization of implantation dosage is firstly discussed. With the selective options on passivation layer and the residual stress issue has been addressed. However, such option is very subjective to the specific application environment. In addition to the fabrication parameters, the detailed device structure design is substantial to the performance of the final NEMS sensor.

In the flow sensor design, beside the intrinsic advantage of SiNWs based piezoresistor, a nearly uniform pressure under laminar air flow is intentionally designed with a proper flow channel length and diameter. Therefore, a reasonable assumption on air flow development is addressed for the possibility to conduct device characterization with a less complicated setup. Benefiting by the sample mechanical structure, the gauge factor is also successfully extracted and tallies with the literature.

As the extension from the previous flat diaphragm pressure sensor [164], the SiNWs embedded pressure sensor is firstly equipped for a low pressure sensing (0 – 120mmHg). Although some parameters (e.g. the exact location of SiNWs for the maximum induced strain, total diaphragm thickness) have not been optimized yet, the proposed device with the proof-of-concept annular groove structures demonstrates the

sensitivity improvement by more than 17 times (compared with the literature) with a simplified fabrication process. The dynamic response of both sensor linearity and sensitivity indicates the monotonously relationship of the sensor performance with respect to temperature changes.

After increasing the dosage of implantation from 1×10^{14} cm^{-2} to 4×10^{15} cm^{-2}, the thin layer (< 100nm) of single crystalline silicon has been demonstrated as the interfacial electrode for neuron signal recordings. Such monolithic fabrication process facilitates the possibility of direct on-chip IC integration. Additionally, the SiNWs connected in full bridge structure is also leveraged to collect the localized strain information caused by mechanical impact between probe and tissue, for instance, detection of probe insertion and retraction behavior, even monitoring the respiration of surgical subject.

We have explored the feasibility of using SiNWs in various applications with an obvious improvement compared with reported conventional piezoresistive counterpart. For future development of the SiNWs based NEMS sensor, the new device design should be introduced with a revolutionary fabrication/structure breakthrough based on current accumulated experience. We hereby propose some suggestions with possible enhancements for future SiNWs based NEMS design.

6.2 Future development of SiNWs embedded NEMS devices

6.2.1 Dual Sensing Range Diaphragm Pressure Sensor

We have discussed the pressure sensor for the low pressure application in chapter 4. For such device, the suggested measurement range spans from 0 to 120 mmHg. As the prototype design, it generally provides the optimum performance between a good sensing resolution and wider sensing region. Nevertheless, both sensing specifics

seem less versatile for the different application. For blood pressure measurement, the practical reading may be up to 200 mmHg depending on the stage of hypertension. It would be challenging for the reported device to work at 200 mmHg still with an acceptable linearity. In another case, for intracranial pressure (ICP) monitoring, the normal pressure reading range is in 7 – 15 mmHg and it is necessary to differentiate the ICP level with a difference as small as 1 mmHg. Therefore, the single pressure sensing device with a vast sensing range for versatile applications would be highly desirable for the consumer market. In addition, how uniform of the sensing performance over the entire wafer would be vitally important for the industry commercialization. An alternative fabrication flow needs to be attempted rather than the traditional backside DRIE. For instance, the frontside isotropic etching as suggested in chapter 2.4.2. With a proper trench protection, the diaphragm can released without an over-etching, thus, a less performance deviation cross the wafer. However, the non-optimized releasing-hole design may sabotage the structure of the final device. After isotropic etching, an example of the significant initial diaphragm deflection is observed and shown in Figure 6.1.
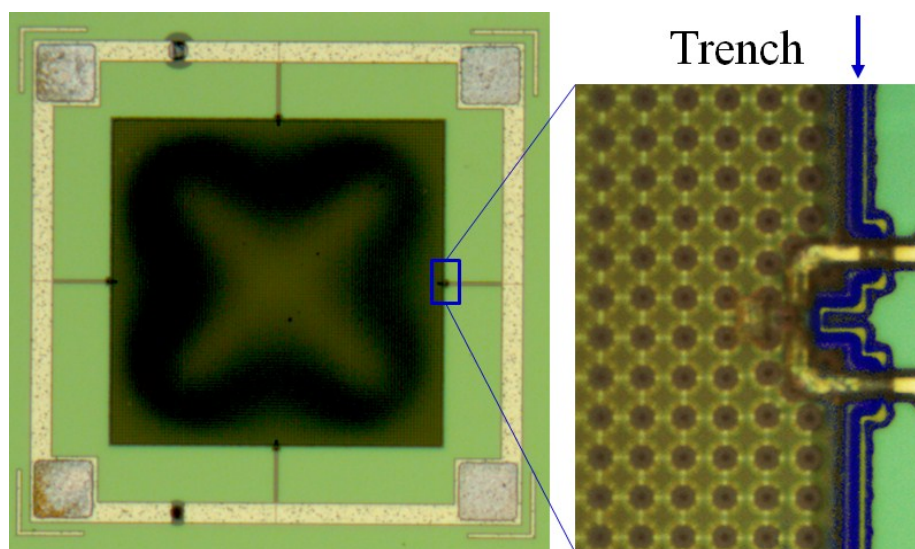
Figure 6. 1 Optical images of the star shaped released diaphragm (400×400 μm^2) with a zoom-in photo on diaphragm edge. The trench is highlighted with blue color.

In this particular design, the 1μm (diameter) released hole of with pitch of 1μm is patterned on the diaphragm. The mechanical stiffness has been greatly reduced with the resultant mesh structured diaphragm in comparison to the original solid diaphragm. In addition, the thickness of passivation Si_3N_4 is decreased to 1μm rather than 2.5μm applied in previous flat diaphragm design. Therefore, the residual stress is no longer balanced and leads to a star shaped diaphragm structure after release.
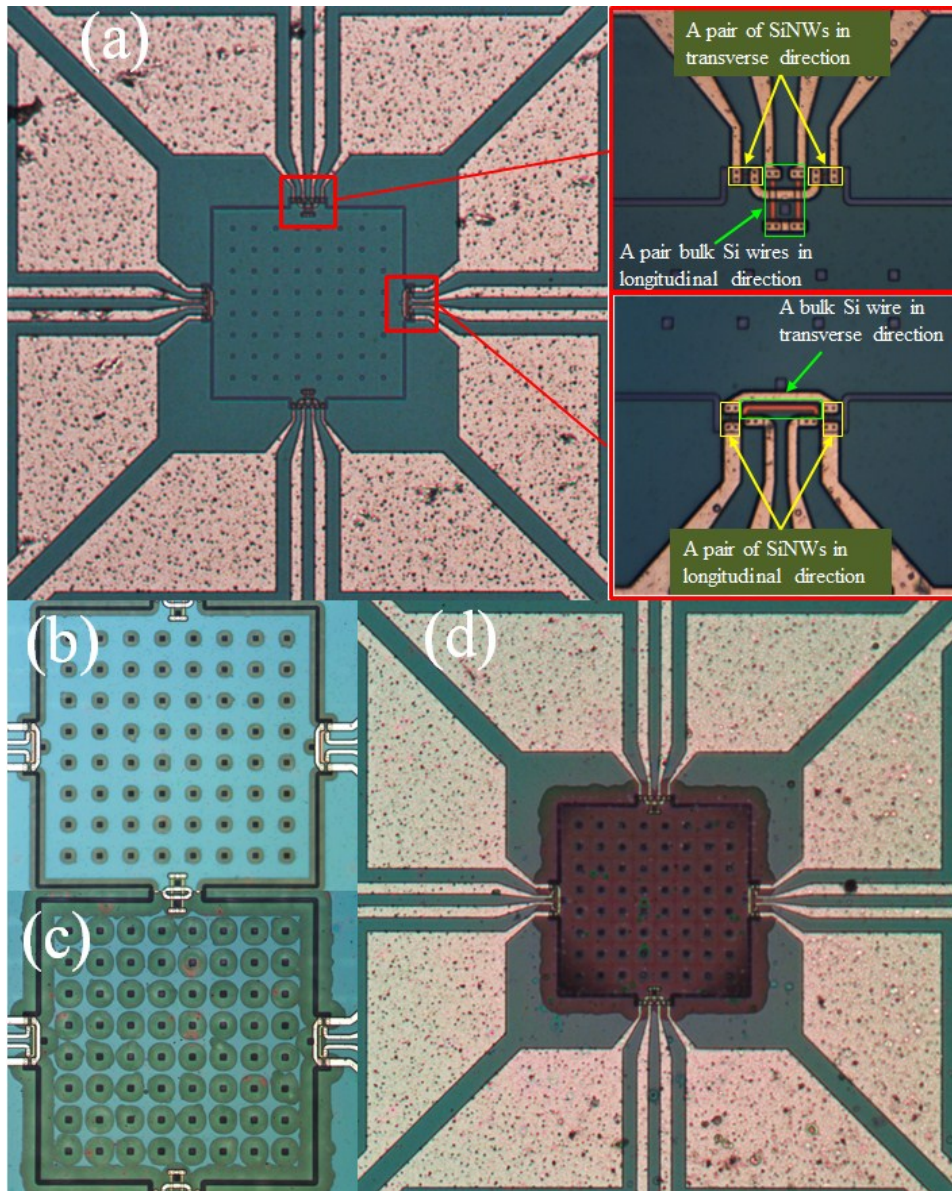
Figure 6. 2 Optical images of the dual sensing range pressure sensor released through a pure frontside releasing process. (a) The diaphragm before XeF_2 etching, (b) after 1 min XeF_2 etching, (c) after 3 mins XeF_2 etching, and (d) after 6 mins XeF_2 etching.

Without increasing the passivation layer thickness, both size and pitch of releasing-hole has to be re-adjusted to maintain a rather stiff pressure diaphragm. The new proposed square diaphragm (sensing area ~ 200 × 200 µm²) pressure sensor has been fabricated and its optical images are given in Figure 6.2. The size of releasing-hole is increased to 3 × 3 µm² with the pitch of 20µm. To quickly verify the new design and reduce the fabrication complexity, the trench structure is not included in this batch. Figure 6.2 (a) – (d) shows the releasing process and the severe diaphragm buckling issue has no longer been observed as indicated in Figure 6.2 (d).

In order to sense a low pressure range (e.g. 0 – 25 mmHg) with a good resolution, 4 pairs of 1µm SiNWs are placed right at the diaphragm edge, whereas, another 4 pairs of 10µm bulk silicon wires are used for the large pressure sensing (e.g. 0 – 200 mmHg). It has been demonstrated in chapter 3 that SiNWs based piezoresistance maintains a relatively good linearity with the percentage changes (∆R/R %) less than 15%, if other mechanical factors are excluded. Hence, we try to keep the percentage of SiNWs resistance within 15% for two different sensing ranges, e.g., 0 – 25 mmHg (ICP pressure) and 0 – 200 mmHg (blood pressure).
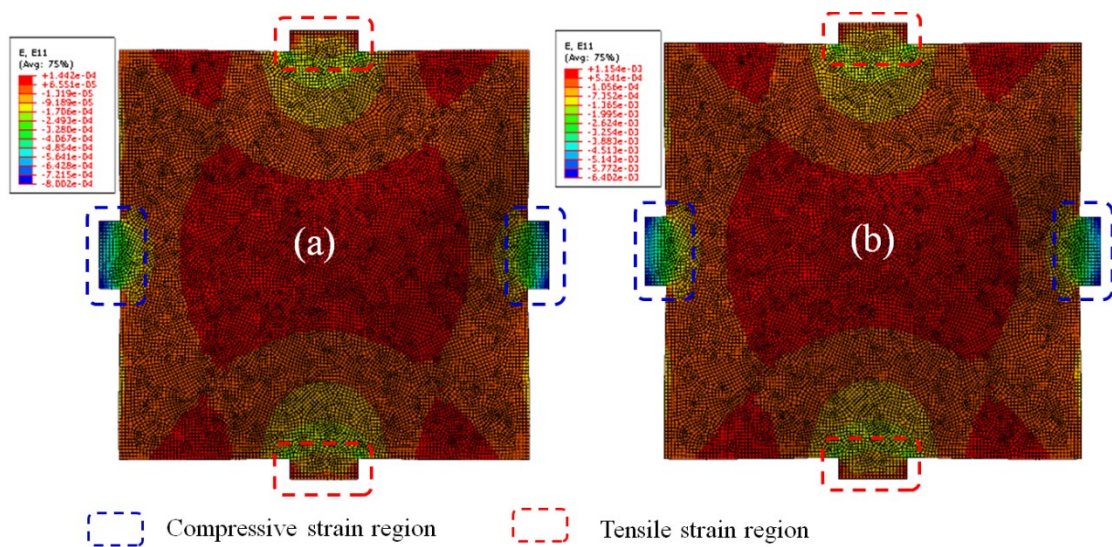
Figure 6. 3 FEM result of strain distribution on diaphragm under pressure of (a) 25 mmHg and (b) 200 mmHg.

According to the FEM result (shown in Figure 6.3), the average strain changes for 1μm SiNWs and bulk silicon wire at 25 mmHg are 8×10^{-4} and 3.3×10^{-4} respectively. With a reasonable assumption of gauge factors ($G = 90$ for SiNWs and $G = 50$ for bulk silicon wires), $\mathit{\Delta}$R/R % is around 7.2% and 1.7% for SiNWs and bulk silicon wires. Based on the same logic, the expected $\mathit{\Delta}$R/R % is around 57% and 13% for SiNWs and bulk silicon wires, respectively. It is thus verified the functionality of different piezoresistor designs for various applications.

The current designs have validated both proper trench and optimum releasing-hole design with a minimum thickness of passivation. Further research efforts will be focusing on the realization of the actual device with aforementioned advantages.

6.2.2 Silicon Probe for Lateral Brain Micro-motion with Minimum Invasion
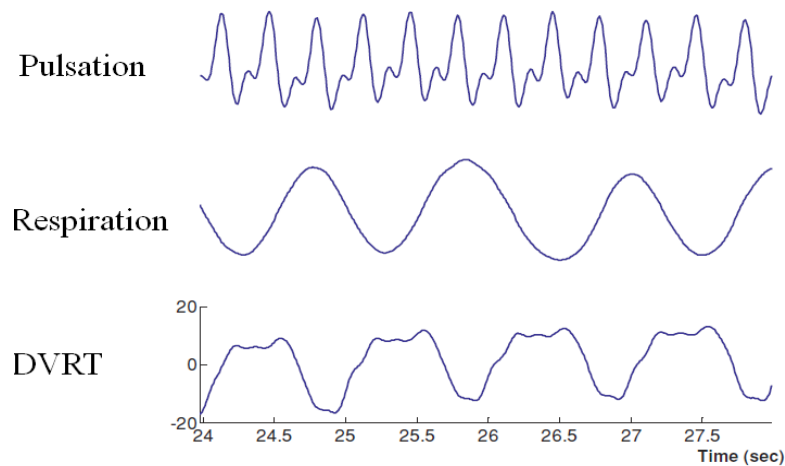
Figure 6. 4 A typical trace of simultaneous pulses. DVRT gives the superimposed micro-motion due to both pulsation and respiration [193].

Understanding the brain micro-motion helps the researcher to study the initial tissue damage and examine the contributing factor to chronic inflammatory response. Our current design of silicon probe is able detect the implantation bulking and respiration induced brain micro-motion (refer to chapter 5), but the resolution can still

be enhanced. In most experimental study, the micro-motion is detected by using a commercialized differential variable reluctance transducer (DVRT) through a vertical direction [193]. A typical output from DVRT is shown in Figure 6.4.

Generally, brain micro-motion may arise from physiological, behavioral or other mechanical sources. Physiological sources are most common causes and include both cardiac rhythm and fluctuation in respiratory pressure. It is theoretical feasible to utilize the implantable device for the detection of lateral micro-motion instead of in vertical way. The previous design (refer to chapter 5) may be too rigid to sense the smaller lateral forces, since the SiNWs are embedded inside the silicon substrate (refer to Figure 5.1 for the device drawing). In order to increase the device sensitivity for a lateral movement, a flexible diaphragm structure is proposed along the probe shank. Its schematic is provided in Figure 6.5.
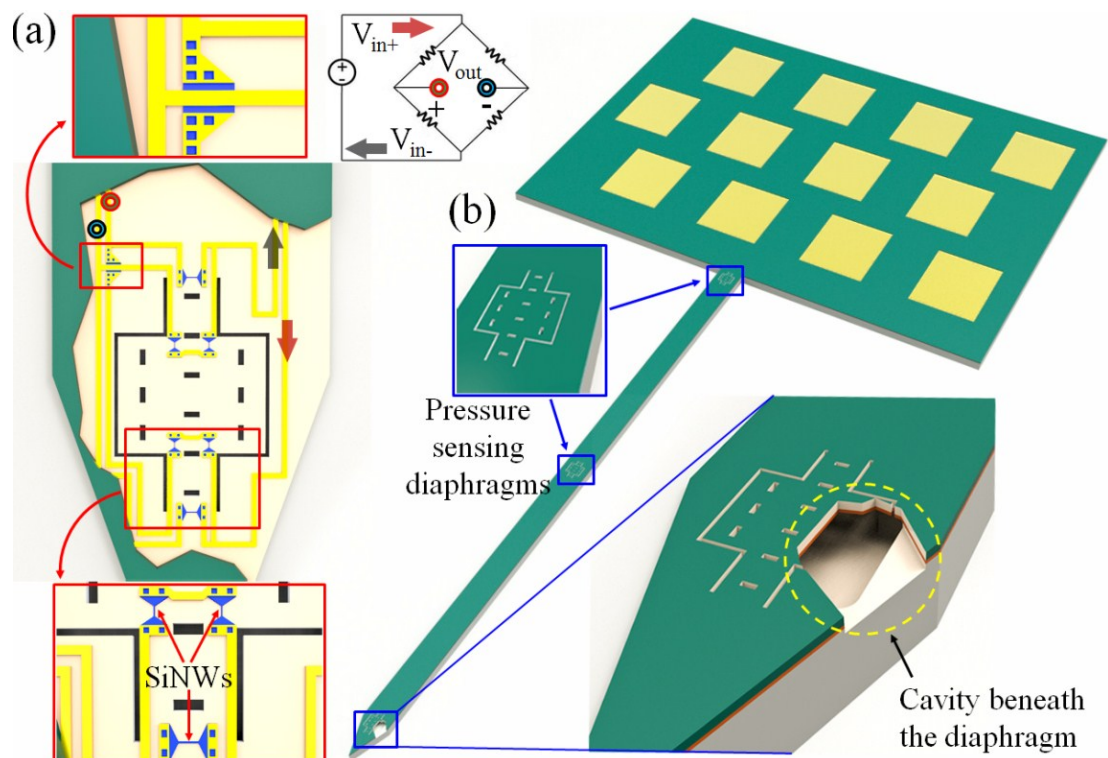
Figure 6. 5 (a) Schematic of electrical connections (full Wheatstone bridge) and the location of SiNWs for a maximized sensitivity, (b) the device drawing of the proposed silicon probe for lateral micro-motion sensing. Inset shows the structure of suspended diaphragm and the cavity below the diaphragm.

Figure 6.5 (b) shows three suspended diaphragms along the probe (tip, middle and base of the shank). The device fabrication can be realized through a similar isotropic etching process mentioned in previous section (chapter 6.2.1).
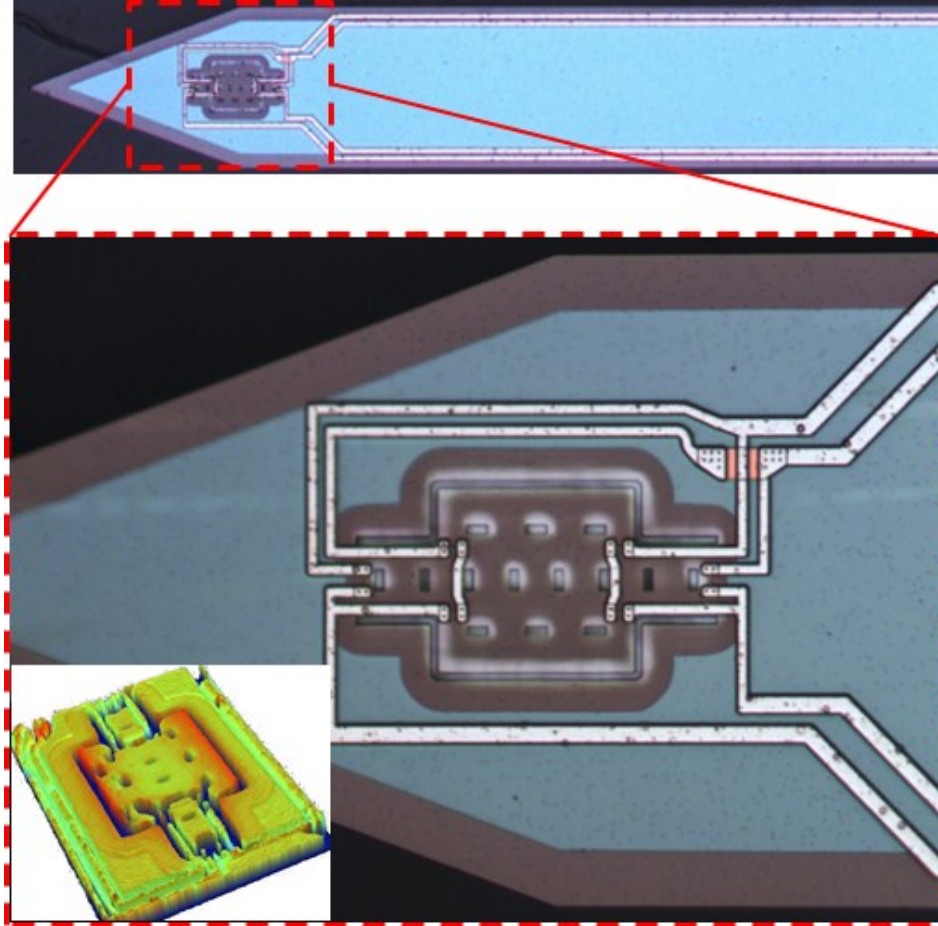
Figure 6. 6 Optical images of a released diaphragm structure on the probe tip. The 3D surface profile is provided in the inset indicating an initial diaphragm deflection less than 0.2μm.

As the prototype design, the trench has not been included in the device. The diaphragm over-releasing is thus observed in Figure 6.6. To validate the device capability, further experiments needs to be carried in future.

In addition to a less sensitive lateral micro-motion response, the optimization for the thickness of probe shank needs to be further explored for the purposes of less initial tissue damage as well as a reduced chronic response. After proper boron diffusion into the silicon substrate, the silicon probe with tip thickness of 15μm has

been demonstrated [117]. The even thinner probe shank (~ 10μm) can be realized by utilizing polymer material (e.g. polyimide) [183], which theoretically favor a less foreigner body response due to much lower young's modulus. However, the problem of a proper packaging remains as a challenge topic. Recently, Jeon *et al*. propose a hybrid neural probe [194], which composes both rigid silicon (tip and base of the probe) and flexible polyimide (middle of the probe) structures as demonstrated in Figure. 6.7.
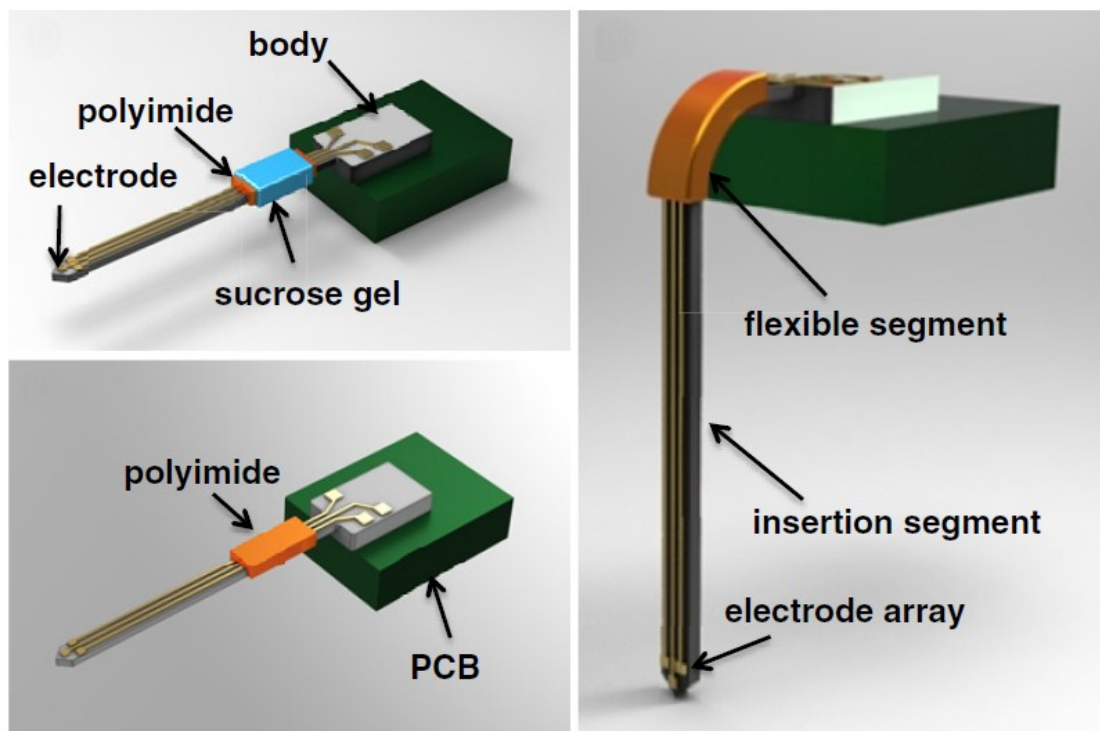
Figure 6. 7 Schematic of the partially flexible MEMS neural probe [194].

By leveraging the flexibility of the polyimide, the reported probe will introduce less initial tissue damage during the implantation. Nevertheless, the problem of inflammatory chronic response between tissue and foreigner body still remains. For the future development of the neural probe, it is necessary to dedicate the research effort on the realization of silicon based flexible probe with an ultra-thin shank for a minimum invasion and the negligible chronic reaction.

Bibliography

[1] J. Bryzek, ''MEMS: A closer look at part 2: The MEMS industry in Silicon Valley and its impact on sensor technology,'' Sensors, Jul. 4, 1996.

[2] J. W. Knutti, ''Finding markets for microstructures,'' in Micromachining and Microfabrication Process Technology IV, Santa Clara, CA, pp. 17–23. 1998

[3] N. Yazdi, F. Ayazi, and K. Najafi, ''Micromachined inertial sensors,'' *Proc. IEEE*, vol. 86, pp. 1640–1659, 1998.

[4] H. Chen, M. Bao, H. Zhu, and S. Shen, ''A piezoresistive accelerometer with a novel vertical beam structure,'' *Sensors and Actuators A: Physical*, vol. 63, pp. 19–25, 1997.

[5] O. N. Tufte, P. W. Chapman, and D. Long, ''Silicon diffused-element piezoresistive diaphragms,'' *J. Appl. Phys.*, vol. 33, pp. 3322–3327, 1962.

[6] L. Lin, and W. Yun, "Design, optimization and fabrication of surface micromachined pressure sensors," *Mechatronics*, vol.8, no.5, pp.505-519, 1998

[7] B. W. Chui, T. W. Kenny, H. J. Mamin, B. D. Terris, and D. Rugar, ''Independent detection of vertical and lateral forces with a sidewall-implanted dual-axis piezoresistive cantilever", *Appl. Phys. Lett.*, vol. 72, pp.1388, 1998.

[8] J. Brugger, M. Despont, C. Rossel, H. Rothuizen, P. Vettiger, and M. Willemin, ''Microfabricated ultrasensitive piezoresistive cantilevers for torque magnetometry,'' *Sens. Actuators, B*, vol. 73 (3), pp. 235-242, 1999.

[9] A J van der Wie, M A Boillat and N F de Rooij 1995 A Bi-directional Silicon Orifice Flow Sensor Characterised For Fluid Temperature And Pressure *8th Int. Conf. on Solid-State Sensors and Actuators and Eurosensors IX* vol 2 pp 420-423

[10] J. Chen, Z. F. Fan, J. Zou, J. Engel and C. Liu, "Two-dimensional micromachined flow sensor array for fluid mechanics studies", *J Aerospace Eng,* vol. 16**,** pp.85-97, 2003.

[11] R. He and P. Yang, "Giant piezoresistance effect in silicon nanowires", *Nature Nanotechnology*, vol. 1, pp 42 – 46, 2006.

[12] P. Neuzil, C. C. Wong and J. Reboud, "Electrically controlled giant piezoresistance in silicon nanowires", *Nano Letters*., Vol.10, pp.1248-1252, 2010.

[13] J. S. Milne, A. C. H. Rowe, S. Arscott and Ch. Renner, "Giant Piezoresistance Effects in Silicon Nanowires and Microwires," *Phys. Rev. Lett.*, vol.105, pp.206802, 2010.

[14] L.K.Tymon Barwicz, Steven J. Koester, and Hendrik Hamann, "Silicon nanowire piezoresistance: Impact of surface crystallographic orientation," *Appl. Phys. Lett.*, vol.97, no.2, pp.023110, 2010

[15] T. Toriyama, Y. Tanimoto, and S. Sugiyama, "Single crystal silicon nano-wire piezoresistors for mechanical sensor," *Journal of Microelectromechanical Systems*, vol.11, no.5, pp. 605-611, 2002.

[16] T. Toriyama, D. Funai, and S. Sugiyama,''Piezoresistance measurement on single crystal silicon nanowires,'' *Journal of Applied Physics*, vol. 93, pp. 561–565, 2003.

[17] D. V. Dao, T. Toriyama, and S. Sugiyama, ''Noise and frequency analyses of aminiaturized 3-DOF accelerometer utilizing silicon nanowire piezoresistors,'' Proceeding of IEEE Sensors International Conference, vol. 3, pp. 1464–1467, 2004.

[18] M.-W. Shao, Y.-Y. Shan, N.-B. Wong，and S.-T. Lee, ''Silicon Nanowire sensors for bioanalytical applications: Glucose and hydrogen peroxide detection,'' *Advanced Functional Materials*, vol. 15, pp. 1478–1482,

[19] G. Yoshikawa, *et al.*, "Nanomechanical Membrane-type Surface Stress Sensor," *Nano Lett.*, vol.11, no.(3), pp. 1044-1048. 2011

[20] D. Stephen , *Microsystem Design*, New York, NY: Springer, 2004

[21] W. Thomson, "On the electro-dynamic qualities of metals: Effects of magnetization on the electric conductivity of nickel and of iron,'' *Proc. R. Soc. London*, vol. 8, pp. 546–550, 1856.

[22] H. Tomlinson, "On the increase in resistance to the passage of an electric current produced on wires by stretching,'' *Proc. R. Soc. London*, vol. 25, pp. 451–453, 1876.

[23] H. Tomlinson, "The influence of stress and strain on the action of physical forces,'' *Philos. Trans. R. Soc. London*, vol. 174,pp. 1–172, 1883

[24] J. Bardeen and W. Shockley, ''Deformation potentials and mobilities in non-polar crystals,'' *Phys. Rev.*, vol. 80, pp. 72–80, 1950.

[25] C. S. Smith, "Piezoresistance effect in germanium and silicon," *Phys. Rev.*, vol.94, pp. 42–49, 1954.

[26] W. P. Mason and R. N. Thurston, "Use of piezoresistive materials in the measurement of displacement, force, and torque,'' *J. Acous. Soc. of Am.*, vol. 29, pp. 1096–1101, 1957.

[27] W. G. Pfann and R. N. Thurston,"Semiconducting stress transducers utilizingthe transverse and shear piezoresistance effects,'' *J. Appl. Phys.*, vol. 32, pp. 2008–2019, 1961.

[28] Y. Kanda, "Piezoresistance effect in silicon," *Sensors and Actuators A: Physical*, vol.28, pp. 83-91, 1991.

[29] G. E. Kimball, "The electronic structure of diamond", *J. Chem. Phys.*, vol. 3, pp. 560-C564, 1935.

[30] J. F. Mullaney, "Optical properties and electronic structure of solid silicon", *Phys.Rev.*, vol. 66, pp. 326-C339, 1944

[31] C. Herring, "Transport properties of a many valley semiconductor", *Bell Syst. Tech. J.*, vol. 34, pp. 237¨C290, Mar. 1955.

[32] C. Herring, "Transport and deformation potential theory for many-valley semiconductors with anisotropic scattering", *Phys. Rev.*, vol. 101, p. 944, 1956.

[33] A. A. Barlian, W. -T. Park, J. R. Mallon, A. J. Jr. Rastegar and B. L. Pruitt B, "Review: Semiconductor Piezoresistance for Microsystems," *Proc. IEEE*, vol. 97, pp.513-552, 2009.

[34] Y. Kanda, "A graphical representation of the piezoresistance coefficients in silicon," *IEEE Transactions on Electron Devices*, vol.29, no.1, pp. 64-70, 1982.

[35] T. Toriyama, S. Sugiyama, "Analysis of piezoresistance in p-type silicon for mechanical sensors," *Journal of Microelectromechanical Systems*. vol.11, no.5, pp. 598-604, 2002

[36] S. I. Kozlovskiy, *et al.*, "First-order piezoresistance coefficients in silicon crystals," *Sensors and Actuators A: Physical*, vol.118, pp. 33-43, 2005.

[37] S. I. Kozlovskiy, *et al.*, "First-order piezoresistance coefficients in heavily doped p-type silicon crystals," *Sensors and Actuators A: Physical*, vol.133, pp. 72-81, 2007.

[38] J. Richter, *et al.*, "Pieozresistance in p-type silicon revisited," *Journal of applied physics*, vol. 104, 023715, 2008.

[39] F. J. Morin, *et al.*, "Temperaure dependance of the piezoresistance of high-purity silicon and germanium," *Phys. Rev.*, vol. 105, pp. 525-539, 1957

[40] O. N. Tufte and E. L. Stelzer, "Piezoresistive properties of silicon diffused layers," *Journal of appliced physics*, vol. 34, no. 2, pp. 313-318, 1963

[41] J. A. Harley and T. W. Kenny, ''1/f noise considerations for the design and process optimization of piezoresistive cantilevers", *Journal of Microelectromechanical Systems*, vol. 9, pp. 226–235, 2000.

[42] M.-W. Shao, Y.-Y. Shan, N.-B. Wong, and S.-T. Lee, "Silicon Nanowire sensors for bioanalytical applications: Glucose and hydrogen peroxide detection", *Advanced Functional Materials*, vol. 15, pp. 1478-1482, 2005.

[43] K. Reck, J. Richter, O. Hansen, and E. V. Thomsen "Piezoresistive effect in top-down fabricated silicon nanowires", *Proc. IEEE MEMS*, pp. 717-720, 2008.

[44] Rowe, C. H. Alistair, "Silicon nanowires feel the pinch", *Nature nanotechnology*, vol.3, pp.311-312, 2008.

[45] B. Kloeck and N. F. De Rooij, "Mechanical sensors," in *Semiconductor Sensors*, S. M. Sze, Ed. New York: Wiley, ch. 4., 1994.

[46] M. Shikida, K. YoshiKawa, S. Iwai and K. Sato 2012 Flexible flow sensor for large-scale air-conditioning network systems *Sensors and Actuators A: Physical.* DOI: 10.1016/j.sna.2011.12.002.

[47] C. Li, P-M Wu, J. A. Hartings, Zh Wu, Ch. H. Ahn, D. LeDoux, L. A. Shutter, and R. K. Narayan, "Smart catheter flow sensor for real-time continuous regional cerebral blood flow monitoring", *Appl. Phys. Lett,.* vol. 99, 233705, 2011.

[48] M. Shikida, T. Yokota, T. Kawabe, T. Funaki, M. Matsushima, S. Iwai, N. Matsunaga and K. Sato "Characteristics of an optimized catheter-type thermal flow sensor for measuring reciprocating airflows in bronchial pathways", *J. Micromech. Microeng.,* vol. 20, 125030, 2010.

[49] S Billat, K Kliche, R Gronmaier, P Nommensen, J Auber, F Hedrich and R Zengerle, "Monolithic integration of micro-channel on disposable flow sensors for medical applications", *Sensors and Actuators A: Physical*, vol. 145–146, pp. 66-74, 2008.

[50] A. F. P. Van Putten and S. Middelhoek, "Integrated silicon anemometer", *Electronics Letters*, vol. 10, pp.425-6. 1974.

[51] S. Haasl and G. Stemme, *Comprehensive Microsystems,* ed Z Hans (Oxford: Elsevier) pp 209-72. 2008.

[52] R. Buchner, K. Froehner, C. Sosna, W. Benecke and W. Lang, "Toward Flexible Thermoelectric Flow Sensors: A New Technological Approach", *J. Microelectromech. Syst.*, vol.17, 1114-9, 2008.

[53] B. W. van Oudheusden and A. W. van Herwaarden, "High-sensivity 2-D flow sensor with an etched thermal isolation structure", *Sensors and Actuators A: Physical*, vol. 22, pp. 425-30, 1989.

[54] T. Neda, K. Nakamura and T. Takumi, "A polysilicon flow sensor for gas flow meters", *Sensors and Actuators A: Physical*, vol. 54, pp. 626-31, 1996.

[55] N. T. Nguyen, "Micromachined flow sensors - a review", *Flow Meas. Instrum.*, vol. 8 pp.7-16, 1997.

[56] R. Buchner, C. Sosna, M. Maiwald, W. Benecke and W. Lang, "A high-temperature thermopile fabrication process for thermal flow sensors", *Sensors and Actuators A: Physical*, vol.130–131, pp. 262-266, 2006.

[57] C. Sosna, T. Walter, W. Lang, "Response time of thermal sensor with air as fluid", *Sensors and Actuators A: Physical*, vol. 172, pp.15-20. 2011.

[58] O. Tabata, "Fast-response silicon flow sensor with an on-chip fluid temperature

sensing element", *IEEE Trans. Electron. Devices.*, vol.33, pp.361-5, 1986.

[59] Y. C. Tai and R. S. Muller, "Lightly-doped polysilicon bridge as a flow meter", *Sensors and Actuators A: Physical*, vol. 15, pp. 63-75, 1988.

[60] L. Lofdahl, G. Stemme, and B. Johansson, "A sensor based on silicon technoligy for turbulence measurements", *J. Phys. E: Sci. Instrum,* vol. 22, pp.391-393, 1989.

[61] G. N. Stemme, "A monolithic gas flow sensor with polyimide as thermal insulator", *IEEE Trans. Electron. Devices.*, vol. 33, pp. 1470, 1986.

[62] C. Liu, J. B. Huang, Z. J. Zhu, F. K. Jiang, S. Tung, Y. C. Tai, and C. M. Ho, "A Micromachined flow shear-stress sensor based on thermal transfer principles", *J. Microelectromech. Syst.*, vol. 8, pp. 90-99, 1999.

[63] Y. Xu, Q. Lin, G. Y. Lin, R. B. Katragadda, F. K. Jiang, S. Tung and Y. C. Tai, "Micromachined thermal shear-stress sensor for underwater applications", *J. Microelectromech. Syst.*, vol. 14, pp. 1023-30, 2005.

[64] Y. Xu, C. W. Chiu, F. K. Jiang, Q. Lin, and Y. C. Tai, "A MEMS multi-sensor chip for gas flow sensing", *Sensors and Actuators A: Physical*, vol. 121, pp. 253-61, 2005.

[65] S. Kim, T. Nam and S. Park, "Measurement of flow direction and velocity using a micromachined flow sensor", *Sensors and Actuators A: Physical*, vol. 114, pp. 312-8, 2004.

[66] W. C. Shin and R. S. Besser, "A micromachined thin-film gas flow sensor for microchemical reactors", *J. Micromech. Microeng.*, vol. 16, pp. 731-41, 2006.

[67] Z. Y. Tan, M. Shikida, M. Hirota, K. Sato, T. Iwasaki and Y. Iriye, "Experimental and theoretical study of an on-wall in-tube flexible thermal sensor", *J. Micromech. Microeng.*, vol. 17, pp. 679-86, 2007.

[68] R Ahrens and K Schlote-Holubek, "A micro flow sensor from a polymer for gases and liquids", *J. Micromech. Microeng.*, vol. 19 pp. 074006, 2009.

[69] K. Kliche, S. Billat, F. Hedrich, C. Ziegler and R. Zengerle, "Sensor for gas analysis based on thermal conductivity, specific heat capacity and thermal diffusivity", *Proc. 24th Int. Conf. on Micro Electro Mechanical Systems (MEMS)*, pp.1189-92, 2011.

[70] Y. H. Wang, C. P. Chen, C. M. Chang, C. P. Lin, C. H. Lin, L. M. Fu and C. Y. Lee, "MEMS-based gas flow sensors", *Microfluid. Nanofluid.*, vol. 6, pp. 333-46, 2009.

[71] N. Svedin, E. Kälvesten and G. Stemme, "A lift force sensor with integrated hot-chips for wide range flow measurements", *Sensors and Actuators A: Physical*, vol. 109, pp. 120-30, 2003.

[72] N. Svedin, E. Kälvesten, E. Stemme and G. Stemme, "A new silicon gas-flow sensor based on lift force", *J. Microelectromech. Syst.*, vol. 7, pp. 303-8, 1998.

[73] J. Shajii, K. Y. Ng and M. A. Schmidt, "A microfabricated floating-element shear stress sensor using wafer-bonding technology", *J. Microelectromech. Syst.*, vol. 1, pp. 89-94, 1992.

[74] A. A. Barlian, S-J Park, V Mukundan and B. L. Pruitt, "Design and characterization of microfabricated piezoresistive floating element-based shear stress sensors", *Sensors and Actuators A: Physical*, vol. 134, pp. 77-87, 2007.

[75] Y. Ozaki, T. Ohyama, T. Yasuda and I. Shimoyama, "An air flow sensor modeled on wind receptor hairs of insects", *Proc. 13th Int. Conf. on Micro Electro Mechanical Systems (MEMS),* pp. 531-536, 2000.

[76] A J van der Wie, M A Boillat and N F de Rooij, "A Bi-directional Silicon Orifice Flow Sensor Characterised For Fluid Temperature And Pressure", *8th Int. Conf.*

on Solid-State Sensors and Actuators and Eurosensors IX, vol. 2, pp. 420-423, 1995.

[77] J. Chen, Z. F. Fan, J. Zou, J. Engel and C. Liu, "Two-dimensional micromachined flow sensor array for fluid mechanics studies", *J Aerospace Eng.*, vol. 16, pp. 85-97, 2003.

[78] J. Liu, J. Wang and X. Li, "Fully front-side bulk-micromachined single-chip micro flow sensors for bare-chip SMT (surface mounting technology) packing", *J. Micromech. Microeng.*, vol. 22, pp. 035020, 2012.

[79] C. Lee, T. Itoh and T. Suga, "Micromachined Piezoelectric Force Sensors Based on PZT Thin Films", *IEEE Trans. Ultrasonics, Ferroelectrics and Frequency Control*, vol. 43, pp. 553-559, 1996.

[80] S. zhang, L. Lou and C. Lee, "Piezoresistive nanowire based nanoelectromechanical system cantilever air flow sensor", *Appl. Phys. Lett.*, vol. 100, pp. 023110, 2012.

[81] C. Lee, J. Thillaigovindan, C-C Chen, X. T. Chen, Y-T Chao, S. H. Tao, W. F. Xiang, A. Yu, H. H. Feng and G. Q. Lo, "Si nanophotonics based cantilever sensor", *Appl. Phys. Lett.*, vol. 93., pp. 113113, 2008.

[82] Y H Seo and B H kim, "A self-resonant micor flow velocity sensor based on a resonant frequency shift by flow-induced vibration", *J. Micromech. Microeng.*, vol. 20, pp. 075024, 2010.

[83] Y-T Lee, C-W Lin, C-M Lin, S-R Yeh, Y-C Chang and W. Fang, "A Pseudo-3D Glass Microprobe Array: Glass Microprobe with Embedded Silicon for Alignment and Electrical Interconnection during Assembly", *J. Micromech. Microeng.*, vol. 20, pp. 201-209, 2010.

[84] Y. Li, Q. Zheng, Y. Hu and Y. Xu, "Micromachined Piezoresistive Accelerometers Based on an Asymmetrically Gapped Cantilever", *J. Microelectromech. Syst.*, vol. 20, pp. 83-94, 2011.

[85] H. Liu, C. J. Tay, C. Quan, T. kobayashi and C. Lee, "Piezoelectric MEMS engery harvester for low-frequency vibrations with wideband operation range and steadily increased output power", *J. Microelectromech. Syst.*, vol. 20, pp. 1131-1142, 2011.

[86] Y Su, A G R Evans, A Brunnschweiler and G Ensell, "Characterization of a highly sensitive ultra-thin piezoresistive silicon cantilever probe and its application in gas flow velocity sensing", *J. Micromech. Microeng.*, vol. 12, pp. 780-785, 2002.

[87] Z F Fan, J Chen, J Zou, D Bullen, C. Liu and F Delcomyn, "Design and fabrication of artificial lateral line flow sensors", *J Micromech. Microeng.*, vol. 12, pp. 655-661, 2002.

[88] N N, Chen C Tucker, J M Engel, Y C Yang, S Pandya and C. Liu, "Design and characterization of artificial haircell sensor for flow sensing with ultrahigh velocity and angular sensitivity", *J. Microelectromech. Syst.*, vol. 16, pp. 999-1014, 2007.

[89] Y. H. Wang, C. Y. Lee and C. M. Chiang, "A MEMS-based air flow sensor with a free-standing micro-cantilever structure", *Sensors*, vol. 7, pp. 2389-401, 2007.

[90] C. Y. Lee, C. Y. Wen, H. H. Hou, R. J. Yang, C. H. Tsai and L. M. Fu, "Design and characterization of MEMS-based flow-rate and flow-direction microsensor", *Microfluid. Nanofluid.*, vol. 6, pp. 363-71, 2009.

[91] A. R. Aiyar, C. Song, S-H Kim and M. G. Allen, "An all-polymer airflow sensor using a piezoresistive composite elastomer", *Smart Mater. Struct.*, vol. 18, pp. 115002. 2009.

[92] C. Song, A. R. Aiyar, S-H. kim and M. G. Allen, "Exploitation of aeroelastic effects for drift reduction, in an all-polymer air flow sensor", *Sensors and Actuators A: Physical*, vol. 165, pp. 66, 2011.

[93] D. Li, T. Zhao, Z. C. Yang and D. C. Zhang, "Monolithic integration of a micromachined piezoresistive flow sensor", *J. Micromech. Microeng.*, vol. 20, 2010.

[94] M. Esashi, S. Sugiyama, K. Ikeda, Y. Wang, and H. Miyashita, "Vacuum-sealed silicon micromachined pressure sensors", *Proc. IEEE*, vol. 86, pp. 1627–1639, 1998.

[95] J. Bryzek, S. Roundy, B. Bircumshaw, C. Chung, K. Castellino, J. R. Stetter , M. Vestel, "Marvelous MEMS", *IEEE Circuits Devices Mag.*, vol. 22, pp. 8–28, 2006.

[96] F. P. Burns, "Piezoresistive semiconductor microphone", *U.S. Patent 2 905 771*, Sep. 22, 1959.

[97] E. R. Peake, A. R. Zias, and J. V. Egan, "Solid-state digital pressure transducer", *IEEE Tran. Electron Devices*, vol. 16, pp. 870–876, 1969.

[98] S. Samaun, K. Wise, E. Nielsen, and J. Angell, "*An IC piezoresistive pressure sensor for biomedical instrumentation*", *IEEE International Solid-State Circuits Conference*, pp. 104–105, 1971.

[99] J. F. Marshall, "Fabrication of semiconductor devices utilizing ion implantation", *U.S. Patent 4 033 787*, Jul. 5, 1977.

[100]   Kim, K.H., B.H. Kim, and Y.H. Seo, "A noncontact intraocular pressure measurement device using a micro reflected air pressure sensor for the prediagnosis of glaucoma", *Journal of Micromechanics and Microengineering,* vol. 22, no.3, pp. 035022, 2012.

[101]   P. Melvas, and G. Stemme, "A diode-based two-wire solution for temperature-compensated piezoresistive pressure sensors", *IEEE Transactions on Electron Devices*, vol.50, no.2, pp. 503-509, 2003

[102]   S. Marco *et al.*, "High-performance piezoresistive pressure sensors for biomedical applications using very thin structured membranes", *Measurement Science and Technology,* vol.7, no.9, pp. 1195, 1996.

[103]   M. Shimazoe, *et al.*, "A special silicon diaphragm pressure sensor with high output and high accuracy", *Sensors and Actuators A: Physical*, vol.2, no.0, pp. 275-282, 1982.

[104]   H. Sandmaier, "Non-linear analytical modelling of bossed diaphragms for pressure sensors", *Sensors and Actuators A: Physical*, vol.27, no.1–3, pp. 815-819, 1991.

[105]   M. Bao, L. Yu, and Y. Wang, "Stress concentration structure with front beam for pressure sensor", *Sensors and Actuators A: Physical*, vol.28, no.2, pp. 105-112, 1991.

[106]   M, Bao., L. Yu, and Y. wang, "Micromachined beam-diaphragm structure improves performances of pressure transducer", *Sensors and Actuators A: Physical*, vol.21, no.1–3, pp. 137-141, 1990.

[107]   R.H. Johnson, *et al.*, "A high-sensitivity ribbed and bossed pressure transducer", *Sensors and Actuators A: Physical*, vol.35, no.2, pp. 93-99, 1992.

[108]   L, Lin., C. Huey-Chi, and Y.-W. Lu, "A simulation program for the sensitivity and linearity of piezoresistive pressure sensors," Journal of Microelectromechanical Systems, vol.8, no.4, pp. 514-522, 1999.

[109]   K. Matsuda, *et al.*, "Nonolinearity of piezoresistance effect in p- and n- type silicon", *Sensors and Actuators A: Physical*, vol. A21-A23, pp.45-48, 1990.

[110]   S. Marco, *et al.*, "Analysis of nonlinearity in high sensitivity piezoresistive pressure sensors", *Sensors and Actuators A: Physical*, vol.37–38, no.0, pp.790-795, 1993.

[111]   Woinowsky-krieger, *Theory of Plates and Shells*. 2nd ed., New York: McGraw-Hill, 1970.

[112]   D. A. Robinson, "The electrical properties of metal microelectrodes", *Proc. IEEE*, vol. 56, pp. 1065-1082. 1968.

[113]   W. H. Dobelle, M. G. Mladejovsky, and J. P. Girvin, "Artifical vision for the blind: electrical stimulation of visual ortex offers hope for a functional prosthesis", *Science*, vol. 183, pp. 440-444, 1974.

[114]   S. Musallam, M. J. Bak, P. R. Troyk, R. A. Andersen, "A floating metal microelectrode array for chronic implantation", *J. Neurosci. Meth.*, vol. *160*, pp.122-127, 2007.

[115]   E. M. Schmidt, M. J. Bak, P. Christensen, "Laser exposure of Parylene-C insulated microelectrodes", *J. Neurosci. Meth.*, vol. 62, pp. 89-92, 1995.

[116]   K. E. Petersen, "Silicon as a mechanical material", *Proc. IEEE*, vol. 70 (5), pp. 420-457, 1982.

[117]   Wise K. D., Sodagar A. M., Yao Y., Gulari M. N., Perlin G. E., Najafi K., "Microelectrodes, Microelectronics, and Implantable Neural Microsystems", *Proc. IEEE*, vol. 96 (7), 1184-1201, 2008.

[118]   R. A. Normann, E. M. Maynard, P. J. Rousche, D. J. Warren, "A neural interface for a cortical vision prosthesis", *Vision Res.*, vol. 39, pp. 2577-2587, 1999.

[119]   L. Lin, A. P. Pisano, "Silicon Processed Microneedles", *IEEE J. Microelectromech. Syst.*, vol. 8 (1), pp. 78-84, 1999.

[120]   D. Papageorgiou, S. Shore, S. Bledsoe, and K. D. Wise, "A shuttered probe with in-line flowmeters for chronic in-vivo drug delivery", *IEEE J. Microelectromech. Syst.*, vol. 15, pp. 1025–1033, 2006.

[121]   K. Seidl, S. Spieth, S. Herwik, J. Steigert, R. Zengerle, O. Paul, P. Ruther, "In-plane silicon probes for simultaneous neural recording and drug delivery", *J. Micromech. Microeng.*, vol. 20, 105006, 2010

[122]   O. Frey, T. Holtzman, R. M. McNamara, D. E. H. Theobald, P. D. van der Wal, N. F. de Rooij, J. W. Dalley, M. Koudelka-Hep, "Enzyme-based choline and L-glutamate biosensor electrodes on silicon microprobe arrays", *Biosens. Bioelectron.*, vol. 26, pp. 477-484. 2010.

[123]   O. Frey, P. D. van der Wal, S. Spieth, O. Brett, K. Seidl, O. Paul, P. Ruther, R. Zengerle, N. F. de Rooij, "Biosensor microprobes with integrated microfluidic channels for bi-directional neurochemical interaction", *J. Neural Eng.*, vol. 8, 066001, 2011.

[124]   W. Wei, Y. Song, W. Shi, N. Lin, T. Jiang, X. Cai, "A high sensitivity MEA probe for measuring real time rat brain glucose flux", *Biosens. Bioelectron.*, vol. 55, pp. 66-71, 2014.

[125]   T. H. Yoon, E. J. Hwang, D. Y. Shin, S. I. Park, S. J. Oh, S. C. Jung, H. C. Shin, S. J. Kim, "A micromachined silicon depth probe for multichannel neural recording", *IEEE Trans. Biomed. Eng.*, vol. 47, pp. 1082-1087, 2000.

[126]   K. C. Cheung, K. Djupsund, Y. Dan, and L. P. Lee, "Implantable multichannel electrode array based on SOI technology", *IEEE J. Microelectromech. Syst.*, vol. 12, pp. 179–184, 2003.

[127]   R. Biran, D. C. Martin, and P. A. Tresco, "Neuronal cell loss accompanies the brain tissue response to chronically implanted silicon microelectrode arrays",

Exp. Neurology, vol. 195 (1), pp. 115-126, 2005.

[128]   V. S. Polikov, P. A. Tresco, W. M. Reichert, "Response of brain tissue to chronically implanted neural electrodes", *J. Neurosci. Meth.*, vol. 148, pp. 1-18, 2005.

[129]   J. P. Seymour, D. R. Kipke, Neural probe design for reduced tissue encapsulation in CNS", *Biometerials*, vol. 28, pp. 3594-3607, 2007.

[130]   C. Kim and K. D.Wise, "A 64-site multi-shank CMOS low-profile neural stimulating probe", *IEEE J. Solid-State Circuits*, vol. 31, pp. 1230–1238, 1996.

[131]   K. Seidl, S. Herwik, T. Torfs, H. P. Neves, O. Paul, P. Ruther, "CMOS-Based High-Density Silicon Microprobe Arrays for Electronic Depth Control in Intracortical Neural Recording", *IEEE J. Microelectromech. Syst.,* vol. 20 (6), pp. 1439-1448, 2011.

[132]   Y-T. Lee, S-R. Yeh, Y-C. Chang, W. Fang, "Integration of silicon-via electrodes with different recording characteristics on a glass microprobe using a glass reflowing process", *Biosens. Bioelectron.*, vol. 26, pp. 4739-4746, 2011.

[133]   M. Tykocinski, Y. Duan, B. Tabor, R. S. Cowan, "Chronic electrical stimulation of the auditory nerve using high surface area (HiQ) platinum electrode", *Hear Res.*, vol. 159 (1-2), pp. 53-68, 2001.

[134]   S. F. Cogan, J. Ehrlich, T. D. Plante, A. Smirnov, D. B. Shire, M. Gingerich, J. F. Rizzo, "Sputtered iridium oxide films for neural stimulation electrodes", *J. Biomed. Mater. Res. B Appl. Biomater.*, vol. 89(2), pp. 353-361., 2009.

[135]   Y. Lu, D. Wang, T. Li, X. Zhao, Y. Cao, H. Yang, Y. Y. Duan, "Poly(vinyl alcohol)/poly(acrylic acid) hydrogel coatings for improving electrode–neural tissue interface", *Biomaterials*, vol. 30, pp. 4143-4151, 2009.

[136]   S. Chen, W. Pei, Q. Gui, R. Tang, Y. Chen, S. Zhao, H. Wang and H. Chen, "PEDOT/MWCNT composite film coated microelectrode arrays for neural interface improvement", *Sensor Actuat a-Phys.*, vol. 193, pp. 141, 2013.

[137]   H. Zhang, J. Shih, J. Zhu, and N. A. Kotov, "Layered Nanocomposites from Gold Nanoparticles for Neural Prosthetic Devices", *Nano Lett.*, vol. 12, pp. 339, 2012.

[138]   J-K. Wu, Y-S. Wu, C-S. Yang, F-G. Tseng, "Charge-selective gate of arrayed MWCNTs for ultra high-efficient biomolecule enrichment by nano-electrostaticsieving (NES)", *Biosens. Bioelectron.*, vol. 43, pp. 453-460, 2013.

[139]   C-H. Chen, C-T. Lin, W-L. Hsu, Y-C. Chang, S-R. Yeh, L-J. Li, D-J. Yao, "A flexible hydrophilic-modified graphene microprobe for neural and cardiac recording", *Nanomedicine: Nanotechnology, Biology, and Medicine*, vol. 9, pp. 600-604, 2013.

[140]   S.F. Cogan, "Neural Stimulation and Recording Electrodes", *Annu. Rev. Biomed. Eng.,* vol. 10, pp. 275-209, 2008.

[141]   K. Najafi, K. D. Wise, and T. Mochizuki, "A high-yield IC-compatible multichannel recording array", *IEEE Trans. Electron Devices*, vol. ED-32, pp. 1206–1211, 1985.

[142]   Y-K. Song, W. R. Patterson, C. W. Bull, J. Beals, N. Hwang, A. P. Deangelis, C. Lay, J. L. McKay, A. K. Nurmikko, R. Matthew, J. D. Simeral, J. P. Donoghue, B. W. Conners, "Development of a chipscale integrated microelectrode /microelectronic device for brain implantable neuroengineering applications", *IEEE Trans. Neural Syst. Rehabi. Eng.*, vol. 13(2), pp. 220-226, 2005.

[143]   G. Charvet, L. Rousseau, O. Billoint, S. Gharbi, J-P. Rostaing, S. Joucla, M. Trevisiol, A. Bourgerette, P. Chauvet, C. Moulin, *et al.*, "BioMEA^{TM}: A versatile

high-density 3D microelectrode array system using integrated electronics", *Biosens. Bioelectron.*, vol. 25, pp. 1889-1896. 2010.

[144]   C-W. Lin, Y-T. Lee, C-W. Chang, W-L. Hsu, Y-C. Chang, W. Fang, "Novel glass microprobe arrays for neural recording", *Biosens. Bioelectron.*, vol. 25, pp. 475-481, 2009.

[145]   S. Spieth, O. Brett, K. Seidl, A. A. A. Aarts, M. A. Erismis, S. Herwik, F. Trenkle, S. Tatzner, J. Auber, M. Daub, *et al.*, "A floating 3D silicon microprobe array for neural drug delivery compatible with electrical recording", *J. Micromech. Microeng.*, vol. 21, 125001, 2011.

[146]   K. Kwon, B. Sirowatka, A. Weber, W. Li, "Opto- µECoG array: a hybrid neural interface with transparent µECoG electrode array and integrated LEDs for optogenetics", *IEEE Trans. Biomed. Circuits Syst.,* vol. 7(5), pp. 593-600, 2013.

[147]   Chen C-H., Chuang S-C., Su H-C., Hsu W-L., Yew T-R., Chang Y-C., Yeh S-R., Yao D-J., "A three-dimensional flexible microprobe array for neural recording assembled through electrostatic actuation", *Lab Chip*, vol. 11, pp. 1647-1655, 2011.

[148]   K. Seidl, M. Schwaerzle, I. Ulbert, H. P. Neves, O. Paul, P. Ruther, "CMOS-Based High-Density Silicon Microprobe Arrays for Electronic Depth Control in Intracortical Neural Recording–Characterization and Application", *IEEE J. Microelectromech. Syst.*, vol. 21(6), pp. 1426-1435, 2012.

[149]   A. Sridharan, D. R. Subramaniam, J. Muthuswamy, "Long-term changes in the material properties of brain tissue at the implant–tissue interface", *J. Neural Eng.*, vol. 10, 066001, 2013.

[150]   C. S. Bjornsson, S. J. Oh, Y. A. Al-Kofahi, Y. J. Lim, K. L. Smith, J. N. Turner, S. De, B. Roysam, W. Shain, S. J. Kim, "Effects of insertion conditions on tissue strain and vascular damage during neuroprosthetic device insertion", *J. Neural Eng.*, vol. 3, pp. 196-207, 2006.

[151]   A. A. Sharp, A. M. Ortega, D. Restrepo, D. Curran-Everett, K. Gall, "In Vivo Penetration Mechanics and Mechanical Properties of Mouse Brain Tissue at Micrometer Scales", *IEEE Trans. Biomed. Eng.*, vol. 56(1), pp. 45-53, 2009.

[152]   M. Welkenhuysen, A. Andrei, L. Ameye, W. Eberle, B. Nuttin, "Effect of insertion speed on tissue response and insertion mechanics of a chronically implanted silicon-based neural probe", *IEEE Trans. Biomed. Eng.*, vol. 58(11), pp. 3250-3258, 2011.

[153]   A. Andrei, M. Welkenhuysen, B. Nuttin, W. Eberle, "A response surface model predicting the in vivo insertion behavior of micromachined neural implants", *J. Neural Eng.*, vol. 10, 016005, 2012.

[154]   L. D. Landau, E. M. Lifshitz, Theory of Elasticity, Course of Theoretical Physics, Vol. 5, Pergamon, Oxford, 1959.

[155]   C-L. Hsin, W. Mai, Y. Gu, Y. Gao, C-T. Huang, Y. Liu, L-J. Chen, Z-L. Wang, "Elastic Properties and Buckling of Silicon Nanowires", *Adv. Mater.*, vol. 20, pp. 3919-3923, 2008.

[156]   K. Najafi, J. F. Hetke, "Strength Characterization of Silicon Microprobes in Neurophysiological Tissues", *IEEE Trans. Biomed. Eng.*, vol. 37(5), pp. 474-481, 1990.

[157]   J. H. Kim, K. T. Park, H. C. Kim, K. Chun, "Fabrication Of A Piezoresistive Pressure Sensor For Enhancing Sensitivity Using Silicon Nanowire", *SoEE , University of Ulsan , Ulsan , KOREA*, pp.1936-1939, 2009

[158]   B. Soon, P. Neuzil, C. Wong, J. Reboud, H. Feng and C. Lee, "Ultrasensitive nanowire pressure sensor makes its debut", *Procedia Eng.*, vol.5, pp. 1127-1130,

2010.

[159]   B. Han, Y-J. Yoon, M. Hamidullah, A. T-H. Lin, and W-T. Park, "Silicon nanowire-based ring-shaped tri-axial force sensor for smart integration on guidewire", *J. Micromech. Microeng.*, vol. 24, 065002, 2014.

[160]   H. C. Card, "Aluminum-Silicon Schottky Barriers and Ohmic Contacts in Integrated Circuits", *IEEE Transactions on Electron Devices*, vol. ED-23, no.6, pp. 538-544, 1976.

[161]   H. M. Naguib and L. H. Hobbs, "Al/Si and Al/Poly-Si Contact Resistance In Integrated Circuits", *J. Electrochem. Soc.*, vol. 124, no. 4, pp. 573-577, 1977.

[162]   S. M. Sze and Kwok K. Ng , *Physics of semiconductor devices*, 3rd edn. Hoboken, NJ : Wiley-Interscience, 2007.

[163]   A. Tarraf, J. Daleiden, S. Irmer, D. Prasai and H. Hillmer, "Stress investigation of PECVD dielectirc layers for advanced optical MEMS", *J. Micromech. Microeng.* vol.14, 317–323, 2004.

[164]   Liang Lou, Songsong Zhang, Woo-Tae Park, Julius Ming-Lin Tsai, Dim-Lee Kwong and Chengkuo Lee, "Optimization of NEMS pressure sensors with multilayered diaphragm using silicon nanowires as piezoresistive sensing elements", *J. Micromech. Microeng.*, vol. 22, no. 5, 055012, 2012.

[165]   Y Su, A G R Evans, A Brunnschweiler and G Ensell, "Characterization of a highly sensitive ultra-thin piezoresistive silicon cantilever probe and its application in gas flow velocity sensing", *J. Micromech. Microeng.*, vol.12, pp. 780-785, 2002.

[166]   J. Yang, J. Gaspar and O. Paul, "Fracture Properties of LPCVD Silicon Nitride and Thermally Grown Silicon Oxide Thin Films From the Load-Deflection of Long Si3N4 and SiO2/Si3N4 Diaphragms", *J. Microelectromech. Syst.*, vol.17,   pp.1120-1134., 2008.

[167]   R. H. Ma, C. Y. Lee, Y. H. Wang and H. J. Chen, "Microcantilever-based weather station for temperature, humidity and flow rate measurement", *Microsyst. Technol.*, vol. 14, pp. 971, 2008.

[168]   P. Singh, J M Miao, W-T Park and D-L Kwong "Gate-bias-controlled sensitivity and SNR enhancement in a nanowire FET pressure sensor", *J Micromech. Microeng.*, vol. 21, 105007, 2011.

[169]   Tao Wang, Liang Lou, and Chengkuo Lee, "A junctionless gate-all-around silicon nanowire FET of high linearity and its potential applications", *IEEE Electron Device Lett.*, vol. 34, no. 4, pp. 478-480, 2013.

[170]   F M White 1999 *Fluid Mechanics* 4th edn (New York: McGraw-Hill).

[171]   R. K. Bansal, *A Textbook of Strength of Materials* Revised 4th edn (LAXMI PUBLICATIONS (P) LTD), 2010.

[172]   J. Wei, S. Magnani and P. Sarro "Suspended submicro silicon-beam for high sensitivity piezoresistive force sensing cantilevers", *Sensors and Actuators A: Physical*, vol. 186., pp. 80-85, 2012.

[173]   K. Yamada, M. Nishihara, S. Shimada, M, Tanabe, M. Shimazoe and Y. Matsuoka, "Nonlinearity of the piezoresistance effect of p-type silicon diffused layers," *IEEE Transactions on Electron Devices*, vol.29, no.1, pp. 71-77, 1982.

[174]   A. Yasukawa, M. Shimazoe, and Y. Matsuoka, "Simulation of circular silicon pressure sensors with a center boss for very low pressure measurement," *IEEE Trans Electron Devices*, vol.36, no.7, pp. 1295-1302, 1989.

[175]   J. Albert Chiou, and S. Chen, "Pressure nonlinearity of micromachined piezoresistive pressure sensors with thin diaphragms under high residual stresses," *Sensors and Actuators A: Physical*, vol.147, no.1, pp. 332-339, 2008.

[176] M. Shimazoe, *et al.*, "A special silicon diaphragm pressure sensor with high output and high accuracy," *Sensors and Actuators A: Physical*, vol.2, no.0, pp. 275-282, 1982.

[177] Stephen Beeby, Graham Ensell, Michael Kraft, Neil White, *MEMS – Electromechanical Sensors*. 2nd ed., Boston: Artech House, Inc., 2004.

[178] J. Mallon, F. Pourahmadi, K. Petersen, P. Barth, T. Vermeulen and J. Brezek, "Low-pressure sensors employing bossed diaphragms and precision etch-stopping," *Sensors and Actuators A: Physical*, vol.21-23, pp.89-95, 1990.

[179] G. E. Pikus, G. L. Bir, "Effect of deformation on the hole energy spectrum of germanium and silicon," *Sov. Phys. –Solid State*, vol. 1, pp. 1502-1517, 1960.

[180] Zhizhen Wu, Chunyan Li, Jed A. Hartings, Raj K. Narayan and Chong H. Ahn, "A New Intracranial Pressure Sensor on Polyimide Lab-on-a-Tube using Exchanged Polysilicon Piezoresistors", *17th International Conference on Solid-State Sensors, Actuators and Microsystems (Transducers 2013)*, Barcelona, Spain, pp.1779-1782, June 16-20, 2013.

[181] B. Bae, K. Bark, M. A. Shannon, "Low-pressure treatment control of glaucoma using an electromagnetic valve actuator with a piezoresistive pressure sensor," *3rd IEEE/EMBS special topic conference on Microtechnology in Medicine and Biology*, pp. 126-129, May 2005.

[182] E. W. Keefer, B. R. Botterman, M. I. Romero, A. F. Rossi, and G. W. Gross, "Carbon nanotube coating improves neuronal recordings", *Nat. Nanotechnol.*, vol. 3, pp. 434, 2008.

[183] Zhuolin Xiang, Shih-Cheng Yen, Ning Xue, Tao Sun, Wei Mong Tsang, Songsong Zhang, Lun-De Liao, Nitish Thakor, and Chengkuo Lee, "Ultra-thin Flexible Polyimide Neural Probe Embedded in Dissolvable Maltose-Coated Microneedle", *J. Micromech. Microeng,* vol. 24, no. 6, pp. 065015, 2014.

[184] B. E. Conway, "Transition from "supercapacitor" to "battery" behavior in electrochemical energy storage", *J. Electrochem. Soc.*, vol. 138, pp.1539-1548, 1991.

[185] K. Wang, H. A. Fishman, H. Dai and James, and S. Harris, "Neural Stimulation with a Carbon Nanotube Microelectrode Array", *Nano Lett.*, vol. 6 (9), pp. 2043, 2006.

[186] A. O. Fung , C. Tsiokos, O. Paydar, L. H. Chen, S. Jin, Y. Wang, and J. W. Judy, "Electrochemical Properties and Myocyte Interaction of Carbon Nanotube Microelectrodes", *Nano Lett.*, vol. 10, pp. 4321, 2010.

[187] G. Cellot, E. Cilla, S. Cipollone, V. Rancic, A. Sucapane, S. Giordan, L. Gambazzi, H. Markram, M. Grandolfo, D. Scaini *et. al.*, "Carbon nanotubes migh improve neuronal performance by favouring electrical shortcuts", *Nature Nanotechnology*, vol. 4, pp. 126, 2009.

[188] H. H. Zhou, X. Cheng, L. Rao, T. Li, Y. Y. Duan, "Poly (3, 4-ethylenedioxythiophene)/multiwall carbon nanotube composite coatings for improving the stability of microelectrodes in neural prostheses applications" *Acta Biomaterialia*, vol. 9, pp. 6439, 2013.

[189] W. M. Tsang, A. L. Stone, D. otten, Z. N. Aldworth, T. L. Daniel, J. G. Hildebrand, R. B. Levine, and J. Voldman, "Insect-machine interface: A carbon nanotube-enhanced flexible neural probe", *J. Neurosci. Methods*, vol. 204, pp. 355, 2012.

[190] W. Lu, L. Qu, K. Henry, and L. Dai, "High performance electrochemical capacitors from aligned carbon nanotube electrodes and ionic liquid electrolytes", *Journal of Power Sources*, vol. 189 (2), pp. 1270, 2009.

[191]   X. F. Wei and W. M. Grill, "Impedance characteristics of deep brain stimulation electrodes in vitro and in vivo", *J. Neural Eng.*, vol. 6, 046008, 2009.

[192]   Liang Lou, Woo-Tae Park, Songsong Zhang, Lishiah Lim, Dim-Lee Kwong and Chengkuo Lee, "Characterization of silicon nanowire embedded in a MEMS diaphragm structure within large compressive strain range", *IEEE Electron Device Lett.*, vol. 32, no. 12, pp. 1764-1766, 2011.

[193]   A. Gilletti, J. Muthuswamy, "Brain micromotion around implants in the rodent somatosensory cortex", *J. Neural. Eng.*, vol. 3, pp. 189-195, 2006.

[194]   M. Jeon, J. Cho, Y. K. Kim, D. Jung, E-S. Yoon, S. Shin, and II-J. Choo, "Partially flexible MEMS neural probe composed of polyimide and sucrose gel for reducing brain damage during and after implantation", *J. Micromech. Microeng,* vol. 24, 025010, 2014.

Appendix: List of Publication

Journal Paper

1. **Songsong Zhang**, Wei Mong Tsang, Zhuolin Xiang, Shih-Cheng Yen, Nitish Thakor, Dim-Lee Kwong and Chengkuo Lee, "Piezoresistive silicon nanowires embedded CMOS-compatible silicon electrode probe for neural signal recording and implantation mechanics monitoring", *Nanoscale*. (Under review).

2. **Songsong Zhang**, Tao Wang, Liang Lou, Wei Mong Tsang, Renshi Sawada, Dim-Lee Kwong and Chengkuo Lee, "Annularly Grooved Diaphragm Pressure Sensor with Embedded Silicon Nanowires for Low Pressure Application", *IEEE/ASME J. Microelectromech. Syst.*, (To be published).

3. Zhuolin Xiang, Shih-Cheng Yen, Ning Xue, Tao Sun, Wei Mong Tsang, **Songsong Zhang**, Lun-De Liao, Nitish Thakor, and Chengkuo Lee, "Ultra-thin Flexible Polyimide Neural Probe Embedded in Dissolvable Maltose-Coated Microneedle", *J. Micromech. Microeng*, vol. 24, no. 6, pp. 065015, 2014.

4. **Songsong Zhang**, Wei Mong Tsang, Merugu Srinivas, Tao Sun, Navab Singh, Dim-Lee Kwong, and Chengkuo Lee, "Development of silicon electrode enhanced by carbon nanotube and gold nanoparticle composites on silicon neural probe fabricated with complementary metal-oxide-semiconductor process", *Appl. Phys. Lett.*, vol. 104, no. 19, pp.193105, 2014.

5. Huicong Liu, **Songsong Zhang**, Takeshi Kobayashi, Tao Chen and Chengkuo Lee, "Flow sensing and energy harvesting characteristics of a wind-driven piezoelectric Pb(Zr0.52, Ti0.48)O3 microcantilever", *Micro & Nano Lett.*, vol. 9, no.4, pp. 286-289, 2014.

6. **Songsong Zhang**, Liang Lou, Woo-Tae Park and Chengkuo Lee, "Characterization of silicon nanowire based cantilever air flow sensor", *J. Micromech. Microeng.*, vol. 22, no. 9, 095008, 2012.

7. Huicong Liu, **Songsong Zhang**, Ramprakash Kathiresan, Takeshi Kobayashi, and Chengkuo Lee, "Development of piezoelectric microcantilever flow sensor with wind-driven energy harvesting capability", *Appl. Phys. Lett.*, vol. 100, no. 22, 223905, 2012.

8. Liang Lou, **Songsong Zhang**, Woo-Tae Park, Julius Ming-Lin Tsai, Dim-Lee Kwong and Chengkuo Lee. "Optimization of NEMS pressure sensors with multilayered diaphragm using silicon nanowires as piezoresistive sensing elements", *J. Micromech. Microeng.*, vol. 22, no. 5, 055012, 2012.

9. **Songsong Zhang**, Liang Lou and Chengkuo Lee, "Piezoresistive silicon nanowire based nanoelectromechanical system cantilever air flow sensor", *Appl. Phys. Lett*, vol. 100, no. 2, 02311, 2012.

10. Liang Lou, Woo-Tae Park, **Songsong Zhang**, Lishiah Lim, Dim-Lee Kwong and Chengkuo Lee, "Characterization of silicon nanowire embedded in a MEMS diaphragm structure within large compressive strain range", *IEEE Electron Device Lett.*, vol. 18 no .4, p. 497-506, 2012.

Conference Paper

1. **Songsong Zhang,** Wei Mong Tsang, Srinivas Merugu, Tao Sun, Dim-Lee Kwong, and Chengkuo Lee, "Silicon neural probe fabricated by CMOS-compatible process with highly P-doped silicon electrode for establishing neuron-electrode interface", *The 6th International Symposium on Microchemistry and Microsystems (ISMM 2014)*, Singapore, 30 July ~ 1 August, 2014.

2. **Songsong Zhang**, Tao Wang, Chengkuo Lee, Liang Lou, Wei-Mong Tsang, Dim-Lee Kwong, "Silicon Nanowires Embedded Pressure Sensor with Annularly Grooved Diaphragm for Sensitivity Improvement", *IEEE 9th Intern.Conf. on Intelligent Sensors, Sensor Networks and Information Processing (IEEE ISSNIP 2014)*, Singapore, 21-24, April, 2014.

3. **Songsong Zhang**, Liang Lou, Tao Wang, Wei Mong Tsang, Dim-Lee Kwong and Chengkuo Lee, "Characterization of Silicon Nanowire (SiNWs) embedded NEMS Sensor for Potential Biomedical Applications", *IMWS-Bio 2013*, Singapore, Dec. 9-11, 2013.

4. **Songsong Zhang**, Liang Lou, Woo-Tae Park, Li Shiah Lim, Wei Mong Tsang, Minkyu Je and Chengkuo Lee, "Silicon nanowires (SiNWs) based NEMS piezoresistive mechanical sensors for potential bio-medical applications", *Intern. Conf. on BioElectronics, BioSensor, BioMedical Devices, BioMEMS/NEMS and Applications 2012 (Bio4Apps 2012)*, PP-11, CeLS, National University of Singapore, Singapore, Nov. 19-20, 2012.

5. **Songsong Zhang**, Liang Lou, and Chengkuo Lee, "Air Flow Sensor Using Microcantilever Embedded with Piezoresistive Silicon Nanowires", *IEEE Sensors 2012*, Taipei, Taiwan, Oct. 28-31, 2012.

6. **Songsong Zhang**, Liang Lou, Huicong Liu, and Chengkuo Lee, "Piezoresistive air flow meter with silicon nanowire as sensing element", *Intern. Union of Mat. Research Soc. - Intern. Conf. on Electronic Mat. (IUMRS-ICEM 2012)*, Symposium B-7 (MEMS/NEMS and MicroTAS), B-7O24-003, Yokohama, Japan, Sep. 23-28, 2012.

7. Liang Lou, **Songsong Zhang**, Lim Lishiah, Woo-Tae Park, Hanhua Feng, Dim-Lee Kwong, Chengkuo Lee, "Characteristics of NEMS piezoresistive silicon nanowires pressure sensors with various Diaphragm Layer", *Eurosensors XXV, Procedia Engineering*, vol. 25, p. 1433-1436, 2011.